NTIA Report 00-379

A Frequency- and Time-Domain Investigation into the Geometric Optics Approximation for Wireless Indoor Applications

Michael G. Cotton
Edward F. Kuester
Christopher L. Holloway

U.S. DEPARTMENT OF COMMERCE
William M. Daley, Secretary

Gregory L. Rohde, Assistant Secretary
for Communications and Information

June 2000

This Page Intentionally Left Blank

This Page Intentionally Left Blank

CONTENTS

Page

A FREQUENCY- AND TIME-DOMAIN INVESTIGATION INTO THE GEOMETRIC OPTICS APPROXIMATION FOR WIRELESS INDOOR APPLICATIONS

Michael G. Cotton,* Edward F. Kuester,** and Christopher L. Holloway***

In this study we investigated the geometric optics (GO) approximation to the fields of an incremental electric dipole above a half plane for geometries typical of wireless indoor communications. This inspection was motivated by efforts to establish a ray-trace model to characterize indoor radio propagation channels. Eight canonical geometries were examined to isolate near-surface and near-field effects that are not accounted for in the GO approximation. Common building materials and physical dimensions (i.e., antenna separation and height) as small as 1 cm were investigated for frequencies up to 8 GHz. Theoretical fields were calculated via numerical evaluation of Sommerfeld integrals and compared to corresponding GO approximations. As expected, GO approximations agreed with theoretical results when the source and observation points were multiple wavelengths above the surface and relatively far apart. Close to the surface, an interesting interference pattern in the frequency domain was caused by adjacent fields in the two media propagating at different speeds. This so-called "pseudo-lateral wave" phenomenon is discussed and demonstrated in various examples. Next, we emulated system specifications (i.e., center frequency and bandwidth), computed time-domain impulse responses, and used delay spread as a metric to quantify GO error. Results show that mechanisms exist under certain circumstances which invalidate GO assumptions; conventional expressions to complement GO approximations are summarized.

Key words: geometric optics; indoor propagation channel; propagation over ground; Sommerfeld integral; numerical integration; ray-trace model; impulse response; delay spread

1. INTRODUCTION

With the growing emergence of indoor wireless local area networks (WLAN), characterization of the indoor propagation channel has become more important. This environment can be characterized in either the frequency or time domain. Frequency-domain modeling takes the form of field-strength

*The author is with the Institute for Telecommunication Sciences, National Telecommunications and Information Administration, U.S. Department of Commerce, Boulder, CO 80303.

**The author is with the Department of Electrical and Computer Engineering, University of Colorado, Boulder, CO 80309.

***The author is with the National Institute of Standards and Technology, U.S. Department of Commerce, Boulder, CO 80303.

predictions over a volume of interest for specified frequencies. In contrast, time-domain modeling is based on the impulse response of the particular environment. For digital communications, the impulse response is a quantity used to characterize the multipath propagation environment. Propagation effects on a transmitted signal are best described by a linear-system representation

$$b(t) = \int_{-\infty}^{+\infty} a(t-\tau)\, g(t,\tau)\, \mathrm{d}\tau \quad , \tag{1}$$

where $a(t)$ and $b(t)$ are the symbol waveforms before and after propagation through the channel, $g(t,\tau)$ is the time-variable impulse response of the propagation channel, and τ is the delay variable.

Multipath propagation environments, such as the indoor-propagation channel, exhibit characteristic impulse responses. For line-of-sight indoor channels, an impulse response is composed of a direct ray plus numerous rays due to reflections off objects, diffraction around objects, and transmission through objects. Impulse response data is useful for the analysis and simulation of digital transmission because it quantifies communication-link degradation within a channel. More specifically, the delay spread τ_{spr} of a channel impulse response is a measure of time-dispersion due to multipath [1, 2] and is defined as

$$\tau_{spr} = \sqrt{\frac{\int_{-\infty}^{+\infty} (\tau - \bar{\tau})^2 |g(t,\tau)|^2 \, \mathrm{d}\tau}{\int_{-\infty}^{+\infty} |g(t,\tau)|^2 \, \mathrm{d}\tau}} \quad , \tag{2}$$

where $\bar{\tau}$ is the first moment or mean delay given by

$$\bar{\tau} = \frac{\int_{-\infty}^{+\infty} \tau |g(t,\tau)|^2 \, \mathrm{d}\tau}{\int_{-\infty}^{+\infty} |g(t,\tau)|^2 \, \mathrm{d}\tau} \quad . \tag{3}$$

As a rule of thumb, small τ_{spr} indicates little degradation, whereas if τ_{spr} is large then severe distortion occurs. Therefore, the data rate may need to be decreased in a high-delay-spread multipath environment in order to maintain or reduce the bit-error rate.

A threshold associated with the calculation of delay spread exists to nullify the noise contribution (i.e., values of $|g(t,\tau)|^2$ below the threshold are set to zero). Throughout this report, a threshold of -30 dB relative to the peak of the impulse is used for all delay spread calculations. Delay spread

quantifies inter-symbol interference and has been the subject of numerous publications such as [1-10]. In most cases, statistical analyses were necessary to account for stochastic processes within the time-variant channel. In this report we are not interested in the time-variant nature of the channel, denoted by the dependent variable t in $g(t,\tau)$, nor statistical procedures to account for stochastic processes. Hence, we assume that the channel is deterministic and that a single impulse response is completely representative.

Various approaches are used to determine impulse-response delay spread for indoor applications, such as ray-trace models [11-24], statistical models based on measurements [25-33], simplified-decay models [34, 35], and full numerical techniques [36-39] (e.g., finite-difference time-domain). The most popular of these techniques is ray-tracing, which is based on GO and assumes that near-surface and near-field effects are negligible and that Fresnel reflection coefficients are valid. For indoor applications, however, transmit and/or receive antennas are likely to be mounted close to a wall or ceiling. Therefore, the GO approximation is in question since the antennas are only a few centimeters from reflecting surfaces. GO errors, relative to the numerical approximation of the general Sommerfeld formulation, are presented here in frequency-domain field-strength predictions and time-domain impulse-response results.

Our goal is to investigate the shortcomings of the GO approximation for antennas mounted close to reflecting surfaces. We focus on a classic problem – dipole radiation above a lossy half space – and consider the elementary vertical electric dipole (VED) and x-aligned elementary horizontal electric dipole (HED) as sources. If there exists a set of substantive single-reflection cases which produce significant near-surface and near-field errors under practical frequency and geometric constraints, then we conclude that GO is an inadequate approximation.

This report is organized in the following manner. In Section 2, we summarize Sommerfeld's classical integral formulation and provide geometric optics expressions for elementary dipoles above an infinite ground plane. Numerical techniques to evaluate Sommerfeld integrals are given in Section 3. Frequency-domain field strength results are given in Section 4. The frequency-domain results are transformed to a complex-baseband representation of a passband signal in order to calculate the channel impulse response. A detailed explanation of the time-domain analyses is given in Section 5, and corresponding results are shown in Section 6.

2. EXPRESSIONS FOR RADIATION IN FREE SPACE OVER GROUND

In order to isolate errors associated with the GO approximation for typical indoor scenarios, we focus on a single reflection off a planar surface. The classic problem of elementary dipole radiation above a ground plane has been analyzed extensively [40-46]. The geometry and nomenclature are shown in Figures 1 and 2. Region 0 is free space; the source dipole and receiver, regardless of nature and orientation, are located in region 0 at heights h and z above the interface, respectively. Region 1 lies beneath the interface; its material composition is defined by its relative dielectric constant ε_r and conductivity σ. All media are assumed to be isotropic, homogeneous, and non-magnetic.

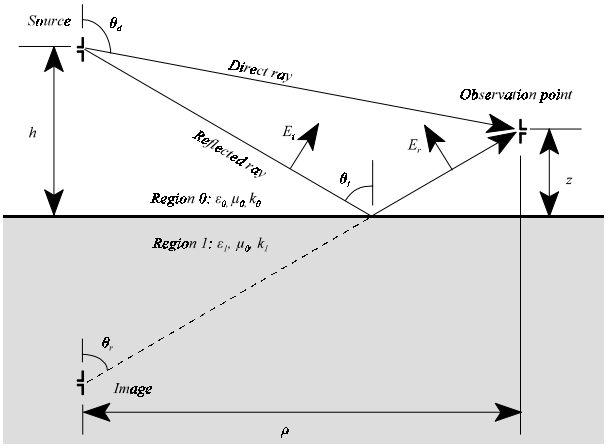

Figure 1. Parallel polarization geometry for *E*-fields above dielectric half-space.

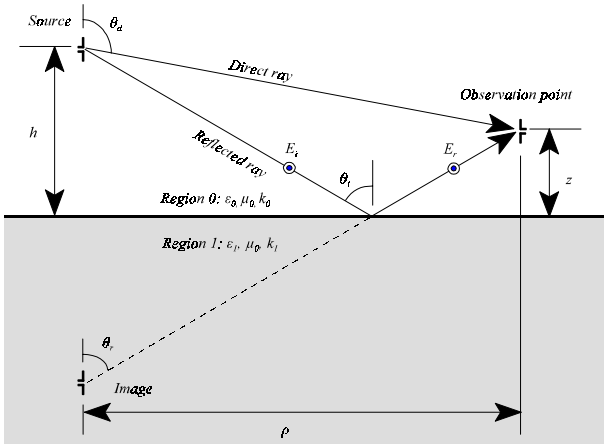

Figure 2. Perpendicular polarization geometry for *E*-fields above dielectric half-space.

The general formulation of the two-media boundary problem is based on the solution of Maxwell's equations subject to boundary conditions at the interface. The differential form of Maxwell's equations, assuming exp(+$j\omega t$) harmonic time dependence for the fields, is

$$\nabla \times \vec{E} = -j\omega\mu_0 \vec{H} \quad \text{and} \quad \nabla \times \vec{H} = \vec{J} + j\omega\varepsilon \vec{E} \quad , \tag{4}$$

where $\vec{E}$ is an electric field, $\vec{H}$ is a magnetic field, $\vec{J}$ is an impressed current source, capital letters denote time-harmonic fields (in contrast to time-instantaneous field variables, which are in lower case), and $\vec{}$ denotes a vector. The electric-type Hertz vector $\vec{\Pi}$ is useful for solving electromagnetic fields generated by a time-harmonic electric current; fields are expressed in terms of $\vec{\Pi}$ as

$$\vec{E} = k^2 \vec{\Pi} + \nabla(\nabla \cdot \vec{\Pi}) \quad \text{and} \quad \vec{H} = j\omega\varepsilon \nabla \times \vec{\Pi} \quad . \tag{5}$$

An alternative form to Maxwell's equations is the Helmholtz equation, given by

$$(\nabla^2 + k^2)\vec{\Pi} = -\frac{\vec{J}}{j\omega\varepsilon} \quad , \tag{6}$$

where $k_1^2 = \omega^2\mu_0(\varepsilon_r\varepsilon_0 - j\sigma/\omega)$ defines the wave number of medium 1. Boundary conditions enforce continuity of tangential $\vec{E}$ and $\vec{H}$ components at the interface and allow for a unique solution of $\vec{\Pi}$.

2.1. Sommerfeld Formulation

The classic Sommerfeld formulation for a dipole above a half plane is a general solution that contains complex, highly oscillatory integrals. Sommerfeld integrals provide an exact solution, but have yet to be solved analytically. Numerical schemes for evaluating these integrals are covered in Section 3. The formulations for VED and HED are given in the following subsections.

2.1.1. Vertical Electric Dipole (VED)

An incremental vertical current element placed a height *h* above the half plane in the z direction produces a z-directed component of the vector potential in regions 0 and 1. For a VED, $\Pi_z(\rho, z)$ is independent of φ and only the E_z, E_ρ, and H_φ field components are radiated. The Helmholtz equations in both media must be satisfied and boundary conditions apply at the interface. The solution to the partial differential equation is simplified via the double Fourier transform. Additionally, the specified geometry suggests a transformation to cylindrical coordinates that introduces a Bessel function into the integral solution. The resulting Sommerfeld formulation for the vector potential in region 0 is taken from [41] and is given by

$$\Pi_z = \frac{j\omega\mu_0 p}{4\pi k_0^2} [\, G_0 - G_1 + k_1^2 V \,] \quad , \tag{7}$$

where *p* is the dipole moment. The source and image Green's functions are defined as

$$\begin{aligned} G_0 &= \frac{\exp(-jk_0R_0)}{R_0} = \int_0^\infty \frac{\exp[-l|h-z|]}{l} J_0(\xi\rho)\,\xi\,\mathrm{d}\xi \quad \text{and} \\ G_1 &= \frac{\exp(-jk_0R_1)}{R_1} = \int_0^\infty \frac{\exp[-l(h+z)]}{l} J_0(\xi\rho)\,\xi\,\mathrm{d}\xi \quad , \end{aligned} \tag{8}$$

respectively, where $J_0(\xi\rho)$ is the Bessel function of the first kind and order zero. The distances from the observation point to the source and image are

$$R_0 = \sqrt{\rho^2 + (z-h)^2} \quad \text{and} \quad R_1 = \sqrt{\rho^2 + (z+h)^2} \quad , \tag{9}$$

respectively. The Sommerfeld integral *V* is defined as

$$V = \int_0^\infty \frac{2\exp[-l(z+h)]}{lk_1^2 + mk_0^2} J_0(\xi\rho)\,\xi\,\mathrm{d}\xi \quad , \tag{10}$$

and the functions *l* and *m* are given by

$$l = \sqrt{\xi^2 - k_0^2} \quad \text{and} \quad m = \sqrt{\xi^2 - k_1^2} \quad . \tag{11}$$

Equation (7) is concise but not optimal for numerical evaluation given the electric properties of the reflecting surfaces considered in this report. An alternative form was used by van der Pol [45] and

is given by

$$\Pi_z = \frac{j\omega\mu_0 p}{4\pi k_0^2}\,[G_0 + G_1 - 2Q] \quad , \tag{12}$$

where

$$Q = \int_0^\infty \frac{m k_0^2 \exp[-l(z+h)]}{l(l k_1^2 + m k_0^2)}\, J_0(\xi\rho)\,\xi\,\mathrm{d}\xi \quad . \tag{13}$$

Under this convention, the sum $G_0 + G_1$ represents the situation when the ground is perfectly conducting and the Sommerfeld integral Q represents a correction for the lossy characteristics of ground. For the material properties considered, the formulation of equation (12) significantly reduces the magnitude of the integrand in equation (13) and consequently improves the convergence and accuracy of the numerical integration.

Relevant field components are extracted from equation (5) to form the following field expressions:

$$\begin{aligned} E_z &= \frac{j\omega\mu_0 p}{4\pi k_0^2}\left[\left(\frac{\partial^2}{\partial z^2} + k_0^2\right)(G_0 + G_1 - 2Q)\right] \\ E_\rho &= \frac{j\omega\mu_0 p}{4\pi k_0^2}\left[\frac{\partial^2}{\partial\rho\,\partial z}(G_0 + G_1 - 2Q)\right] \\ H_\varphi &= \frac{p}{4\pi}\left[\frac{\partial}{\partial\rho}(G_0 + G_1 - 2Q)\right] \quad . \end{aligned} \tag{14}$$

These general expressions were derived with no assumptions regarding proximity, wavelength, or material composition and account for the near-surface and near-field effects we aim to observe.

2.1.2. Horizontal Electric Dipole (HED)

In the case of an incremental horizontal current element placed a height h above the half plane in the x direction, Baños [41] employs the x and z components of the electric Hertz vector (i.e., $\vec{\Pi} = \vec{a}_x\Pi_x + \vec{a}_z\Pi_z$). The z components satisfy the homogeneous Helmholtz equation in each medium, and the x components satisfy the inhomogeneous Helmholtz equation in region 0 and the homogeneous Helmholtz equation in region 1. Imposition of the boundary conditions at the interface gives vector potential solutions for region 0 that are substituted into equation (5) to give field expressions. Sommerfeld formulations of the transverse-electric (TE) field components are

$$
\begin{aligned}
E_\varphi &= \frac{j\omega\mu_0 p}{4\pi k_0^{\,2}} \sin\varphi \left[\frac{1}{\rho}\frac{\partial}{\partial\rho} (G_0 - G_1 + k_0^{\,2} V) + k_0^{\,2}(G_0 - G_1 + U) \right] \\
H_z &= -\frac{p}{4\pi} \sin\varphi \left[\frac{\partial}{\partial\rho}(G_0 - G_1 + U) \right] \\
H_\rho &= \frac{p}{4\pi} \sin\varphi \left[\frac{\partial}{\partial z} (G_0 - G_1 + U) - \frac{1}{\rho}\frac{\partial W}{\partial\rho} \right] ,
\end{aligned}
\tag{15}
$$

and the transverse-magnetic (TM) field components are

$$
\begin{aligned}
E_z &= -\frac{j\omega\mu_0 p}{4\pi k_0^{\,2}} \cos\varphi \left[\frac{\partial^2}{\partial z\,\partial\rho}(G_0 + G_1 - k_1^{\,2} V) \right] \\
E_\rho &= -\frac{j\omega\mu_0 p}{4\pi k_0^{\,2}} \cos\varphi \left[\frac{\partial^2}{\partial\rho^2}(G_0 - G_1 + k_0^{\,2} V) + k_0^{\,2}(G_0 - G_1 + U) \right] \\
H_\varphi &= \frac{p}{4\pi} \cos\varphi \left[\frac{\partial}{\partial z}(G_0 - G_1 + U) - \frac{\partial^2 W}{\partial\rho^2} \right] .
\end{aligned}
\tag{16}
$$

Sommerfeld integrals U and W are defined by

$$
\begin{aligned}
U &= \int_0^\infty \frac{2\exp[-l(z+h)]}{l + m} J_0(\xi\rho)\, \xi\, \mathrm{d}\xi \\
W &= \int_0^\infty \frac{2(l-m)\exp[-l(z+h)]}{k_1^{\,2} l + k_0^{\,2} m} J_0(\xi\rho)\, \xi\, \mathrm{d}\xi \quad .
\end{aligned}
\tag{17}
$$

Note that if one were to compare the VED and HED Sommerfeld formulations given in this report to the corresponding expressions in [41], then a number of differences would be observed. These differences are due to an opposite time convention and rotation of the spatial coordinate axes. The opposite time convention causes the opposite sign in the exponent of G_0 and G_1. Rotation of the coordinate axes flips the leading sign of many of the field equations, the sign in front of z in numerous exponential exponents, and the sign of W.

2.2. Geometric Optics and Norton Surface-Wave Approximation

Special cases exist where closed-form approximations are obtainable. Geometric optics is a far-field approximation that assumes the source, observation point, and reflecting surface are many wavelengths apart. Also, the Norton surface-wave term may be used to approximate surface-wave effects when $k_0 R_0 \gg 1$ and $|k_1| > |k_0|$.

2.2.1. Vertical Electric Dipole (VED)

If the observation point is in the far field of the source, then the approximations to fields resulting from a vertical electric dipole above a half plane are given by

$$\begin{aligned} E_z &\approx -\frac{jk_0 p}{4\pi}\sqrt{\frac{\mu_0}{\varepsilon_0}}\,[\sin^2\theta_d G_0 + \Gamma_{/\!/}\sin^2\theta_r G_1 + (1-\Gamma_{/\!/})F(w)\sin^2\theta_r G_1] \\ E_\rho &\approx \frac{jk_0 p}{4\pi}\sqrt{\frac{\mu_0}{\varepsilon_0}}\,[\sin\theta_d\cos\theta_d G_0 + \Gamma_{/\!/}\sin\theta_r\cos\theta_r G_1 - (1-\Gamma_{/\!/})\Delta_0 F(w)\sin\theta_r G_1] \\ H_\varphi &\approx \frac{jk_0 p}{4\pi}\,[\sin\theta_d G_0 + \Gamma_{/\!/}\sin\theta_r G_1 + (1-\Gamma_{/\!/})F(w)\sin\theta_r G_1] \quad , \end{aligned} \tag{18}$$

where θ_d and θ_r are shown in Figures 1 and 2. The first two terms make up the GO approximation which involves the Fresnel reflection coefficient $\Gamma_{/\!/}$ (see Section 2.2.3). The third term is Norton's surface-wave approximation, which was obtained from a high-refractivity, far-field approximation to V [42]. The Norton term incorporates an attenuation function given by

$$F(w) = 1 - \sqrt{\pi w}\; e^{-w}\,\mathrm{erfc}(j\sqrt{w}) \quad . \tag{19}$$

For a homogeneous half-space the remaining variables are defined as

$$w = -\frac{jk_0 R_0}{2\sin^2\theta_r}(\cos\theta_r + \Delta_0)^2 \qquad \text{and} \qquad \Delta_0 = \frac{k_0}{k_1}\sqrt{1-\left(\frac{k_0}{k_1}\right)^2\sin^2\theta_r} \quad . \tag{20}$$

The Norton surface-wave terms are valid only when $k_0 R_0 \gg 1$ and $|k_1| > |k_0|$ due to assumptions made when deriving equations (18), (19), and (20).

2.2.2. Horizontal Electric Dipole (HED)

For observation points in the far field of a horizontal dipole above a homogeneous half plane, the TE fields are given by

$$\begin{aligned} E_\varphi &\approx \frac{jk_0 p}{4\pi}\sqrt{\frac{\mu_0}{\varepsilon_0}}\,\sin\varphi\,[G_0 + \Gamma_\perp G_1 + (1-\Gamma_\perp)F(q)G_1] \\ H_z &\approx \frac{jk_0 p}{4\pi}\,\sin\varphi\,[\sin\theta_d G_0 + \Gamma_\perp\sin\theta_r G_1 + (1-\Gamma_\perp)F(q)\sin\theta_r G_1] \\ H_\rho &\approx -\frac{jk_0 p}{4\pi}\,\sin\varphi\,[\cos\theta_d G_0 + \Gamma_\perp\cos\theta_r G_1 - (1-\Gamma_\perp)F(q)\delta_0 G_1] \quad , \end{aligned} \tag{21}$$

and the TM components in the far field are given by

$$
\begin{aligned}
E_z &\approx \frac{jk_0 p}{4\pi}\sqrt{\frac{\mu_0}{\varepsilon_0}}\cos\varphi\,[\sin\theta_d\cos\theta_d G_0 - \Gamma_{/\!/}\sin\theta_r\cos\theta_r G_1 + (1-\Gamma_{/\!/})F(w)\Delta_0\sin\theta_r G_1] \\
E_\rho &\approx -\frac{jk_0 p}{4\pi}\sqrt{\frac{\mu_0}{\varepsilon_0}}\cos\varphi\,[\cos^2\theta_d G_0 - \Gamma_{/\!/}\cos^2\theta_r G_1 - (1-\Gamma_{/\!/})F(w)\Delta_0^2 G_1] \\
H_\varphi &\approx -\frac{jk_0 p}{4\pi}\cos\varphi\,[\cos\theta_d G_0 - \Gamma_{/\!/}\cos\theta_r G_1 + (1-\Gamma_{/\!/})F(w)\Delta_0 G_1] \quad ,
\end{aligned}
\tag{22}
$$

where θ_d and θ_r are shown in Figures 1 and 2, the sum of the first two terms is the geometric optics approximation, and the third term is the Norton surface-wave term. For a homogeneous half-space the remaining variables are defined as

$$
q = -\frac{jk_0 R_0}{2\sin^2\theta_r}(\cos\theta_r + \delta_0)^2 \qquad \text{and} \qquad \delta_0 = \frac{k_1}{k_0}\sqrt{1-\left(\frac{k_0}{k_1}\right)^2\sin^2\theta_r} \quad . \tag{23}
$$

Similar to the VED case, the Norton surface-wave terms are valid only when $k_0 R_0 \gg 1$ and $|k_1| > |k_0|$. The following section provides a summary of Fresnel reflection coefficients to complete the far-field formulation of the fields radiated by incremental dipoles above a half-space.

2.2.3. Fresnel Reflection Coefficients

Detailed derivations for the expressions given in this section may be found in standard electromagnetic texts, such as [47]. Electric field polarization is defined relative to the plane of incidence, which contains the normal to the reflecting surface and the incident propagation vector (see Figures 1 and 2). Parallel polarized electric fields lie in the plane of incidence and perpendicular polarized fields are orthogonal. The *E*-field Fresnel reflection coefficients at a plane boundary are

$$
\Gamma_{/\!/} = \frac{\eta_0\cos\theta_i - \eta_1\cos\theta_t}{\eta_0\cos\theta_i + \eta_1\cos\theta_t} \qquad \text{and} \qquad \Gamma_{\perp} = \frac{\eta_1\cos\theta_i - \eta_0\cos\theta_t}{\eta_1\cos\theta_i + \eta_0\cos\theta_t} \quad , \tag{24}
$$

where the transmitted angle and intrinsic wave impedance of region 1 are complex and defined as

$$
\sin\theta_t = \frac{\eta_1}{\eta_0}\sin\theta_i \qquad \text{and} \qquad \eta_1 = \sqrt{\frac{\mu_0}{\varepsilon_r\varepsilon_0 - j\sigma/\omega}} \quad , \tag{25}
$$

respectively. Figure 3 illustrates $\Gamma_{/\!/}$ and $\Gamma_{\perp}$ for various material properties and frequencies.

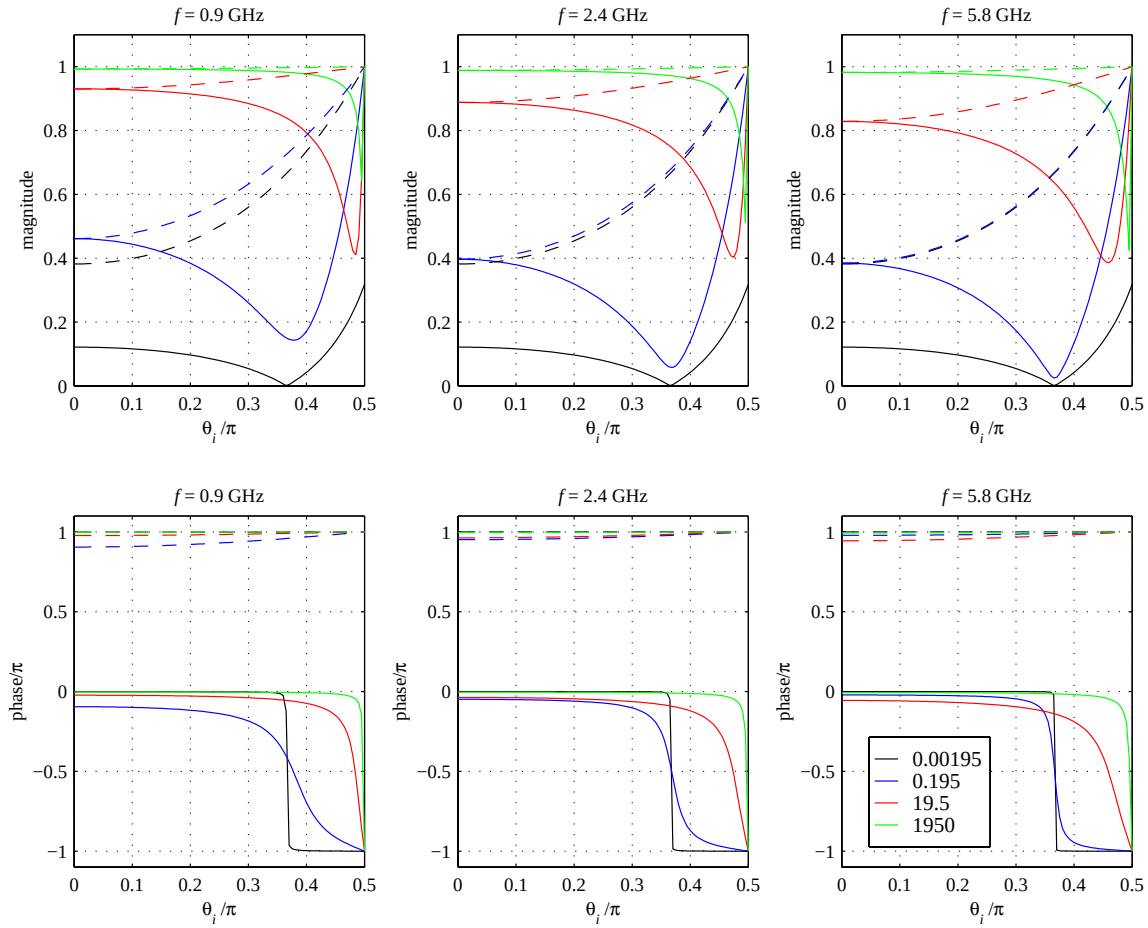

Figure 3. Parallel (line) and perpendicular (dash) Fresnel reflection coefficients versus angle of incidence for ε_r=5. Legend displays conductivity σ [S/m].

3. NUMERICAL INTEGRATION TECHNIQUES

To evaluate the accuracy of GO, we must analyze near-field interaction and propagation effects near the interface. General solutions for fields radiated by a VED or an x-aligned HED are obtained via numerical evaluation of Sommerfeld integrals. In this section, relevant numerical techniques are presented with reference to [48-52]. Romberg integration for relatively well-behaved functions and the weighted-averages method for evaluating asymptotically-oscillating slowly-convergent functions are summarized. Finally, specific details for the numerical evaluation of $2Q/k_0^2$, U, V, and W and the necessary derivatives are given.

3.1. Romberg Quadrature

Romberg integration is an effective means of integrating well-behaved integrands over a finite range of integration by extrapolating the error associated with a prediction from previous iterations and

subtracting the error to give a higher-order approximation. To demonstrate this, consider the trapezoidal rule

$$\int_{\xi_0}^{\xi_1} X(\xi)\,\mathrm{d}\xi = \Delta\xi\left[\frac{1}{2}X(\xi_0) + \frac{1}{2}X(\xi_1)\right] + O\left(\Delta\xi^3 X^{(2)}\right) \quad , \tag{26}$$

where $\Delta\xi$ is the distance between abscissae, parenthesized superscripts denote derivative order, and O defines error order. Equation (26) is a two-point formula and is exact for polynomials up to and including degree 1. If this equation is used N times for the equally-spaced intervals (ξ_0, ξ_1), (ξ_1, ξ_2), ..., (ξ_{N-1}, ξ_N) and summed, then the extended trapezoidal rule is

$$\begin{aligned} S_N = \int_{\xi_0}^{\xi_N} X(\xi)\,\mathrm{d}\xi = \Delta\xi\left[\frac{1}{2}X(\xi_0) + X(\xi_1) + \cdots + \frac{1}{2}X(\xi_N)\right] \\ - \frac{B_2(\xi_N - \xi_0)^2}{2!\,N^2}\left[X'(\xi_N) - X'(\xi_0)\right] - \cdots \\ - \frac{B_{2n}(\xi_N - \xi_0)^{2n}}{(2n)!\,N^{2n}}\left[X^{(2n-1)}(\xi_N) - X^{(2n-1)}(\xi_0)\right] - \cdots \end{aligned} \tag{27}$$

where B_n is a Bernoulli number. If one evaluates the integral with N steps and then again with $2N$ steps, then the leading error in the second evaluation will be ¼ the size of the error in the first evaluation. Therefore the combination

$$S = \frac{4}{3}S_{2N} - \frac{1}{3}S_N \tag{28}$$

subtracts off the leading error term. Similarly, Romberg integration uses Neville's algorithm to extrapolate the leading error term for high-order integrands.

3.2. Weighted-Averages Method

The weighted-averages method is a useful numerical technique for integrating functions that are periodic yet convergent over a semi-infinite integration range. Sommerfeld integrals are inherently oscillatory and slowly convergent due to the presence of Bessel functions. We begin our discussion of the weighted-averages method with the integration then summation technique [52], where the integral is expressed as a limit of a sequence of partial sums

$$S = \int_{\xi_{-1}}^{\infty} \chi(\xi) J_\upsilon(\xi\rho)\,\xi\,\mathrm{d}\xi = \lim_{N\to\infty} \sum_{n=0}^{N} \int_{\xi_{n-1}}^{\xi_n} \chi(\xi) J_\upsilon(\xi\rho)\,\xi\,\mathrm{d}\xi = \lim_{N\to\infty} S_N \quad . \tag{29}$$

Note that the Sommerfeld integrand was split into its characteristic factors, $X(\xi) = \chi(\xi) J_\upsilon(\xi\rho)\xi$. Also, ξ_{-1} is chosen to ensure that no singularities exist in the Sommerfeld tail $X(|\Re\xi| > |\xi_{-1}|)$. The sequence S_N approaches S slowly and the error or remainder complies with the following expression

$$\begin{aligned} r_N &= S_N - S = -\int_{\xi_N}^{\infty} \chi(\xi) J_\upsilon(\xi\rho)\,\xi\,\mathrm{d}\xi \\ &\sim w_N \sum_{n=0}^{\infty} c_n \xi_N^{-n} \quad , \qquad N \to \infty \quad , \end{aligned} \tag{30}$$

where w_N are remainder estimates specific to $\chi(\xi)$. Series acceleration methods are based on the idea that information contained in the sequence of partial sums, $S_0, S_1, \ldots, S_N$, is extracted and utilized in a way that is more efficient than the conventional combination techniques. If the weight, W_N, is associated with S_N, then a general combination formula is

$$S_N' = \frac{W_N S_N + W_{N+1} S_{N+1}}{W_N + W_{N+1}} = S + \frac{W_N r_N + W_{N+1} r_{N+1}}{W_N + W_{N+1}} = S + r_N' \quad . \tag{31}$$

The second form shows that if

$$\alpha_N \equiv \frac{W_{N+1}}{W_N} = -\frac{r_N}{r_{N+1}} \quad , \tag{32}$$

then the remainder r_N' of the transformed sequence will be nullified. The difficulty is determining r_N from its asymptotic estimates. Careful scrutiny leads to the generalized weighted-averages algorithm, given as

$$S_N^{(\ell+1)} = \frac{S_N^{(\ell)} + \alpha_N^{(\ell)} S_{N+1}^{(\ell)}}{1 + \alpha_N^{(\ell)}} \qquad (N \geq 0 \text{ and } \ell \geq 0) \quad , \tag{33}$$

where parenthesized superscripts denote transformation order and $\alpha_N^{(\ell)}$ is formulated in Section 3.3 for the integrands under consideration. Equation (33) is a recursive scheme that produces $S_0^{(\ell)}$ as the best approximation to S, given the partial sums $S_0, S_1, \ldots, S_\ell$, and accelerates the convergence.

3.3. Numerical Evaluation of $2Q/k_0^2$, U, V, and W

Efficient numerical integration of the integrals associated with dipole radiation above a half plane are now considered. Table 1 summarizes the necessary Sommerfeld integrals and Figure 4 illustrates the common traits among each integrand in the complex plane. Derivatives were pulled inside the

Table 1. Sommerfeld Integrands and Asymptotic Coefficients

Sommerfeld integral	Sommerfeld integrand, X	asymptotic
$\frac{2Q}{k_0^2}$	$\frac{2m\exp[-l(z+h)]}{l(k_0^2 m + k_1^2 l)} J_0(\xi\rho)\xi$	1
$\frac{\partial^2}{\partial z^2}\left(\frac{2Q}{k_0^2}\right)$	$\frac{2lm\exp[-l(z+h)]}{k_0^2 m + k_1^2 l} J_0(\xi\rho)\xi$	-1
$\frac{\partial^2}{\partial z\partial\rho}\left(\frac{2Q}{k_0^2}\right)$	$\frac{2m\exp[-l(z+h)]}{k_0^2 m + k_1^2 l} J_1(\xi\rho)\xi^2$	-1
$\frac{\partial}{\partial\rho}\left(\frac{2Q}{k_0^2}\right)$	$-\frac{2m\exp[-l(z+h)]}{l(k_0^2 m + k_1^2 l)} J_1(\xi\rho)\xi^2$	0
$\frac{\partial^2 V}{\partial z\partial\rho}$	$\frac{2l\exp[-l(z+h)]}{k_0^2 m + k_1^2 l} J_1(\xi\rho)\xi^2$	-1
$\frac{\partial V}{\partial\rho}$	$-\frac{2\exp[-l(z+h)]}{k_0^2 m + k_1^2 l} J_1(\xi\rho)\xi^2$	0
$\frac{\partial^2 V}{\partial\rho^2}$	$\frac{2\exp[-l(z+h)]}{k_0^2 m + k_1^2 l}\left[\frac{J_1(\xi\rho)}{\rho} - \xi J_0(\xi\rho)\right]\xi^2$	0, -1
U	$\frac{2\exp[-l(z+h)]}{l+m} J_0(\xi\rho)\xi$	1
$\frac{\partial U}{\partial z}$	$-\frac{2l\exp[-l(z+h)]}{l+m} J_0(\xi\rho)\xi$	0
$\frac{\partial U}{\partial\rho}$	$-\frac{2\exp[-l(z+h)]}{l+m} J_1(\xi\rho)\xi^2$	0
$\frac{\partial W}{\partial\rho}$	$-\frac{2(l-m)\exp[-l(z+h)]}{k_0^2 m + k_1^2 l} J_1(\xi\rho)\xi^2$	-1
$\frac{\partial^2 W}{\partial\rho^2}$	$\frac{2(l-m)\exp[-l(z+h)]}{k_0^2 m + k_1^2 l}\left[\frac{J_1(\xi\rho)}{\rho} - \xi J_0(\xi\rho)\right]\xi^2$	-1, -2

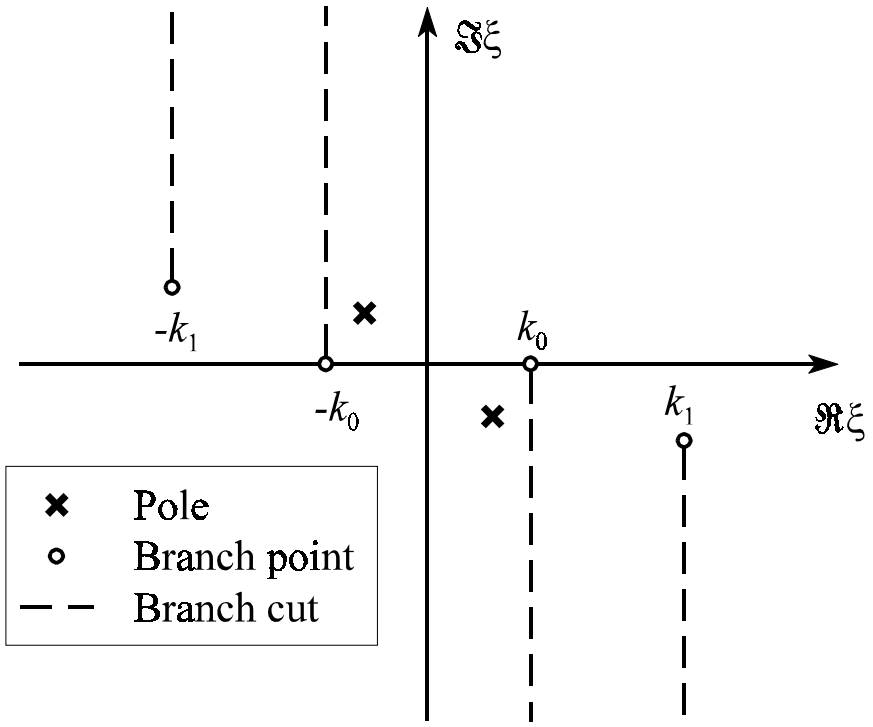

Figure 4. Sommerfeld poles and branch points in complex plane.

integrals and each resulting Sommerfeld integrand, X, contains Bessel functions, exponential terms, branch cuts, and possible poles. These factors make analytic solutions unlikely, but provide a commonality which allows for a single numerical integration scheme to evaluate all of the integrals. In this approach the real-axis integration path is partitioned and specific numerical integration techniques are used according to the integrand behavior in each subinterval.

Poles may cause strong variations in the integrand, such as those associated with V and W at

$$\xi_{pole} = \frac{\pm k_0 k_1}{\sqrt{k_0^2 + k_1^2}} \quad . \tag{34}$$

These poles are located in the fourth quadrant on the complex plane just below the real axis and $\Re(\xi_{pole}) \le k_0$ as well as in the second quadrant symmetric about the origin. It was confirmed that they have negligible effect on the real-axis integration path for the electric properties considered.

To avoid branch cuts, the integration path was partitioned into three subintervals $[0, k_0]$, $[k_0, k_0\sqrt{\varepsilon_r}]$, and $[k_0\sqrt{\varepsilon_r}, \infty]$, where different techniques were used according to specific difficulties encountered. In the first subinterval, change of variables $\xi = k_0 \cos u$ removed the discontinuity in the derivative at k_0, resulting in

$$\int_0^{k_0} X(\xi)\,\mathrm{d}\xi = \int_0^{\frac{\pi}{2}} X(k_0 \cos u)\, k_0 \sin u\,\mathrm{d}u \quad . \tag{35}$$

In the second subinterval, change in variable $\xi = k_0 \cosh v$ removed the discontinuity at k_0 giving

$$\int_{k_0}^{k_0\sqrt{\varepsilon_r}} X(\xi)\,\mathrm{d}\xi = \int_0^{\mathrm{Arccosh}\sqrt{\varepsilon_r}} X(k_0 \cosh v)\, k_0 \sinh v\,\mathrm{d}v \quad . \tag{36}$$

The integrands in equations (35) and (36) are well behaved and converge when numerically integrated with Romberg quadrature.

The semi-infinite subinterval was chosen to begin at $\xi_{-1} = k_0\sqrt{\varepsilon_r}$ because all singularities, poles, and branch points on the right half of the complex plane lie either on or to the left of the line defined by $\Re(\xi) = k_0\sqrt{\varepsilon_r}$. Change in variable was not necessary and the generalized weighted-averages algorithm was used to numerically integrate the Sommerfeld integral tail. The break points $\xi_N = k_0\sqrt{\varepsilon_r} + N\pi/\rho$ were chosen based on the half-period of the Bessel function, π/ρ, and the weights were chosen according to the analytical form of the remainder estimates, given by

$$w_N = \frac{(-1)^{N+1}}{\xi_N^{\beta-\frac{1}{2}}} \exp\left[-\frac{N\pi(z+h)}{\rho}\right] \quad . \tag{37}$$

A more detailed derivation of equation (37) was given by Michalski in [52]. This equation is based on the asymptotic behavior of the Sommerfeld integrand, which is characterized by the asymptotic coefficient β (given in Table 1) and the expressions

$$\begin{aligned} f(\xi) &\sim \frac{\exp[-\xi(z+h)]}{\xi^{\beta}}\left[C + O(\xi^{-1})\right] \\ J_{\upsilon}(\xi\rho) &\sim \sqrt{\frac{2}{\pi\xi\rho}} \cos\left(\xi\rho - \upsilon\frac{\pi}{2} - \frac{\pi}{4}\right) \quad , \end{aligned} \tag{38}$$

where C is a constant. Applying equation (37) to equations (30) and (32) gives

$$\alpha_N^{(\ell)} = \exp\left[\frac{\pi(z+h)}{\rho}\right]\left(\frac{\xi_{N+1}}{\xi_N}\right)^{\beta-\frac{1}{2}+\ell} \quad , \tag{39}$$

which completes the weighted-averages formulation given by equation (33).

4. FREQUENCY-DOMAIN RESULTS

In this section, field-strength results and corresponding GO errors are illustrated in the frequency domain. Frequencies ranging from 10 to 8000 MHz (i.e., $30 \geq \lambda \geq 0.0375$ m) were chosen to encompass the ISM bands at 902 - 928 MHz, 2.4000 - 2.4835 GHz, and 5.725 - 5.850 GHz where unlicensed wireless LAN products operate [53]. In order for the theoretical received signals to embody the channel transfer function, we simulate a flat-frequency transmitted spectrum by defining the electric dipole moment as

$$p = j\frac{4\pi}{\omega\mu_0} \quad . \tag{40}$$

First, VED results from a simple two-ray geometry at various ground conductivities are presented to introduce the behavior of the two-ray model. Next, position dependency is investigated to isolate near-surface and near-field effects. Lastly, field strength as a function of horizontal separation and frequency is displayed in order to demonstrate the nature of the fields in a more general sense. Throughout this report, superscripts (i.e., E_z^S, E_z^{GO}, E_z^{GO+N}) and colors (i.e., green, red, blue) are used to distinguish between Sommerfeld, GO, and GO with Norton term results, and all fields are in dB normalized to 1 V/m for *E*-fields or 1 A/m for *H*-fields. Note that in many cases the curves are indistinguishable because they lie on top of one another.

4.1. Conductivity Variation to Demonstrate Two-Ray Behavior

Electric properties are defined by the conductivity and relative dielectric constant of the lossy half space; geometry is specified by height above the interface and horizontal separation. In this section, we consider $\{\sigma\,[\text{S/m}]\} = \{0.00195, 0.195, 19.5, 1950\}$, $\varepsilon_r = 5$, and $\{h\,[\text{m}], z\,[\text{m}], \rho\,[\text{m}]\} = \{1, 1, 10\}$ in order to minimize the effect of the null in the radiation pattern of the VED source and to ideally illustrate the nature of the two-ray model. Figure 5 presents the numerically approximated Sommerfeld solution with the GO approximation for the squared magnitude of E_z radiated by a VED.

As the electrical conductivity gets large, the Fresnel reflection coefficients approach plus or minus unity and the field expressions approach the sum of the source and image Green's functions $G_0 + G_1$. This produces a two-ray cancellation effect where equally spaced nulls occur according to the difference in path lengths, $\Delta R = R_1 - R_0$. At lower conductivities, the reflected wave is less influential because the Fresnel reflection coefficient decreases in magnitude and shifts in phase, thus flattening the cancellation behavior and shifting the nulls in frequency. Geometry associated with the above case effectively demonstrates the behavior of a two-ray model and its dependence on material properties. For practical purposes, we limit the scope of the remainder of this analysis to reflecting surfaces made of concrete. Although the electric properties of concrete vary with frequency [54], we assume that frequency-independent parameters (i.e., $\varepsilon_r = 5$ and $\sigma = 0.00195$ S/m) will provide representative results.

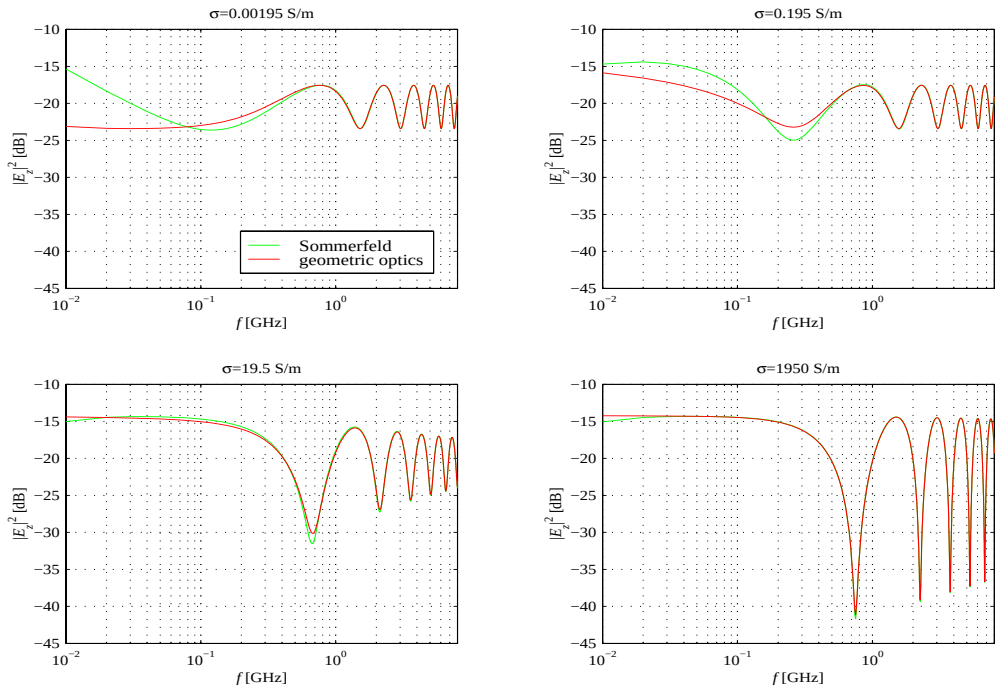

Figure 5. Magnitude squared of the z component of the E-field for a VED above a half space (z=1 m, h=1 m, ρ=10 m, ε_r=5) at various conductivities.

4.2. Position Variation to Isolate Near-Surface and Near-Field Effects

In this section, we position the source and observation points to isolate near-surface and near-field effects. Figures 6 and 7 illustrate fields radiated by a VED above a half plane, Figures 8 and 9 isolate the TE waves of an x-aligned HED by limiting the observation points to $\varphi = 90°$, and Figures 10 and 11 isolate the TM waves of an x-aligned HED by limiting the observation points to $\varphi = 0°$.

For incremental electric dipoles, simulations show that near-field effects are substantially reduced for $\rho > 1$ m excluding the E_ρ component of the HED-TM case; hence, we isolate near-surface effects by holding the horizontal separation constant at 5 m and simultaneously reducing the source and observation heights: {(h [m], z [m], ρ [m])} = {(10, 10, 5), (1, 1, 5), (0.1, 0.1, 5), (0.01, 0.01, 5)}. It should be understood that near-field regions depend on antenna size and that ideal infinitesimal dipole sources are non-realizable. Figures 6, 8, and 10 demonstrate surface effects on field strength and Sections 4.2.1 and 4.2.2 provide relevant observations and discussion.

It is shown later that for an elementary electric dipole above a concrete half plane, surface effects are significantly reduced when $h \geq 10$ m and $z \geq 10$ m. Therefore, we isolate near-field effects by holding the source and observation points at a constant height of 10 m and reducing the horizontal separation: {(h [m], z [m], ρ [m])} = {(10, 10, 10), (10, 10, 1), (10, 10, 0.1), (10, 10, 0.01)}. Figures 7, 9, and 11 illustrate near-field effects in the frequency domain, and Section 4.2.3 provides analyses.

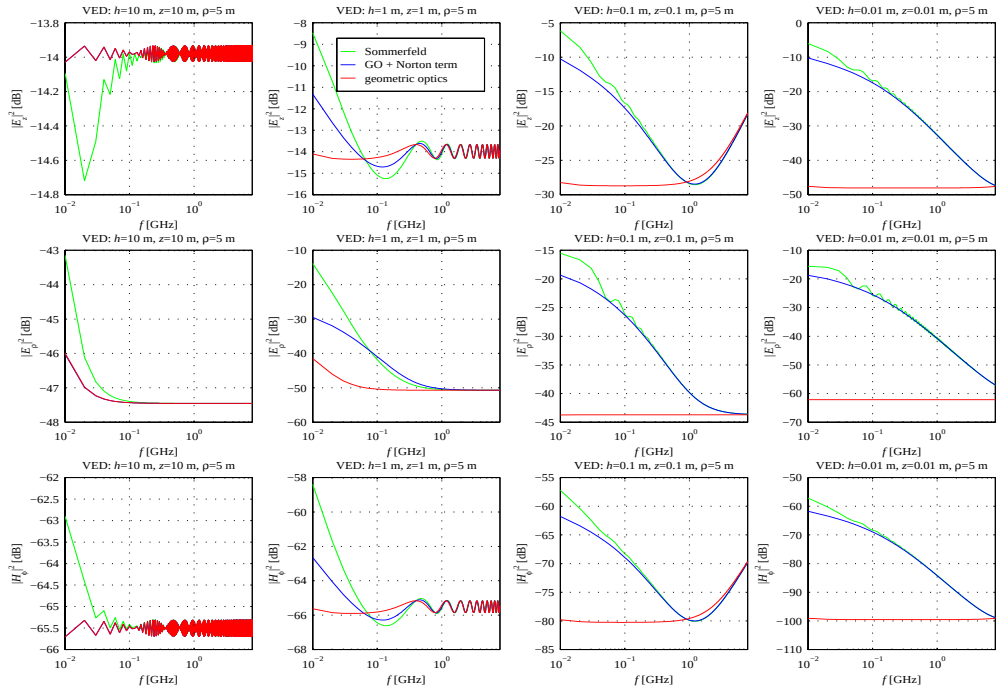

Figure 6. Near-surface effects on field strength of a VED above a concrete half space.

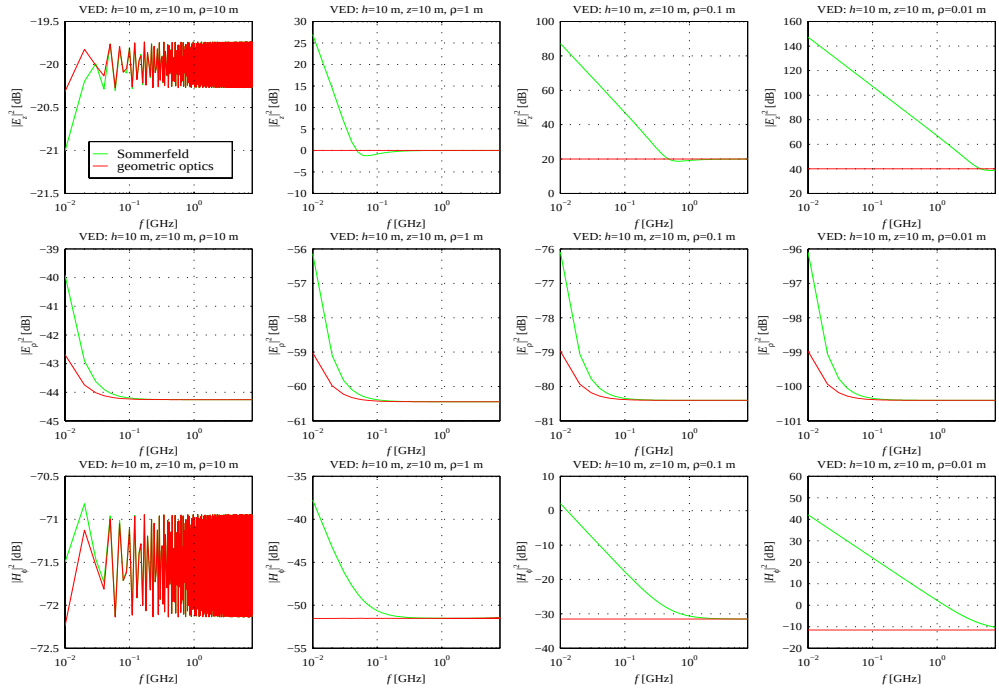

Figure 7. Near-field effects on field strength of a VED above a concrete half space.

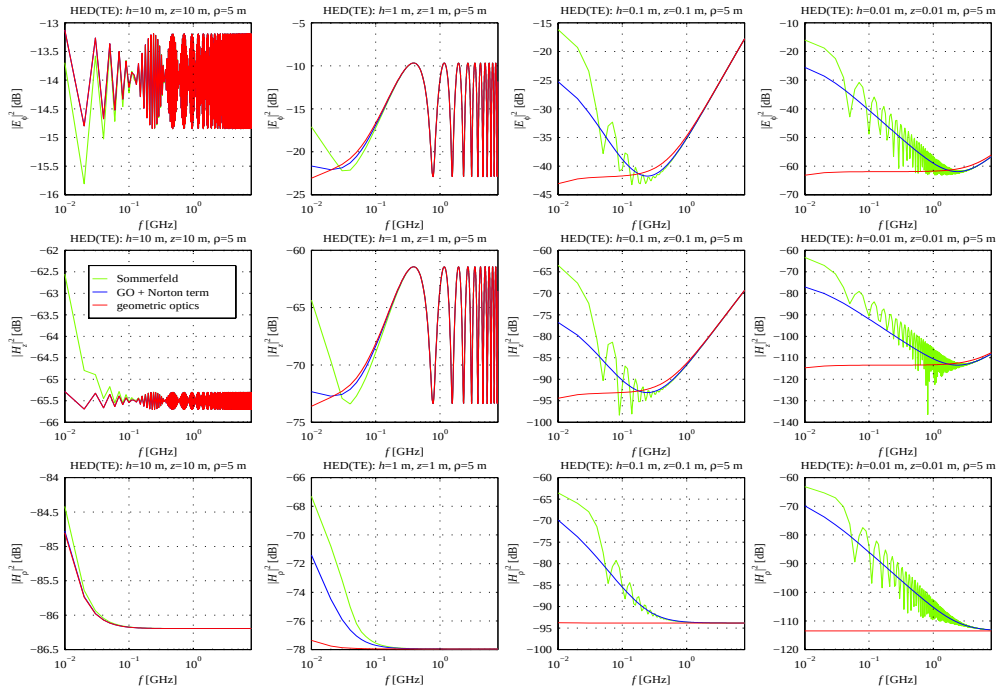

Figure 8. Near-surface effects on field strength of an x-aligned HED above a concrete half space. Observation points are restricted to φ=90°.

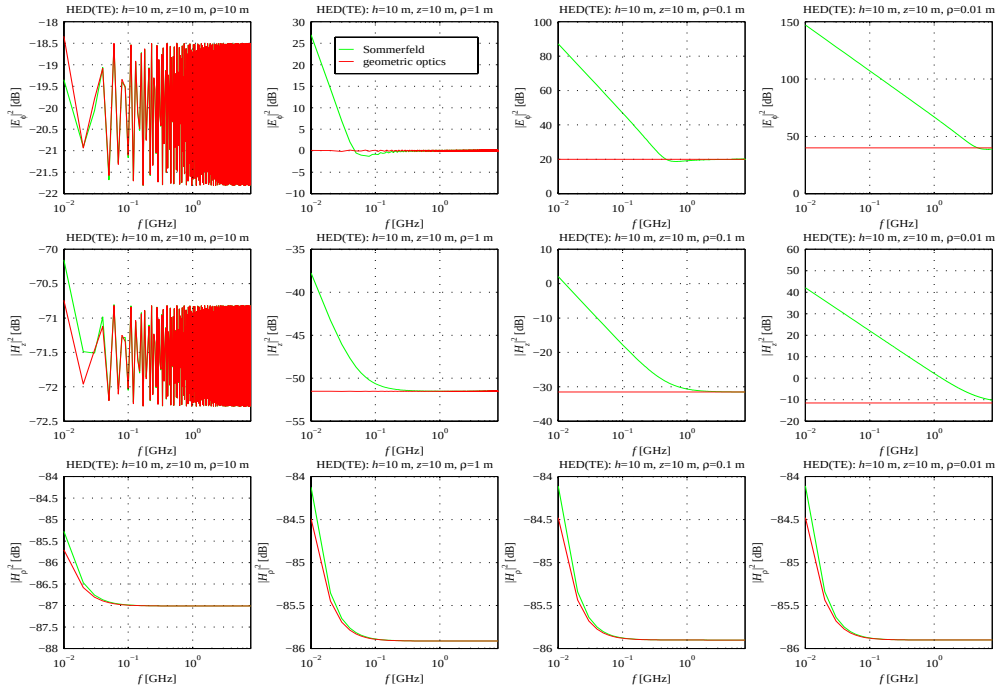

Figure 9. Near-field effects on field strength of an x-aligned HED above a concrete half space. Observation points are restricted to φ=90°.

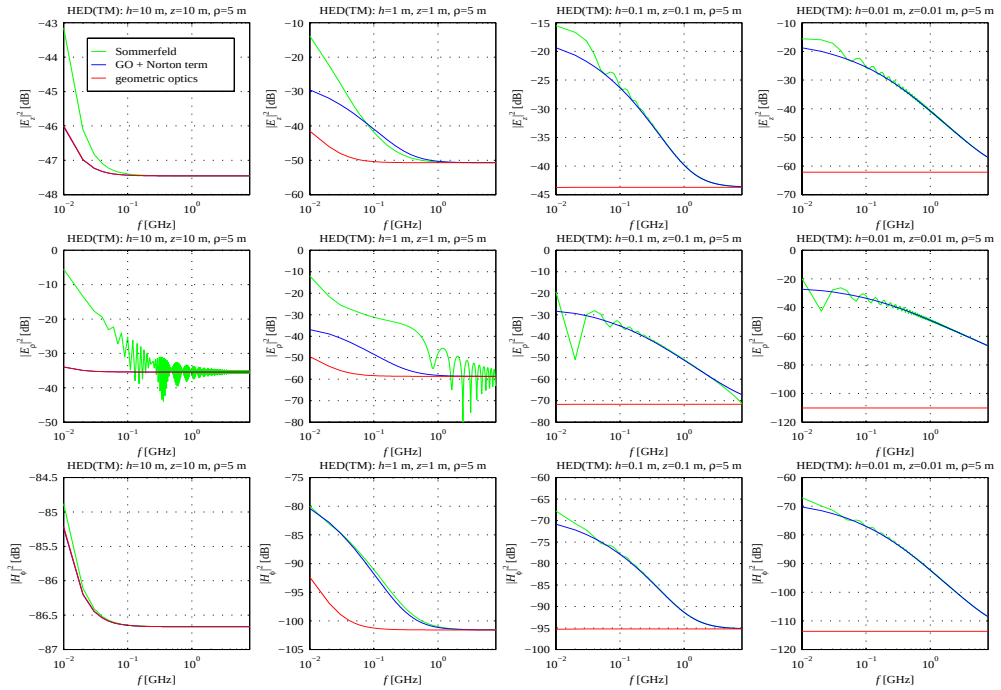

Figure 10. Near-surface effects on field strength of an x-aligned HED above a concrete half space. Observation points are restricted to φ=0°.

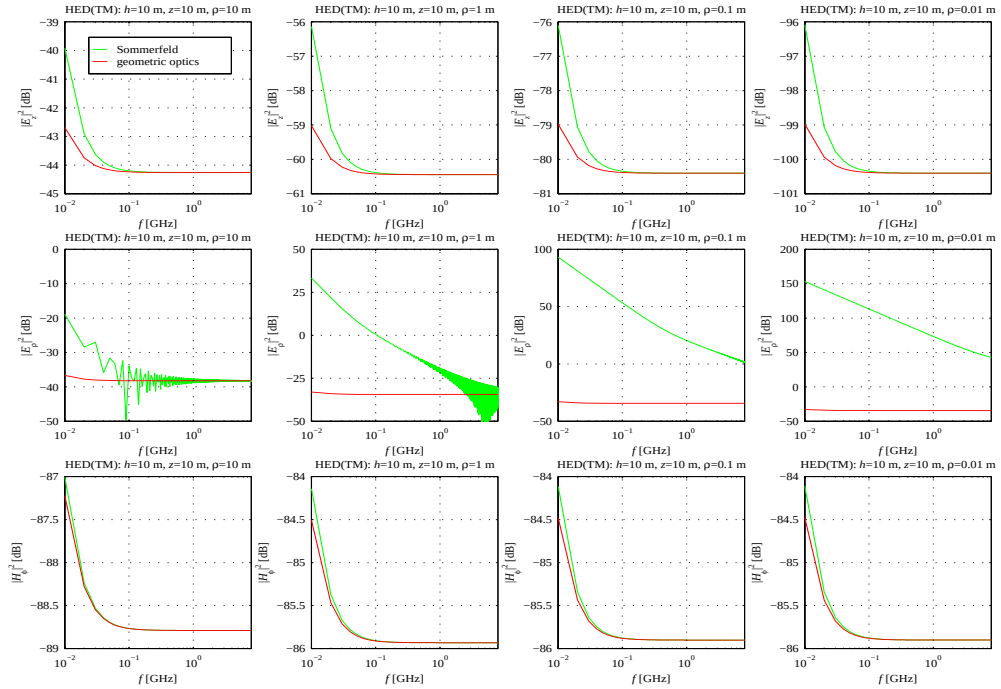

Figure 11. Near-field effects on field strength of an x-aligned HED above a concrete half space. Observation points are restricted to φ=0°.

4.2.1. Surface Wave

Figures 6, 8, and 10 illustrate near-surface effects as the source and observation points are drawn close to the interface. Norton surface-wave terms provide a means to isolate surface-wave effects. Near the interface, deviation from geometric optics due to surface-wave propagation peaks near d.c. and decreases continuously with increasing frequency. As expected, surface-wave propagation is more influential in TM fields than in TE fields radiated by HED. In comparison to the more general Sommerfeld solution, GO + Norton term approximations seem adequate for predicting the radiation of a VED above a half-plane; significant discrepancies, however, appear in the HED case where near-field effects are influential, as discussed in the following sections.

4.2.2. Pseudo-Lateral Wave

Sommerfeld results in Figure 8 show strong oscillations in the TE fields radiated by an x-aligned HED over a wide range of frequencies when the source and observation point are near the interface (i.e., $h \le 0.01$ m and $z \le 0.01$ m). In this section, we provide alternative expressions for U, V, and W to help explain this oscillation.

Notice that the HED-TE fields in equation (15) are strongly influenced by the integral U. With reference to [55], rationalization of the denominator in U and use of the integral representation of G_1 in equation (8) allows for it to be rewritten as

$$U = \frac{2}{k_1^2 - k_0^2}\left[\frac{\partial^2 G_1}{\partial z^2} - \int_0^\infty m \exp[-l(z+h)] J_0(\xi\rho)\,\xi\,\mathrm{d}\xi\right] . \tag{41}$$

If we add and subtract 1 within the integrand and make use of

$$\int_0^\infty m J_0(\xi\rho)\,\xi\,\mathrm{d}\xi = \frac{\partial^2}{\partial z^2}\frac{\exp[-jk_1R_1]}{R_1}\bigg|_{z=h=0} , \tag{42}$$

then U can be expressed as

$$U = \frac{2}{k_1^2 - k_0^2}\left[\frac{\partial^2 G_1}{\partial z^2} - \frac{\partial^2}{\partial z^2}\frac{\exp(-jk_1R_1)}{R_1}\bigg|_{z=h=0} - \int_0^\infty m\{\exp[-l(z+h)] - 1\} J_0(\xi\rho)\,\xi\,\mathrm{d}\xi\right] . \tag{43}$$

Close to the interface the integral term is relatively small and the first two terms depict two waves traveling adjacent to one another but at different speeds due to the different propagation media. The two waves destructively interfere when $-k_0R_1 \approx -k_1R_1 + 2\pi n$, where n is an integer. For the material properties chosen and $R_1 = 5$ m, the interference occurs approximately every 48.5 MHz which agrees

with the oscillation observed. The interference caused by the adjacent fields dies off as the source and observation point are moved away from the surface, which suggests near-field excitation for generating the pseudo-lateral wave.

By the same motivation, an alternative form of the Sommerfeld integral V is derived with reference to [55]. As in the approach used in reformulating U, we add and subtract 1 within the integrand in equation (10). The denominator of V cannot be rationalized as with U, but the integral identity

$$\int_{k_0/k_1}^{k_1/k_0} \frac{v\,\mathrm{d}v}{\sqrt{(\xi^2-\xi_{pole}^2)v^2-\xi_{pole}^2}} = \frac{k_1^4-k_0^4}{k_1 k_0}\frac{1}{k_1^2 l + k_0^2 m} \quad , \tag{44}$$

allows for integration by parts, which produces two additive exponential terms. Finally, change in variable and identification of the integral form of the incomplete Hankel function, given by

$$H_0^{(1)}(k_1/k_0,\xi\rho) = \frac{2}{j\pi}\int_0^{k_1/k_0} \frac{\exp(j\xi\rho\sqrt{1+u^2})}{\sqrt{1+u^2}}\,\mathrm{d}u \quad , \tag{45}$$

completes the derivation and yields

$$\begin{aligned} V = {} & \frac{2k_1k_0}{k_1^4-k_0^4}\left\{\frac{k_1}{k_0}\frac{\exp(-jk_1\rho)}{\rho} - \frac{k_0}{k_1}\frac{\exp(-jk_0\rho)}{\rho} - \frac{\pi}{2}\xi_{pole}\left[H_0^{(1)}(k_1/k_0,\xi_{pole}\rho) - H_0^{(1)}(k_0/k_1,\xi_{pole}\rho)\right]\right\} \\ & + \int_0^{\infty} \frac{2\{\exp[-l(z+h)]-1\}}{lk_1^2+mk_0^2} J_0(\xi\rho)\,\xi\,\mathrm{d}\xi \quad , \end{aligned} \tag{46}$$

where the positive form of equation (34) is used for ξ_{pole}. Values for incomplete Hankel functions may be attained via numerical expansion. A useful relation given by

$$W = -\frac{\partial}{\partial z}\left[2G_1 - (k_0^2+k_1^2)V\right] \quad , \tag{47}$$

provides the means for expressing the last Sommerfeld integral W in terms of V.

The leading terms of equations (43) and (46) show evidence of a pseudo-lateral wave, which originates in the less dense media and propagates along the surface; it travels inside the dielectric and is excited via near-field coupling. This phenomenon resembles the lateral wave that has application in geophysical exploration of the lithosphere [56] and propagation modeling in highly vegetated environments [57]. Lateral waves are excited along a boundary between two media by a source either at the interface or in the dense medium and travel atop the interface in the less dense medium. In Section 5, time-domain results will also illustrate the pseudo-lateral wave phenomenon, where a pulse arrival time corresponding to the wave velocity of the dense media is shown.

4.2.3. Near-Field Effects on the Direct Ray

Electromagnetic fields in the near-field region were computed via numerical evaluation of Sommerfeld integrals and compared to GO approximations in Figures 7, 9, and 11. Note that Norton surface wave approximations are not included in these plots because they are valid only in the far field. As separation decreases to $\rho < \lambda$, the direct ray is observed in the near field of the source, and field components influenced by the direct ray (i.e., E_z and H_φ for VED and E_φ and H_z for HED-TE) demonstrate deviation from the GO approximation at low frequencies due to near-field effects. At $h = z = 10$ m, the reflected ray travels well into the far field of the source before being reflected and observed; consequently, field components influenced by the reflected ray and not the direct ray (i.e., E_ρ for VED, H_ρ for HED-TE, and E_z and H_φ for HED-TM) show little near-field error.

The fields of the direct ray may be expressed in spherical coordinates as

$$
\begin{aligned}
E_r &= \frac{p}{2\pi {R_0}^2}\sqrt{\frac{\mu_0}{\varepsilon_0}}\cos\theta_d\left[1+\frac{1}{jk_0R_0}\right]\exp(-jk_0R_0)\\
E_\theta &= \frac{jk_0p}{4\pi R_0}\sqrt{\frac{\mu_0}{\varepsilon_0}}\sin\theta_d\left[1+\frac{1}{jk_0R_0}-\frac{1}{(k_0R_0)^2}\right]\exp(-jk_0R_0) \qquad (48)\\
H_\varphi &= \frac{jp}{4\pi R_0}\sin\theta_d\left[1+\frac{1}{jk_0R_0}\right]\exp(-jk_0R_0) \quad .
\end{aligned}
$$

Notice that E_r is strictly a near- and intermediate-field expression with an $\exp(-jk_0R_0)$ phase dependence that is not accounted for in the geometric optics expressions. If $\theta_d = 0°$, then E_r is equivalent to the direct-ray of E_ρ in the HED-TM case and near-field influence is maximized in the null of the antenna pattern because the $\cos\theta_d$ factor is equal to 1. In Figures 10 and 11, the E_ρ component of the HED-TM radiated field displays an oscillatory deviation from the GO + Norton term approximation when locations are many wavelengths from the interface and from each other. In this scenario, the near-field direct ray is comparable in magnitude to the reflected ray, hence causing a near-field direct ray plus a GO reflected ray cancellation pattern. Further discussion is given in the time-domain results section where the results are more intuitive.

4.3. Contour Plots to Observe Two-Ray Behavior

We assigned the field strength and corresponding GO error to colors and plotted those colors versus frequency and horizontal separation for constant h and z; this allows us to visualize the results in a more general sense. Appendix A displays numerical solutions to Sommerfeld formulations, residual errors (i.e. $||E_z^S|^2 - |E_z^{GO}|^2|$ [dB]), and dashed lines on the residual error plots representing the $R_0 = 10\lambda$ contour to provide a geometric guideline. Note that these results have low resolution in frequency, so highly oscillatory behavior may not be seen.

Half the figures in Appendix A present cases where the source and observation points lie on the same horizontal plane {(h [m], z [m])} = {(10, 10); (1, 1); (0.1, 0.1); (0.01, 0.01)}. In these plots, observe the decrease in two-ray cancellation frequency with increasing ΔR (i.e., constant ρ and decreasing height) when the direct and reflected rays are both present. Also notice the error magnification near the Brewster angle. The remaining figures in Appendix A give representative contour plots for source and observation points at different heights {(h [m], z [m])} = {(1, 10); (0.1, 10); (0.1, 1); (0.01, 1)}. Notice the effect of the source antenna pattern; that is, if the observation point is not at a null in an antenna pattern, then the two-ray cancellation effect becomes visible.

5. TIME-DOMAIN ANALYSIS

Field strength plots in the frequency domain are descriptive, but the practical significance of the results are difficult to interpret. Of more importance to the digital communications engineer is how the errors translate to the time domain. In order to assess the practical significance of GO error for indoor scenarios, we compute the delay spread of the channel impulse response and quantify the cumulative error seen in the frequency domain. This section provides a detailed explanation of the time-domain analyses used in this report.

Digital signals are typically transmitted by some type of carrier modulation. The transmitted signal is limited in bandwidth to an interval of frequencies centered around the carrier or center frequency (i.e., $\omega_c = 2\pi f_c$) and must be real-valued in the time domain in order to have a physical interpretation; consequently, it is complex-conjugate symmetric about d.c. in the frequency domain. For mathematical convenience with no loss in generality, the passband signal may be expressed as a complex-baseband representation. This is accomplished by first filtering out the negative frequencies to produce an analytic signal. In the time domain, the real and imaginary parts of the analytic signal are a Hilbert transform pair. Next, we shift the analytic signal down to baseband to give a complex-baseband representation of the original passband signal. A pictorial representation of real-time, analytic, and complex-baseband signals is given in Figure 12 and more extensive discussions can be found in [58, 59].

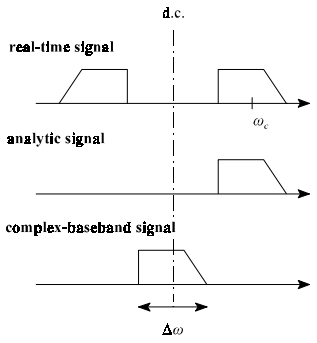

Figure 12. Signal representations.

The impulse response of the channel can be given by

$$g(t,\tau) = \vec{v} \cdot \begin{cases} \vec{e}(t,\tau) \\ \vec{h}(t,\tau) \end{cases} , \tag{49}$$

where $\vec{v}$ is a unit direction vector corresponding to the receive antenna. The complex-baseband representation of the applicable vector field components, $\vec{e}(t,\tau)$ and $\vec{h}(t,\tau)$, is given by

$$\begin{aligned} \vec{e}(t,\tau) &= \mathrm{FT}^{-1}[\vec{E}(t,\omega+\omega_c)\Lambda(\omega+\omega_c)] \\ \vec{h}(t,\tau) &= \mathrm{FT}^{-1}[\vec{H}(t,\omega+\omega_c)\Lambda(\omega+\omega_c)] \quad , \end{aligned} \tag{50}$$

where FT^{-1} is the inverse Fourier transform operator, τ is the transform variable, and $\Lambda(\omega)$ is a scalar window function that filters out negative frequencies and defines pulse shape and bandwidth.

We seek an expression for the squared magnitude of the impulse response $|g(t,\tau)|^2$ in terms of electric and magnetic field variables in order to compute delay spread via equations (2) and (3). Depending on the type and orientation of the receive antenna, one or some combination of the field components will be the dominant coupling mechanism. Orientation, radiation pattern, and efficiencies of the receive antenna are fairly arbitrary and only clutter the field effects we wish to observe. For simplification purposes, we examine each field component at the observation point separately. This augments the influence of the propagation mechanisms, generalizes the results, and allows for flexible receive antenna specification to be easily realized. In the following subsections, we discuss optimal pulse shapes and frequency considerations for indoor scenarios.

5.1. Windowing Techniques to Optimize Pulse Shape

In this section we address time-domain pulse shaping issues associated with the choice of $\Lambda(\omega)$. It is desirable to choose a window that produces a well-behaved pulse shape for large dynamic ranges. The single-ray scenario (i.e., source and observation points existing in infinite space) allows us to analyze delay spread sensitivity to threshold for a given pulse shape. We computed a single-ray impulse response and its corresponding delay spread as a function of threshold (i.e., 0 to 40 dB below the peak) for four windows (i.e., flat, Hanning, Hamming, and Blackman). Results are shown in Figure 13. As expected, the behavior of the flat window is undesirable because of its high sidelobes in the time-domain and sensitivity to threshold. If one considers threshold levels between 20 and 40 dB then the Hamming window is optimal because it has the most narrow well-behaved pulse shape. Henceforth, the Hamming window is applied to all results. Use of non-rectangular windows allows us to speak in terms of bandwidth *BW* (i.e., 3-dB bandwidth). For a Hamming window, bandwidth is about 35% of the total frequency content.

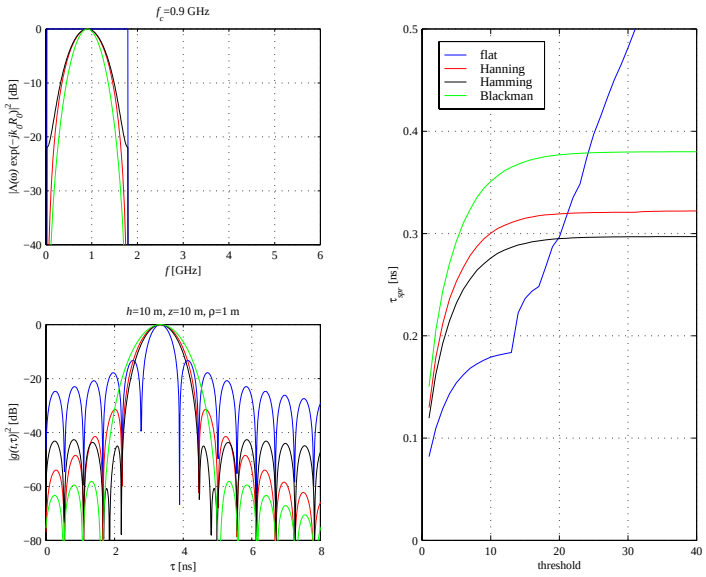

Figure 13. Windows, pulse shapes, and single-ray delay spread versus threshold.

5.2. Practical Bandwidth Limitations

We aim to describe how radio-propagation channels limit communication system performance. Simulation and measurement of broader frequency bands produce narrower pulses and more effectively distinguish multipath contributors as well as subtle near-surface and near-field effects. Consequently, the resulting impulse response contains more information and is a more general description of the channel. Here we consider a pragmatic upper limit to bandwidth.

Current WLAN systems operate within allocated bands with less than 100 MHz bandwidth. Broader bandwidths are achievable and are in demand. In order to extend the relevance of this study, we do not limit our focus to allocated operational bandwidths. It is reasonable, however, to confine simulation bandwidths to those achievable by wideband measurement systems, which are hardware limited. Typically, impulse response measurement systems are limited by the digitizer's analog bandwidth, which is on the order of 1 GHz [60]. Henceforth, we limit our simulation bandwidth to 1 GHz, impose the frequency constraint $0 < f < 2f_c$ to avoid overlap into negative frequencies, and limit the center frequency to $900 \le f_c \le 5800$ MHz. Notice that if $f_c \le 1.35$ GHz, then the bandwidth is limited by the $0 < f < 2f_c$ constraint (e.g., the 900-MHz signal shown in Figure 13).

It should also be noted that results are computed at discrete frequencies, and if too few points are used then the noise floor rises in the time domain due to the correlating nature of the inverse Fourier transform in equation (50). The frequency step dictates the pulse repetition rate of the transformed signal according to $PRR = 1/f_{step}$, and should be chosen so that influential multipath components arrive before the repetition rate elapses. The maximum dimension considered in this report is 10 m; therefore, a frequency step of 10 MHz (i.e., PRR = 100 ns) is sufficient for two-dimensional scenarios because the maximum delay is approximately $\tau_{max} = (20^2 + 10^2)^{½} \div 3\text{x}10^8 \approx 75$ ns.

6. TIME-DOMAIN RESULTS

Time-domain results corresponding to previously specified geometries are presented in this section. First, we consider the worse-case scenario (i.e., f_c = 900 MHz, $BW \approx$ 600 MHz) by maximizing the influence of low frequencies. This illustrates propagation effects in the time domain and their influence on delay spread. Next, we shift the center frequency up into the next relevant bands to demonstrate f_c and BW dependence. Delay spread versus center frequency and bandwidth is presented in order to assess the practical significance of errors associated with GO approximations for indoor scenarios.

6.1. Impulse Responses for Wideband Signals Centered at 900 MHz

Impulse responses for a wideband signal centered at 900 MHz (i.e., λ_c = 0.33 m) are given in Figures 14 - 19. Since low frequencies have the most influence, this is the worst scenario considered here. The eight geometries used in the frequency-domain analysis were maintained in order to isolate the near-surface and near-field effects. Given the large data set, a summary of basic observations is given to avoid unnecessary confusion:

1) Near the interface (i.e., $h \le 0.1$ m and $z \le 0.1$ m), the direct and reflected rays overlie each other if the time resolution of the pulse cannot resolve the rays.
2) The presence of a specific ray depends on the observed field component (e.g., if $h = z$, then the direct ray is below the noise floor in E_ρ for VED, H_ρ for HED-TE, and E_z and H_φ for HED-TM).
3) Individual rays may be affected by the antenna pattern, by transmission into the dielectric half plane, and by free-space loss (e.g., if $h = z$ and ρ is small, then the reflected ray from a VED is strongly attenuated by the source antenna pattern).

Near-surface effects are best observed at $h = z$ = 0.01 m in Figures 14, 16, and 18. The blue curve (i.e., GO + Norton term) isolates surface-wave effects. In the frequency domain, the surface wave causes a sharp increase in field strength concentrated at d.c.; in the time domain, this corresponds to a raised noise floor. Also, the surface wave has an $\exp(-jk_0R_1)$ phase dependence, arrives at the observation point along with the reflected ray, and enhances signal strength at that delay. The green curve (i.e., numerical evaluation of Sommerfeld integrals) demonstrates the more influential pseudo-lateral wave, which causes a delayed pulse near 37 ns. A simple calculation shows that a wave propagating 5 m through concrete at $(\varepsilon\mu_0)^{-½} \approx 1.34\times10^8$ m/s arrives at the observation point with a 37.4 ns delay.

As shown in Figures 15, 17, and 19, the reactive nature of the near field dominates for $\rho \le 0.1$ m. This is expected, as the separation is well within the carrier wavelength. When the direct ray is observed in the near field, GO error increases because the magnitude of the direct pulse and the noise floor rise. For this frequency band, the geometric optics approximation fails for $\rho \le 0.1$ m if the direct ray is significant.

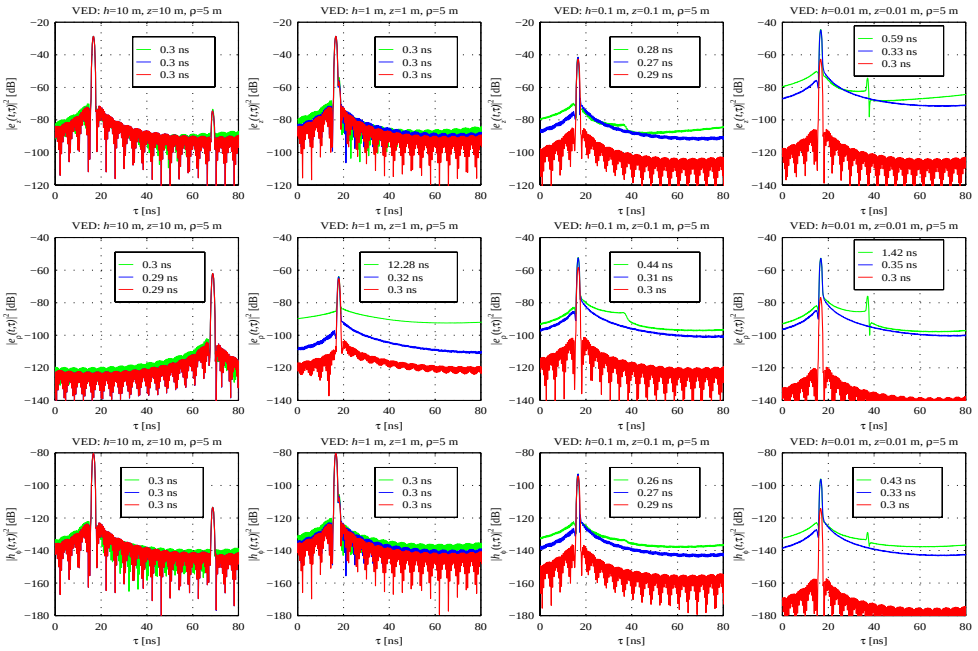

Figure 14. Near-surface effects on impulse responses of a VED above a concrete half space (f_c=900 MHz, BW≈660 MHz, threshold=-30 dB). Legends display Sommerfeld, GO + Norton term, and GO approximations to delay spread.

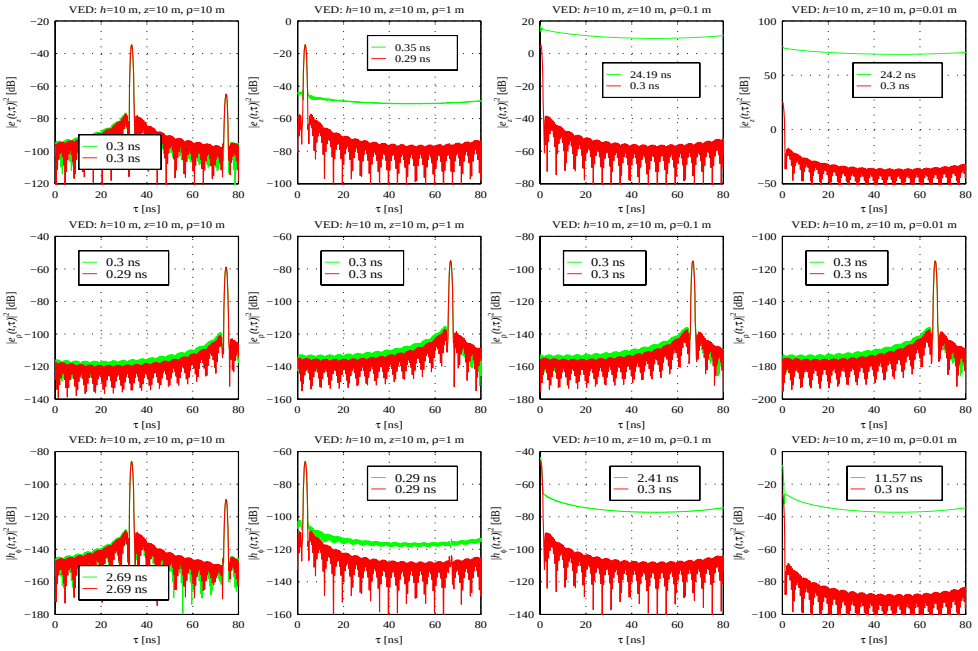

Figure 15. Near-field effects on impulse responses of a VED above a concrete half space (f_c=900 MHz, BW≈660 MHz, threshold=-30 dB). Legends display Sommerfeld and GO approximations to delay spread.

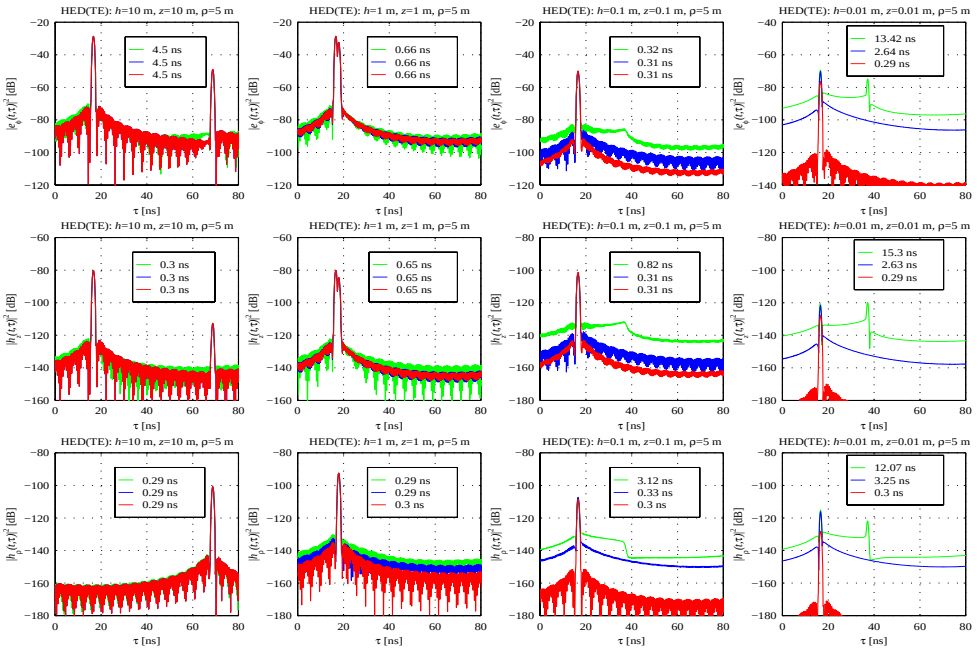

Figure 16. Near-surface effects on impulse responses of an x-aligned HED above a concrete half space (f_c=900 MHz, BW≈660 MHz, threshold=-30 dB, φ=90 °). Legends display Sommerfeld, GO + Norton term, and GO approximations to delay spread.

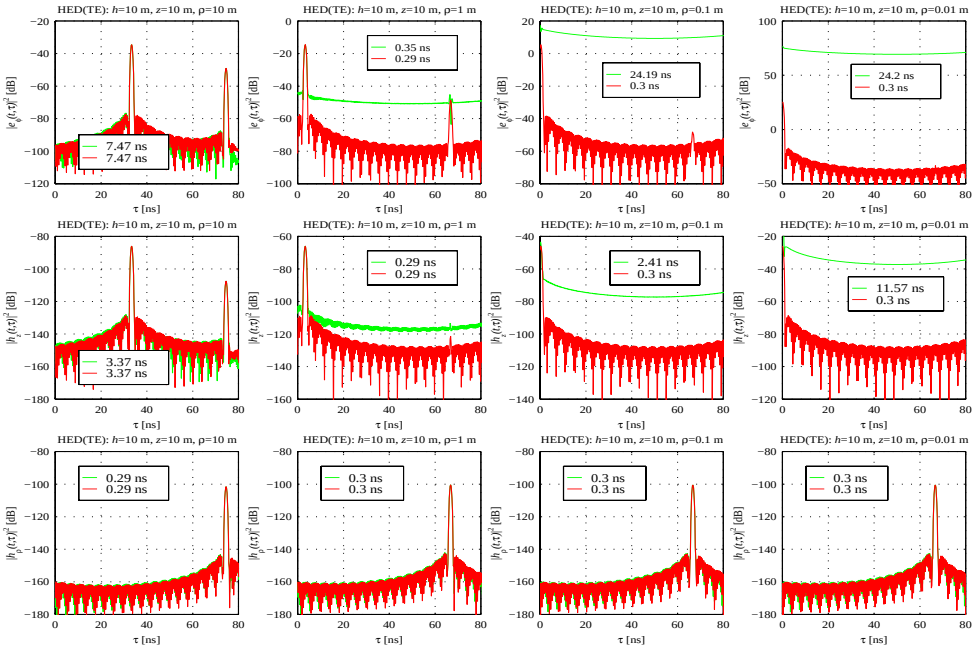

Figure 17. Near-field effects on impulse responses of an x-directed HED above a concrete half space (f_c=900 MHz, BW≈660 MHz, threshold=-30 dB, φ=90 °). Legends display Sommerfeld and GO approximations to delay spread.

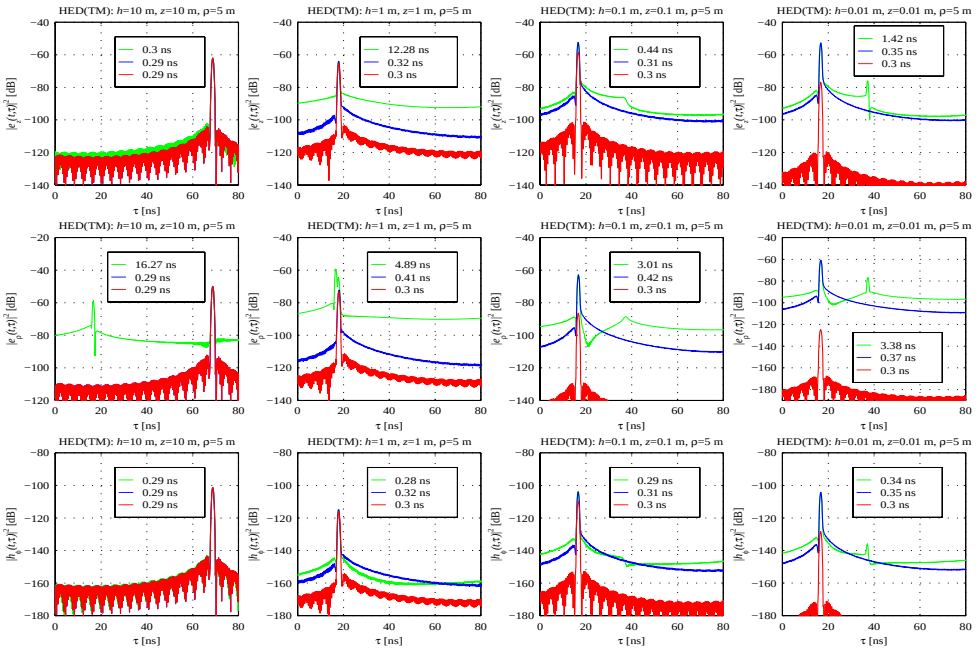

Figure 18. Near-surface effects on impulse responses of an x-aligned HED above a concrete half space (f_c=900 MHz, BW≈660 MHz, threshold=-30 dB, φ=0°). Legends display Sommerfeld, GO + Norton term, and GO approximations to delay spread.

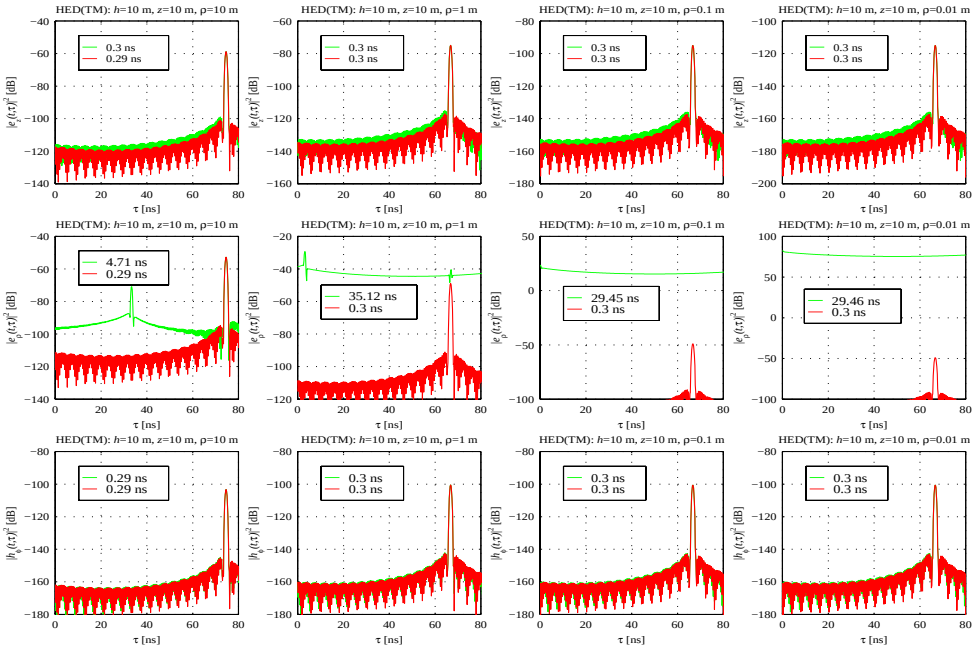

Figure 19. Near-field effects on impulse responses of an x-aligned HED above a concrete half space (f_c=900 MHz, BW≈660 MHz, threshold=-30 dB, φ=0°). Legends display Sommerfeld and GO approximations to delay spread.

Interesting observations are found in the HED-TM results in Figures 18 and 19, in which the observation points lie directly in the null of the x-aligned HED antenna pattern. As mentioned earlier, the transverse field components (i.e., e_z and h_φ) corresponding to the direct pulse are attenuated due to the orientation of the dipole. The radial component (i.e., e_ρ) corresponding to the direct ray, however, is influential due to near- and intermediate-field propagation.

Geometric optics predictions may be improved by including near-field terms when computing the direct-ray field components. When considering an x-aligned HED at $z = h$ and $\varphi = 0°$, the analytic expression for E_ρ corresponding to the direct ray is equivalent to E_r of equation (48) with $\theta_d = 0°$. For the geometry $\{(h\ [\text{m}], z\ [\text{m}], \rho\ [\text{m}])\} = \{(10, 10, 1)\}$, the direct ray was calculated via equation (48), the reflected ray was calculated via the second term of equation (22), and the magnitude of the individual rays along with the magnitude of their sum are displayed as a function of frequency in Figure 20. Notice that the near-field direct ray is comparable in magnitude to the reflected ray. The two rays destructively interfere, as shown in grey, which agrees with the Sommerfeld solution in Figure 11. The magnitude of the direct ray is frequency sensitive, as shown in the impulse responses in Figure 20. At f_c = 900 MHz, the spread of the impulse response is dominated by the high noise floor, which corresponds to the strong near fieldss near d.c. At higher frequencies the high noise floor is avoided, but the near-field direct ray produces high delay spreads as its magnitude approaches the magnitude of the reflected ray. Given the close confinement of most indoor channels, it seems logical to use the general expressions to account for near-field effects on the direct ray.

6.2. Impulse Responses for Wideband Signals Centered at 2.4 GHz and 5.8 GHz

Appendices B and C show impulse response results for carrier frequencies at 2.4 GHz and 5.8 GHz, respectively, at maximum bandwidth (i.e., BW = 1 GHz). The wider frequency range produces more narrow pulses in the time domain. As shown by the delay spreads, near-surface and near-field errors were reduced significantly at higher center frequencies because low frequencies had less influence. These errors, however, are not negligible. Appendix D provides delay spread curves as a function of bandwidth for center frequencies at 900 MHz, 2.4 GHz, and 5.8 GHz. These plots demonstrate that GO accuracy depends on frequency content and show cases where considerable GO error occurs for signals as high as 5.8 GHz.

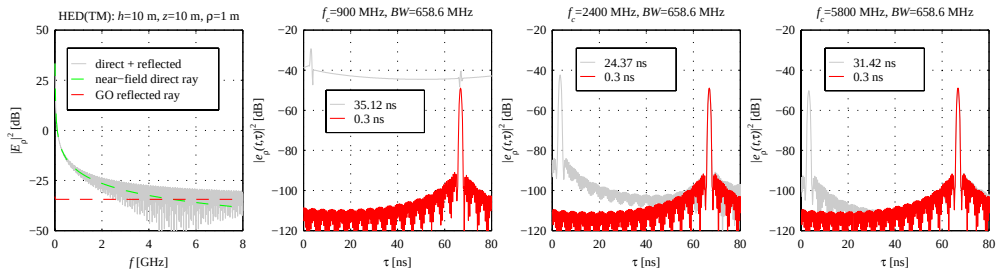

Figure 20. Combination of a near-field direct ray and far-field reflected ray for an x-aligned HED above a concrete half space (φ=0°).

6.3. Delay Spread Versus Bandwidth and Carrier Frequency

Thus far, we have demonstrated significant GO error in practical indoor scenarios and its dependence on material composition, geometry, and center frequency. This section helps to determine under what frequency conditions GO is valid.

Figures 21 - 26 are contour plots of delay spread (from the numerical evaluation of Sommerfeld integrals) versus bandwidth and carrier frequency. White areas indicate where negative frequencies would be encountered. Figures 27 - 32 are contour plots of percentage error (associated with the GO approximation) versus bandwidth and carrier frequency. Percentage error is formulated as

$$\% \text{ error } \tau_{spr}^{v} = 100 \frac{|\tau_{spr}^{S,v} - \tau_{spr}^{GO,v}|}{\tau_{spr}^{S,v}} , \quad (51)$$

where *v* stands for the relative field component. From these plots we draw the following conclusions based on delay spread results of elementary electric dipoles above a concrete half space for typical indoor dimensions and frequencies:

1) Surface-wave effects are significant for heights on the order of 0.1m or less at BW > 0.6 f_c for TM fields radiated by VED and HED sources.
2) Pseudo-lateral-wave effects are significant for heights on the order of 0.01 m or less at f_c < 1.8 GHz for E_ρ fields radiated by a VED source, f_c < 3.8 GHz for TE fields radiated by a HED source, f_c < 1.8 GHz for E_z fields radiated by a HED source, and f_c < 2.5 GHz for E_ρ fields radiated by a HED source.
3) Near-field effects are significant for separation on the order of 0.1 m or less at $BW > 0.6 f_c$ for transverse fields radiated by VED and HED sources.
4) Near-field effects are significant for radial fields observed in the null of the antenna patterns of VED and HED sources.

7. CONCLUSION

In this report, we evaluated the error associated with GO predictions for indoor propagation models. Our conclusions were based on results from the classical problem of elementary dipoles above a lossy half space. Exact (i.e., Sommerfeld) and approximate (i.e., GO and GO + Norton surface-wave term) formulations for vertical and horizontal dipole sources were summarized, and numerical schemes for evaluating the complex integrals in the Sommerfeld formulation were given. Eight canonical geometries were chosen to isolate individual propagation effects on relevant field components. Most scenarios were limited to material properties appropriate for concrete and physical dimensions up to 10 m and as small as 1 cm. Results were given in both the frequency and time domains.

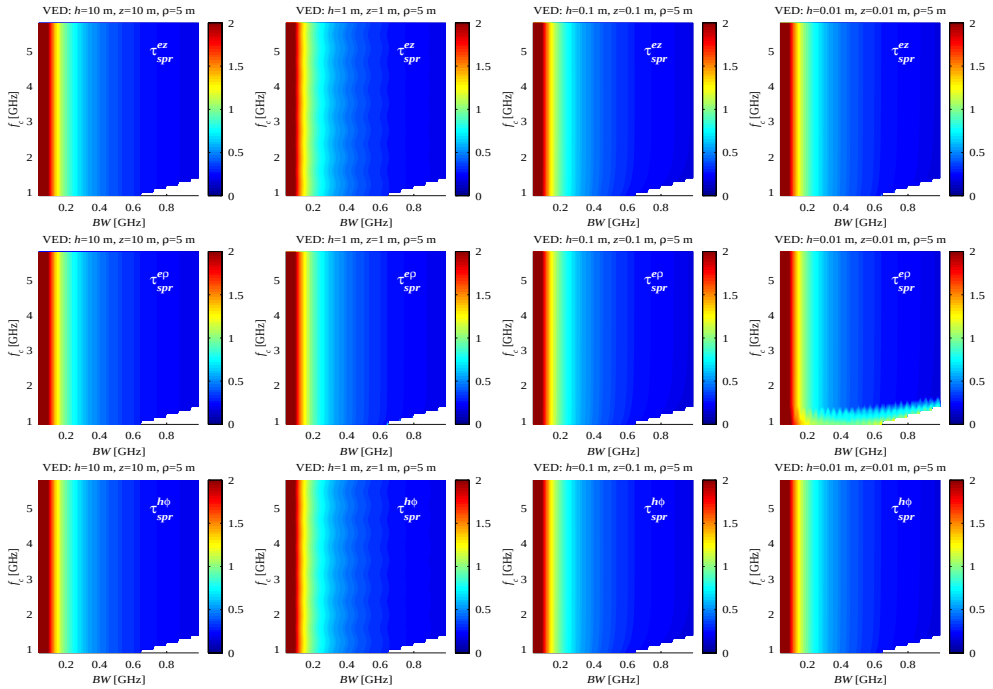

Figure 21. Near-surface effects on delay spread versus *BW* and center frequency for a VED above a concrete half space (Hamming window, threshold=-30 dB).

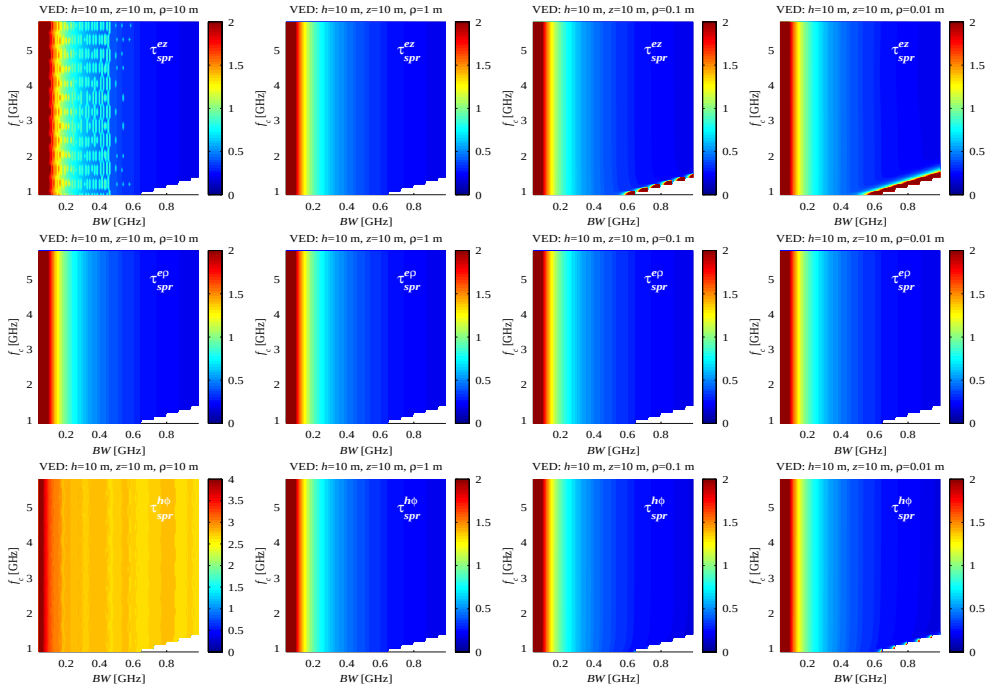

Figure 22. Near-field effects on delay spread versus *BW* and center frequency for a VED above a concrete half space (Hamming window, threshold=-30 dB).

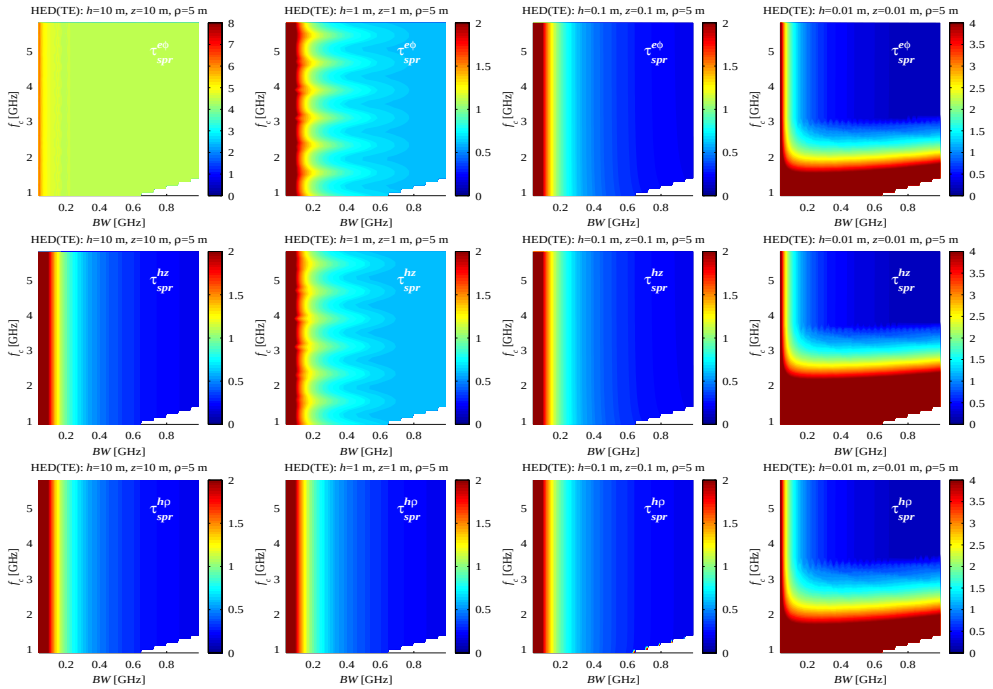

Figure 23. Near-surface effects on delay spread versus *BW* and center frequency for a HED above a concrete half space (Hamming window, threshold=-30 dB, *φ*=90°).

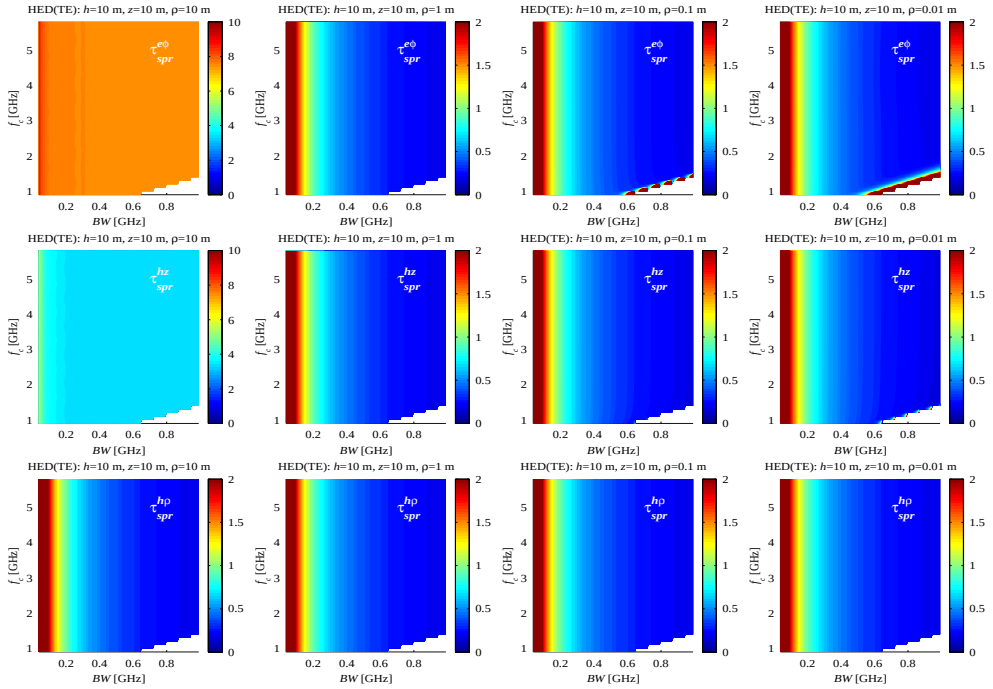

Figure 24. Near-field effects on delay spread versus *BW* and center frequency for a HED above a concrete half space (Hamming window, threshold=-30 dB, *φ*=90°).

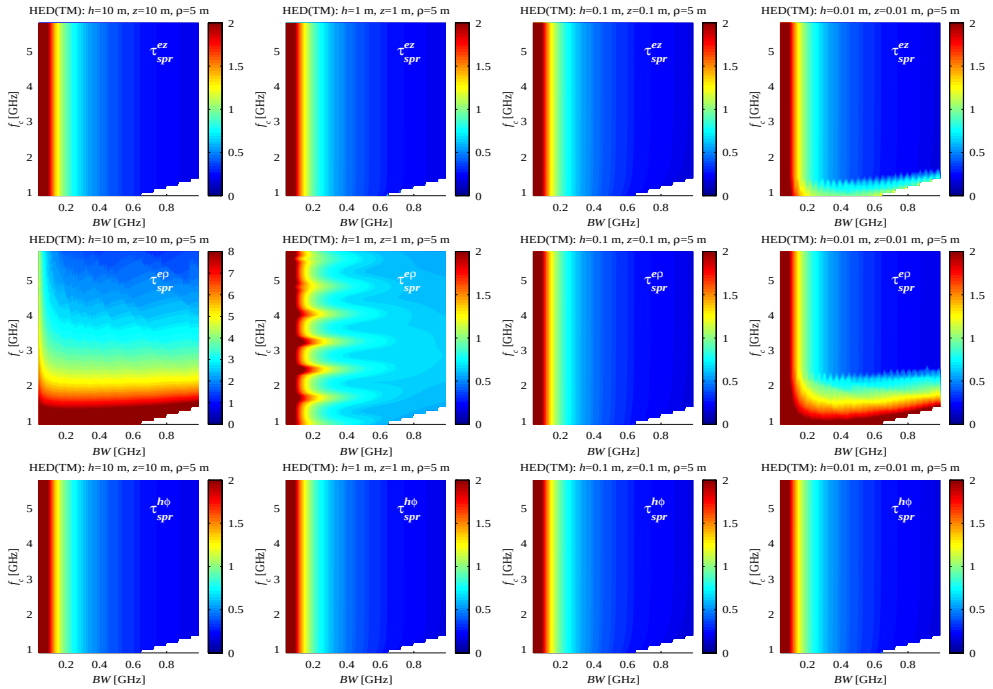

Figure 25. Near-surface effects on delay spread versus *BW* and center frequency for a HED above a concrete half space (Hamming window, threshold=-30 dB, φ=0°).

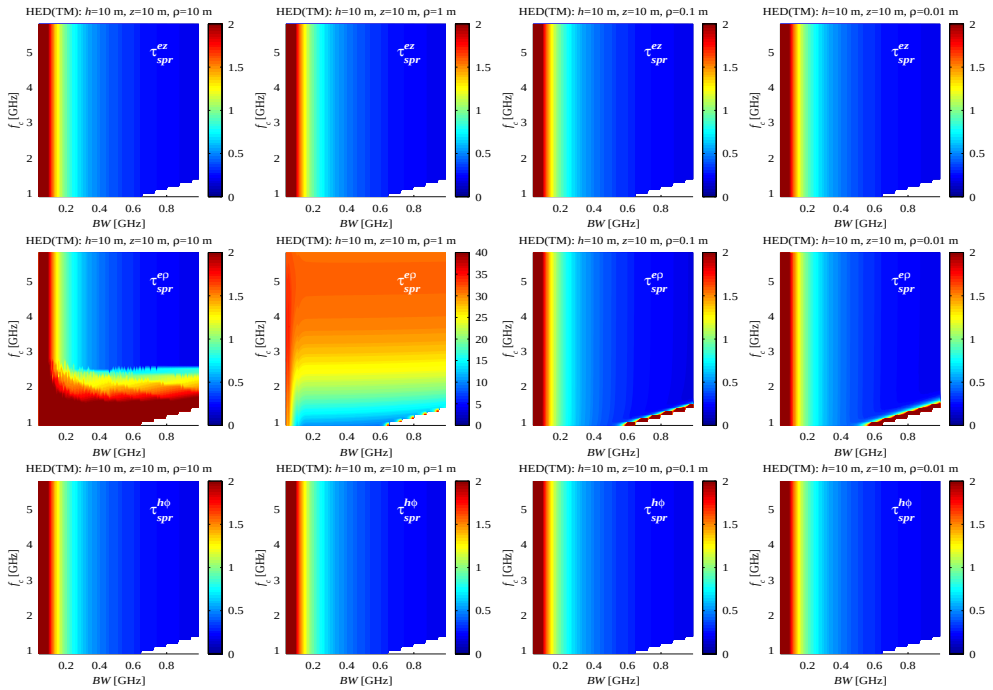

Figure 26. Near-field effects on delay spread versus *BW* and center frequency for a HED above a concrete half space (Hamming window, threshold=-30 dB, φ=0°).

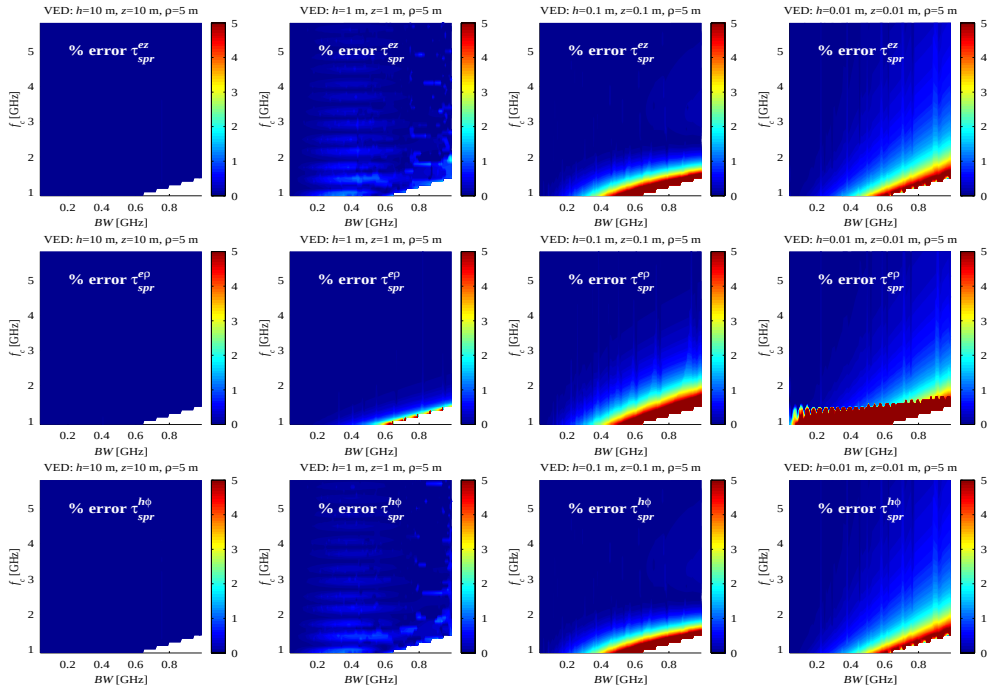

Figure 27. Near-surface effects on % error delay spread versus *BW* and center frequency for a VED above a concrete half space (Hamming window, threshold=-30 dB).

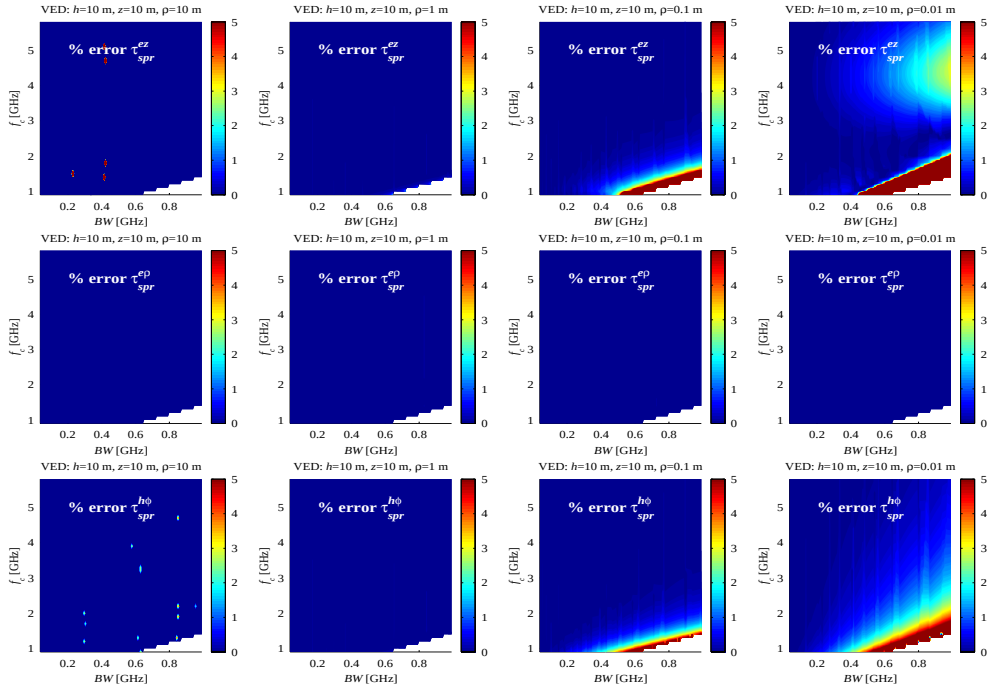

Figure 28. Near-field effects on % error delay spread versus *BW* and center frequency for a VED above a concrete half space (Hamming window, threshold=-30 dB).

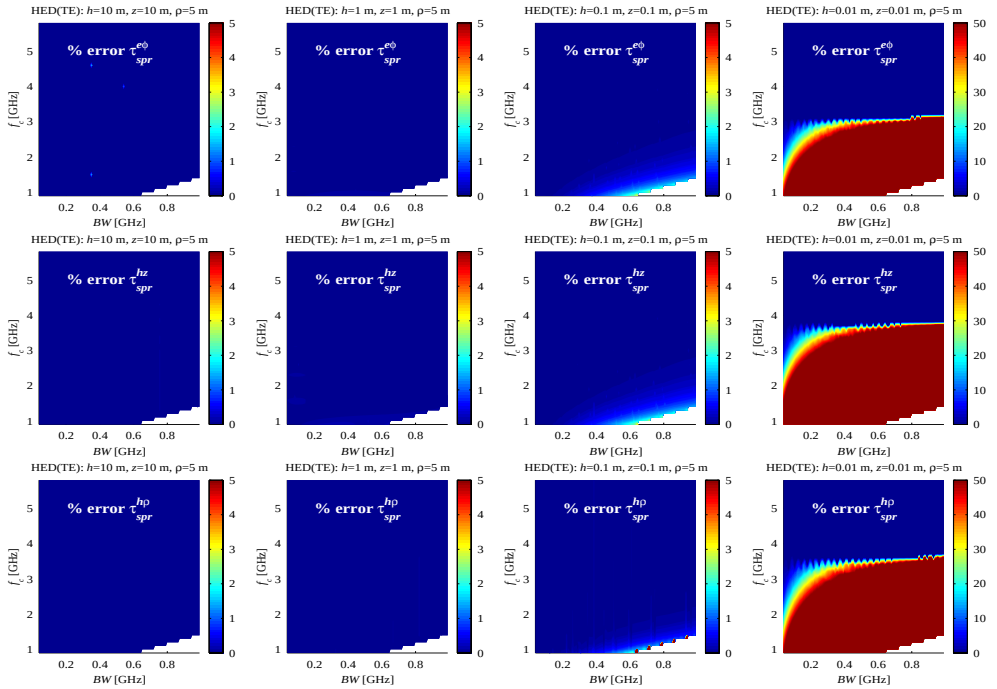

Figure 29. Near-surface effects on % error delay spread versus *BW* and center frequency for a HED above a concrete half space (Hamming window, threshold=-30 dB, φ=90°).

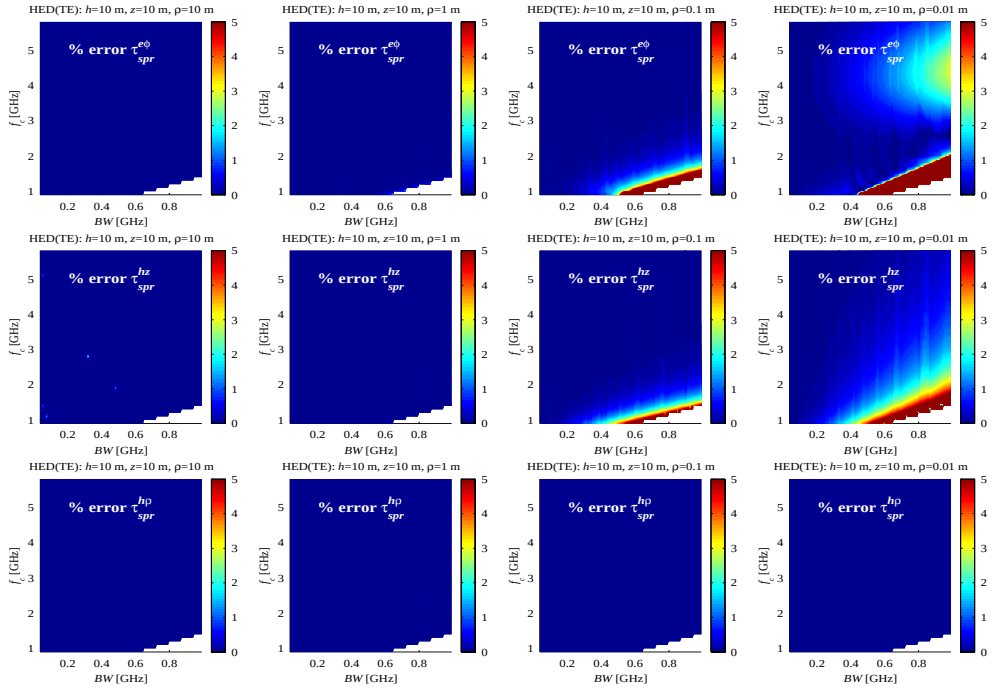

Figure 30. Near-field effects on % error delay spread versus *BW* and center frequency for a HED above a concrete half space (Hamming window, threshold=-30 dB, φ=90°).

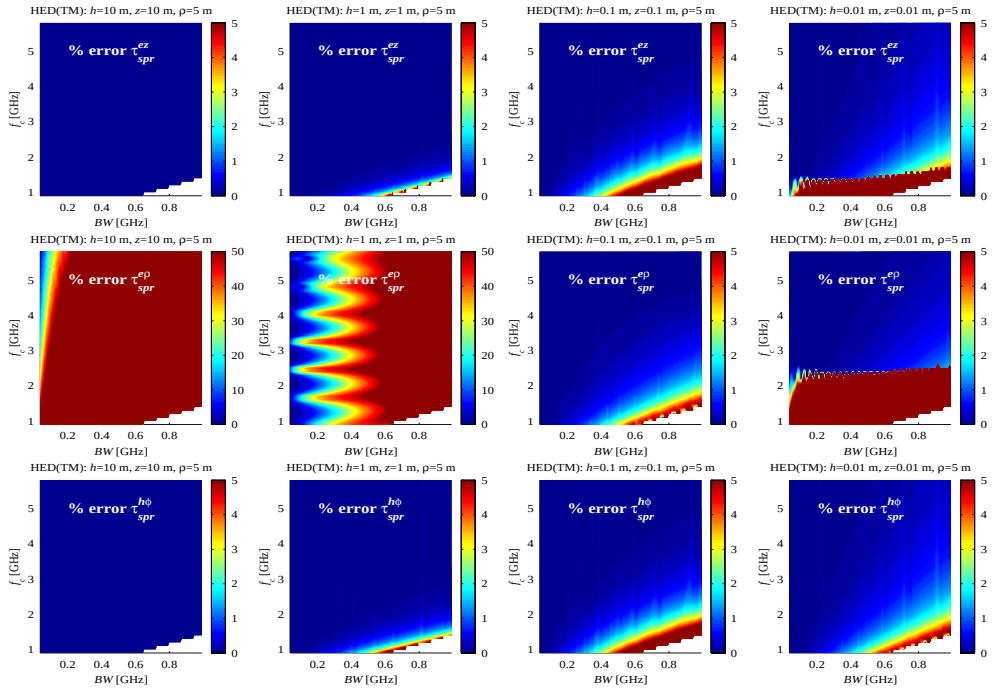

Figure 31. Near-surface effects on % error delay spread versus *BW* and center frequency for a HED above a concrete half space (Hamming window, threshold=-30 dB, φ=0°).

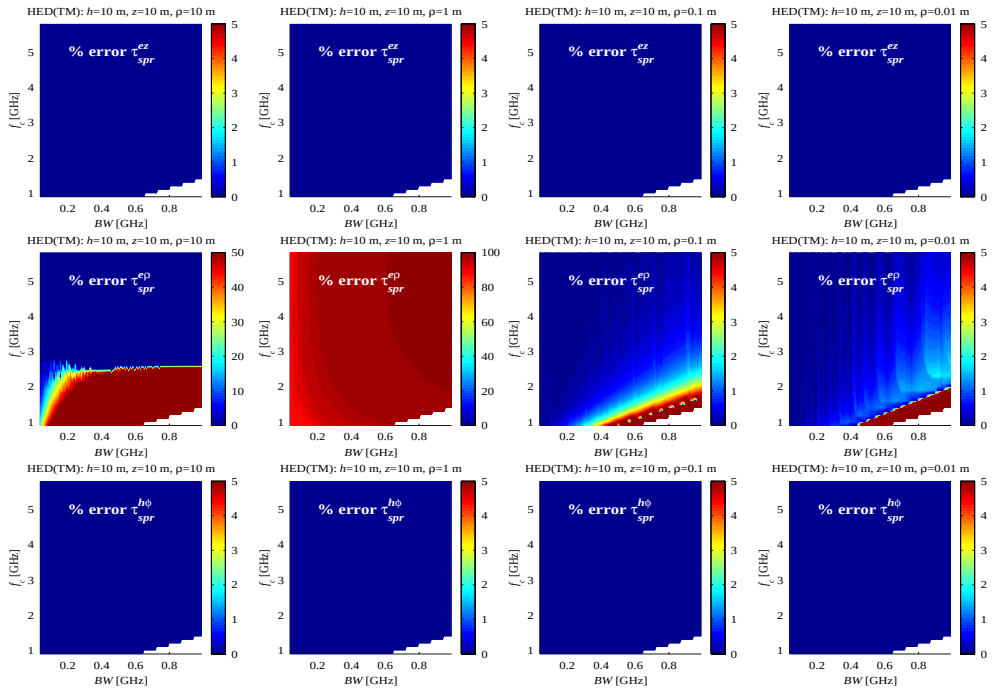

Figure 32. Near-field effects on % error delay spread versus *BW* and center frequency for a HED above a concrete half space (Hamming window, threshold=-30 dB, φ=0°).

As expected, GO predictions agreed with the numerical approximations to Sommerfeld integrals when the source and observation points were multiple wavelengths above the surface and multiple wavelengths apart. By drawing the points close to the surface and close together, we were able to isolate classic surface-wave and near-field effects and observe an additional propagation mechanism we call the pseudo-lateral wave. Frequency-domain observations are summarized as follows:

Surface-wave observations in the frequency domain

1) Surface-wave effects peak at d.c. and decrease sharply with increasing frequency.
2) Surface-wave propagation is more influential in TM fields than in TE fields.

Pseudo-lateral-wave observations in the frequency domain

3) Pseudo-lateral-wave effects are influential over a broad range of frequencies.
4) Pseudo-lateral-wave propagation is more influential in TE fields than in TM fields.

Near-field observations in the frequency domain

5) Near-field effects peak at d.c. and decrease sharply with increasing frequency.
6) Near-field error depends on the individual propagation paths and field components.
7) Near-field effects are significant for radial fields observed in the null of the dipole antenna pattern at observation points many wavelengths away.

These observations demonstrated frequency dependency and interesting electromagnetic behavior, but they were fairly inconclusive; hence, we transformed the results to the time domain in order to assess the practical significance of the propagation mechanisms.

Frequency domain results were translated into band-limited impulse responses. The frequency content was specified by center frequency and bandwidth, and time dispersion was quantified via delay spread. Time-domain observations are summarized as follows:

Surface-wave observations in the time domain

1) Surface waves create a pulse at the reflected-ray delay and increase the noise floor.
2) Surface-wave effects are significant for heights on the order of 0.1 m or less at BW > 0.6 f_c for TM fields radiated by VED and HED sources.

Pseudo-lateral-wave observations in the time domain

3) Pseudo-lateral-wave pulses are delayed according to the electric properties of the dielectric.
4) Pseudo-lateral-wave effects are significant for heights on the order of 0.01 m or less at
   a) f_c < 1.8 GHz for E_ρ fields radiated by a VED source,
   b) f_c < 3.8 GHz for TE fields radiated by a HED source,
   c) f_c < 1.8 GHz for E_z fields radiated by a HED source, and
   d) f_c < 2.5 GHz for E_ρ fields radiated by a HED source.

Near-field observations in the time domain

5) Near-field effects increase the noise floor.
6) Near-field effects are significant for separation on the order of 0.1 m or less at $BW > 0.6\, f_c$ for transverse fields radiated by VED and HED sources.
7) Near-field effects can be predominant for radial fields observed in the null of the antenna patterns of VED and HED sources.

Conditions which cause the GO approximation to be invalid depend on the transmit and receive antennas and their position, on the material composition of the reflecting surface, and on the operational frequency band. General expressions for incremental electric dipoles above a half space have been provided to improve the accuracy of GO predictions by accounting for surface-wave and near-field effects. More specifically, the GO approximation may be complemented by the Norton surface-wave terms in equations (18), (21), and (22) when $k_0 R_0 \gg 1$ and $|k_1| > |k_0|$ and by the near-field terms in equation (48) to model the direct ray. These expressions, however, apply only to elementary dipoles above a dielectric half space. Care should be taken when modeling actual antennas and finite-thick reflection surfaces.

As demonstrated, pseudo-lateral wave effects can be severe. The leading terms of equations (43) and (46) show evidence of the pseudo-lateral wave; these equations, however, are cumbersome and require numerous derivatives and substitutions in order to acquire field equations. A more mathematically rigorous derivation is necessary in order to provide a closed-form asymptotic approximation to the pseudo-lateral wave.

8. ACKNOWLEDGMENTS

The authors thank Dr. George A. Hufford, J. Randy Hoffman, Paul McKenna, and Robert J. Achatz for insights shared.

9. REFERENCES

[1] K. Pahlavan and A.H. Levesque, *Wireless Information Networks*, New York: John Wiley & Sons, 1995, pp. 37-206.

[2] T.S. Rappaport, *Wireless Communications: Principles and Practice*, Upper Saddle River, NJ: Prentice Hall PTR, 1996, pp. 139-196.

[3] J.C.I. Chuang, "The effects of time delay spread on portable radio communication channels with digital modulation," *IEEE J. Selected Areas Commun.*, vol. 5, no. 5, pp. 879-889, Jun. 1987.

[4] P.A. Bello and B.D. Nelin, "The effect of frequency selective fading on the binary error probabilities of incoherent and differentially coherent matched filter receivers," *IEEE Trans. Commun. Systems*, vol. 11, no. 2, pp. 170-186, Jun. 1963.

[5] M. Wittmann, J. Marti, and T. Kurner, "Impact of the power delay profile shape on the bit error rate in mobile radio systems," *IEEE Trans. Veh. Technol.*, vol. 46, no. 2, pp. 329-339, May 1997.

[6] D.M.J. Devasirvatham, "Multipath time delay spread in the digital portable radio environment," *IEEE Commun. Mag.*, vol. 25, no. 6, pp. 13-21, Jun. 1987.

[7] L.J. Greenstein and V.K. Prabhu, "Analysis of multipath outage with applications to 90-Mbits/s PSK systems at 6 and 11 GHz," *IEEE Trans. Commun.*, vol. 27, no. 1, pp. 68-75, Jan. 1979.

[8] A.G. Burr, "Modulation and multipath countermeasures," in *Modern Personal Radio Systems*, R.C.V. Macario, Ed., London: Institution of Electrical Engineers, 1996, pp. 43-78.

[9] C.A. Siller, Jr.,"Multipath propagation," *IEEE Commun. Mag.*, vol. 22, no. 2, pp. 6-15, Feb. 1984.

[10] W.C. Jakes, "An approximate method to estimate an upper bound on the effect of multipath delay distortion on digital transmission," *IEEE Trans. Commun.*, vol. 27, no. 1, pp. 76-81, Jan. 1979.

[11] M.C. Lawton and J.P. McGeehan, "The application of GTD and ray launching to channel modeling for cordless radio systems," in *Proc. IEEE Veh. Technol. Conf.*, Denver, CO, May 1992, pp. 125-130.

[12] K.R. Schauback, N.J. Davis, and T.S. Rappaport, "A ray tracing method for predicting path loss and delay in microcellular environments," in *Proc. IEEE Veh. Technol. Conf.*, Denver,

CO, May 1992, pp. 932-935.

[13] S.Y. Seidel and T.S. Rappaport, "A ray tracing technique to predict path loss and delay spread inside buildings," in *Proc. IEEE GLOBECOM 92*, Orlando, FL, Dec. 1992, pp. 649-653.

[14] T. Holt, K. Pahlavan, and J.F. Lee, "A graphical indoor radio channel simulator using ray tracing," in *Proc. IEEE PIMRC '92*, Boston, MA, Oct. 1992, pp. 411-416.

[15] W. Honcharenko, H.L. Bertoni, J.L. Dailing, J. Qian, and H.D. Yee, "Mechanisms governing UHF propagation on single floors in modern office buildings," *IEEE Trans. Veh. Technol.*, vol. 41, no. 4, pp. 496-504, Nov. 1992.

[16] G. Yang, K. Pahlavan, and J.F. Lee, "A 3D propagation model with polarization characteristics in indoor radio channels," in *Proc. IEEE GLOBECOM '93*, Houston, TX, Nov. 1993, pp. 1252-1256.

[17] G. Bronson, K. Pahlavan, and H. Rotithor, "Performance prediction of wireless LANs based on ray tracing algorithms," in *Proc. PIMRC 93*, Yokohama, Japan, Oct. 1993, pp. 151-156.

[18] R.A. Valenzuela, "A ray tracing approach to predicting indoor wireless transmission," in *Proc. IEEE Veh. Technol. Conf.*, Secaucus, NJ, May 1993, pp. 214-218.

[19] M.C. Lawton and J.P. McGeehan, "The application of a deterministic ray launching algorithm for the prediction of radio channel characteristics in small-cell environments," *IEEE Trans. Veh. Technol.*, vol. 43, no. 4, pp. 955-968, Nov. 1994.

[20] S.Y. Seidel and T.S. Rappaport, "Site-specific propagation prediction for wireless in-building personal communication system design," *IEEE Trans. Veh. Technol.*, vol. 43, no. 4, pp. 879-891, Nov. 1994.

[21] T. Kürner, D.J. Cichon, and W. Wiesbeck, "Evaluation and verification of the VHF/UHF propagation channel based on a 3-D-wave propagation model," *IEEE Trans. on Antennas and Propagat.*, vol. 43, no. 4, pp. 879-891, Nov. 1994.

[22] G. Durgin, N. Patwari, and T.S. Rappaport, "Improved 3D ray launching method for wireless propagation prediction," *Electronic Letters*, vol. 33, no. 16, pp. 1412-1413, Jul. 1997.

[23] S.H. Chen and S.K. Jeng, "An SBR/Image approach to indoor radio wave propagation in indoor environments with metallic furniture," *IEEE Trans. on Antennas and Propagat.*, vol. 45, no. 1, pp. 98-106, Jan. 1997.

[24] R.P. Torres, L. Valle, M. Domingo, S. Loredo, and M.C. Diez, "Cindoor: An engineering tool for planning and design of wireless systems in enclosed spaces," *IEEE Antennas and*

Propagat. Mag., vol. 41, no. 4, pp. 11-22, Aug. 1999.

[25] A.A.M. Saleh and R.A. Valenzuela, "A statistical model for indoor multipath propagation," *IEEE J. Selected Areas Commun.*, vol. 5, no. 2, pp. 128-137, Feb. 1987.

[26] D. Molkdar, "Review on radio propagation into and within buildings," *IEE Proc.-H: Microwave, Antennas and Propagat.*, vol. 138, no. 1, pp. 61-73, Feb. 1991.

[27] R. Ganesh and K. Pahlavan, "Statistical modelling and computer simulation of indoor radio channel," *IEE Proc.-I: Commun. Speech and Vision*, vol. 138, no. 3, pp. 153-161, Jun. 1991.

[28] T.S. Rappaport, S.Y. Seidel, and K. Takamizawa, "Statistical channel impulse response models for factory and open plan building radio communication system design," *IEEE Trans. Commun.*, vol. 39, no. 5, pp. 794-807, May 1991.

[29] P. Yegani and C.D. McGillem, "A statistical model for the factory radio channel," *IEEE Trans. Commun.*, vol. 39, no. 10, pp. 1445-1454, Oct. 1991.

[30] T.S. Rappaport and D.A. Hawbaker, "Wide-band microwave propagation parameters using circular and linear polarized antennas for indoor wireless channels," *IEEE Trans. Commun.*, vol. 40, no. 2, pp. 240-245, Feb. 1992.

[31] G.A. Hufford, "A characterization of the multipath in the HDTV channel," *IEEE Trans. on Broadcasting*, vol. 38, no. 4, pp. 252-254, Dec. 1992.

[32] S.J. Howard and K. Pahlavan, "Autoregressive modeling of wide-band indoor radio propagation," *IEEE Trans. Commun.*, vol. 40, no. 9, pp. 1540-1552, Sep. 1992.

[33] H. Hashemi, "Impulse response modeling of indoor radio propagation channels," *IEEE J. Selected Areas Commun.*, vol. 11, no. 7, pp. 967-978, Sep. 1993.

[34] C.L. Holloway, M.G. Cotton, and P. McKenna, "A simplified model for calculating the decay rate of the impulse response for an indoor propagation channel," in *Proc. Wireless Communic. Conf.*, Boulder, CO., Aug. 1997, pp. 210-214.

[35] C.L. Holloway, M.G. Cotton, and P. McKenna, "A model for predicting the power delay profile characteristics inside a room," *IEEE Trans. Veh. Technol.*, vol. 48, no. 4, pp. 1110-1120, Jul. 1999.

[36] L. Talbi and G.Y. Delisle, "Finite difference time domain characterization of indoor radio propagation," in *Electromagnetic Waves Pier 12, Progress in Electromagnetic Research*, J. A. Kong, Ed., Cambridge, Massachusetts: EMW Publishing, 1996, pp. 251-275.

[37] A. Lauer, I. Wolff, A. Bahr, J. Pamp, J. Kunisch, and I. Wolff, "Multi-mode FDTD simulations of indoor propagation including antenna properties," in *Proc. IEEE Veh. Technol. Conf.*, Chicago, IL, Jul. 1995, pp. 454-458.

[38] A. Taflove, *Computational Electrodynamics: The Finite-Difference Time-Domain Method*, Boston: Artech House, 1995.

[39] K.S. Kunz and R. J. Luebbers, *The Finite Difference Time Domain Method for Electromagnetics*, Boca Raton: CRC Press, 1993.

[40] A. Sommerfeld, *Partial Differential Equations in Physics*, New York: Academic Press, 1964.

[41] A. Baños, *Dipole Radiation in the Presence of a Conducting Half-Space*, New York: Pergamon Press, 1966.

[42] K.A. Norton, "The propagation of radio waves over the surface of the earth and in the upper atmosphere," *Proc. of the IRE*, vol. 25, no. 9, pp. 1203-1236, Sep. 1937.

[43] G. Tyras, *Radiation and Propagation of Electromagnetic Waves*, New York: Academic Press, 1969.

[44] T.S.M. Maclean and Z. Wu, *Radiowave Propagation Over Ground*, New York: Chapman & Hall, 1993, pp. 1-119.

[45] B. van der Pol, "Theory of the reflection of the light from a point source by a finitely conducting flat mirror, with an application to radiotelegraphy," *Physica*, vol. 2, pp. 843-853, 1935.

[46] J.R. Wait, "The ancient and modern history of EM ground-wave propagation," *IEEE Antennas and Propagat. Mag.*, vol. 40, no. 5, pp. 7-24, Oct. 1998.

[47] C. Johnk, *Engineering Electromagnetic Fields and Waves*, New York: John Wiley & Sons, Inc., 1988.

[48] W.H Press, B.P. Flannery, S.A. Teukolsky, and W.T. Vetterling, "Integration of functions," in *Numerical Recipes*, New York: Cambridge University Press, 1986, pp. 102-130.

[49] J.R. Mosig, "Integral equation technique," in *Numerical Techniques for Microwave and Millimeter-Wave Passive Structures*, T. Itoh, Ed., New York: Wiley, 1989, pp. 133-213.

[50] R.J. Lytle and D.L. Lager, "Numerical evaluation of Sommerfeld integrals," Lawrence Livermore Laboratory Report W-7405-Eng-48, Oct. 1974.

[51] W.A. Johnson and D.G. Dudley, "Real axis integration of Sommerfeld integrals: Source and observation points in air," *Radio Science*, vol. 18, no. 2, pp. 175-186, Mar. 1983.

[52] K.A. Michalski, "Extrapolation methods for Sommerfeld integral tails," *IEEE Trans. Antennas Propagat.*, vol. 46, pp. 1405-1418, Oct. 1998.

[53] R.O. LaMaire, A. Krishna, P. Bhagwat, and J. Panian, "Wireless LANs and mobile networking standards and future directions," *IEEE Commun. Mag.*, vol. 34, no. 8, pp. 86-94, Aug. 1996.

[54] U.B. Halabe, A. Sotoodehnia, K.R. Maser, and E.A. Kausel, "Modeling the electromagnetic properties of concrete," *ACI Materials Journal*, vol. 90, no. 6, pp. 552-563, Nov. 1993.

[55] E.F. Kuester and D.C. Chang, "Evaluation of Sommerfeld integrals associated with dipole sources above earth," University of Colorado Scientific Report No. 43, Jan. 1979.

[56] R.W. King, M. Owens, and T.T. Wu, "Properties of lateral electromagnetic fields and their application," *Radio Science*, vol. 21, no. 1, pp. 13-23, Jan. 1986.

[57] L.W. Li, T.S. Yeo, P.S. Kooi, and M.S. Leong, "Radio wave propagation along mixed paths through a four-layered model of rain forest: An analytic approach," *IEEE Trans. on Antennas and Propagat.*, vol. 46, no. 7, pp. 1098-1111, Jul. 1998.

[58] E. Bedrosian, "The analytic signal representation of modulated waveforms," *Proc. of the IRE*, vol. 50, pp. 2071-2076, Oct. 1962.

[59] D. Vakman, *Signals, Oscillations, and Waves: A Modern Approach*, Boston: Artech House, 1998.

[60] M.G. Cotton, R.J. Achatz, Y. Lo, and C.L. Holloway, "Indoor polarization and directivity measurements at 5.8 GHz," NTIA Report 00-372, Nov. 1999.

This Page Intentionally Left Blank

This Page Intentionally Left Blank

APPENDIX A: FIELD STRENGTH VERSUS FREQUENCY AND SEPARATION

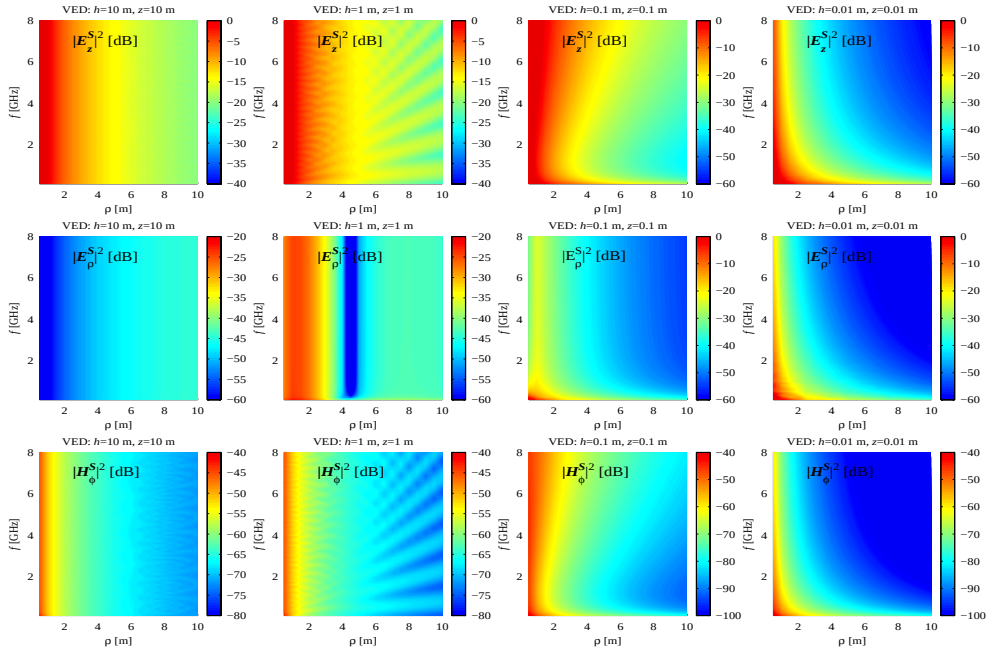

Figure A-1. Sommerfeld field strength of a VED above a concrete half space (h=z) versus frequency and horizontal separation.

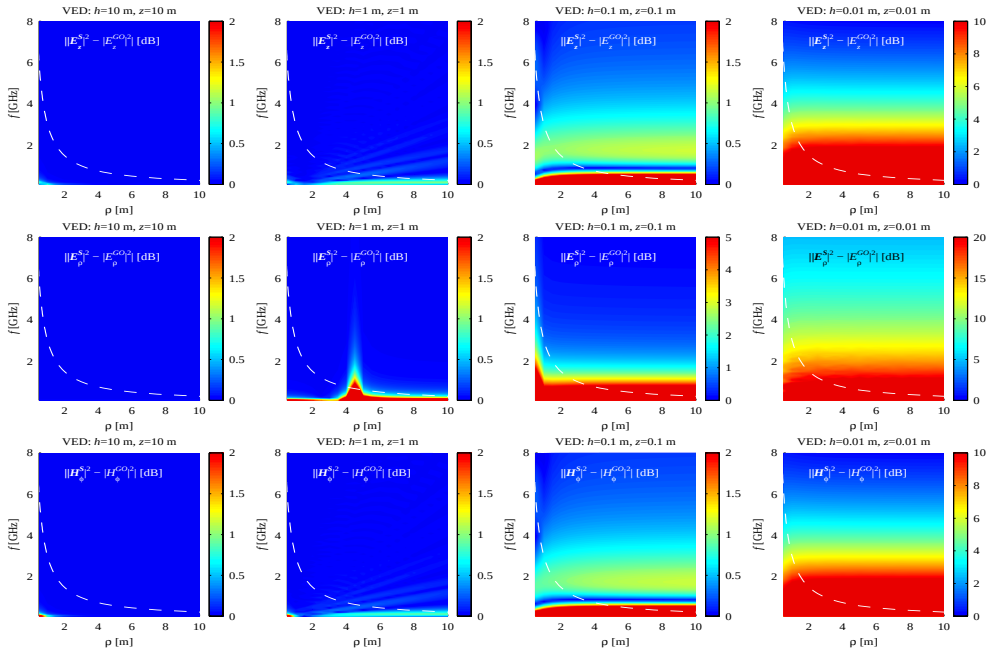

Figure A-2. Field strength residual error of a VED above a concrete half space (h=z) versus frequency and horizontal separation.

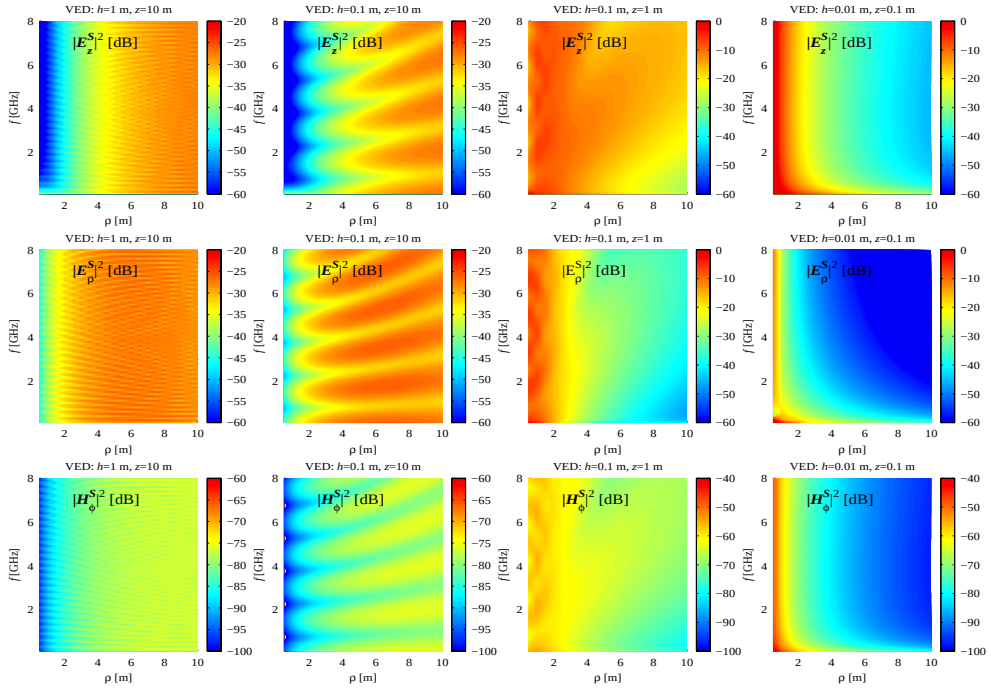

Figure A-3. Sommerfeld field strength of a VED above a concrete half space ($h \neq z$) versus frequency and horizontal separation.

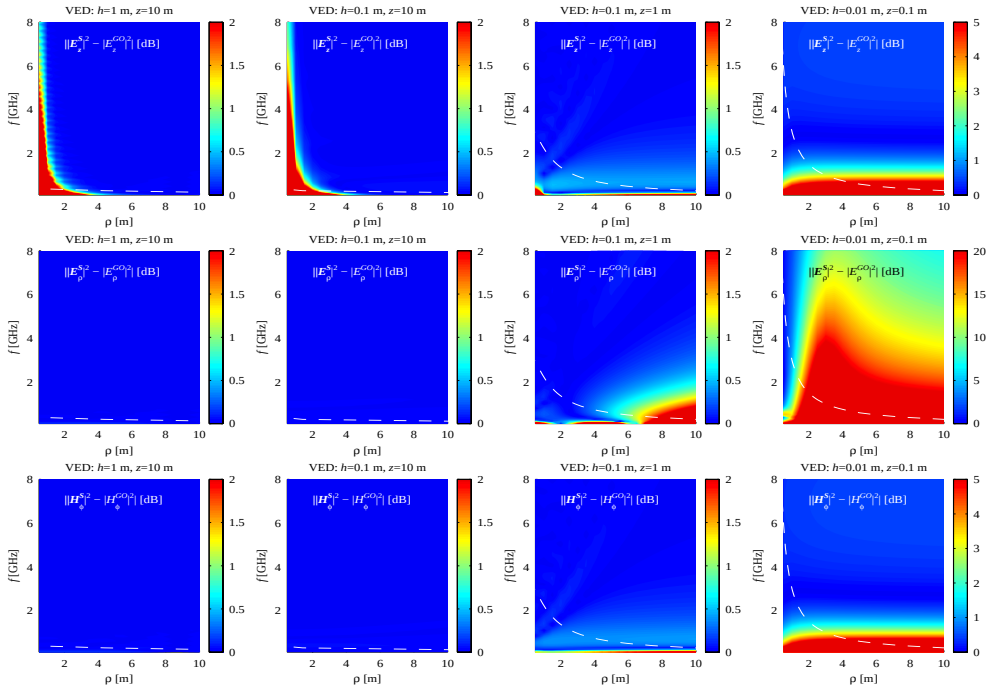

Figure A-4. Field strength residual error of a VED above a concrete half space ($h \neq z$) versus frequency and horizontal separation.

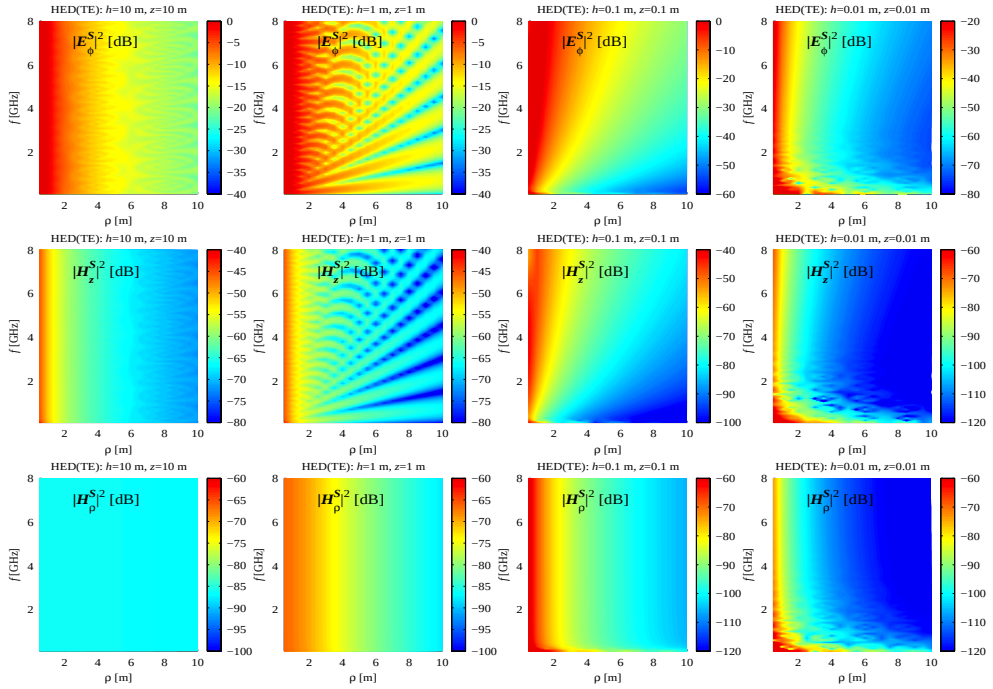

Figure A-5. Sommerfeld field strength of a HED above a concrete half space (h=z, φ=90°) versus frequency and horizontal separation.

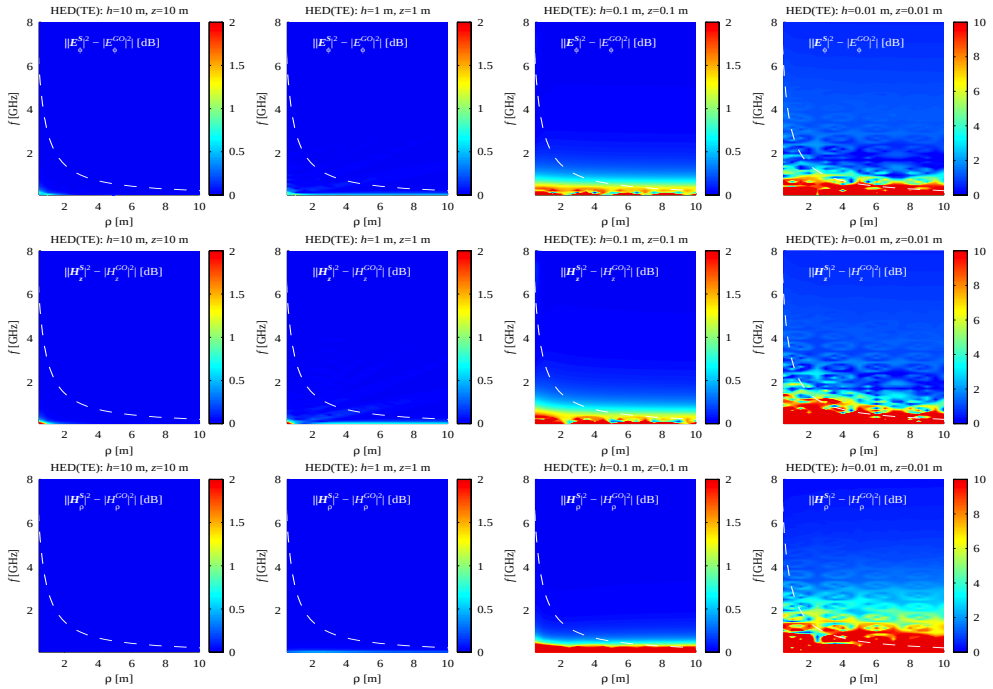

Figure A-6. Field strength residual error of a HED above a concrete half space (h=z, φ=90°) versus frequency and horizontal separation.

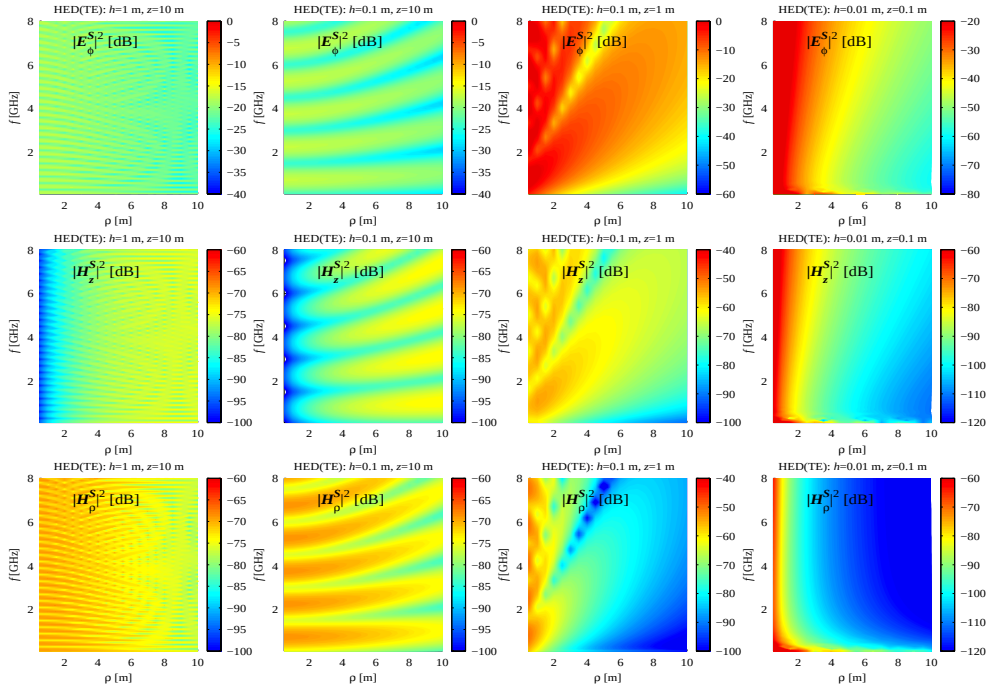

Figure A-7. Sommerfeld field strength of a HED above a concrete half space ($h \neq z$, φ=90°) versus frequency and horizontal separation.

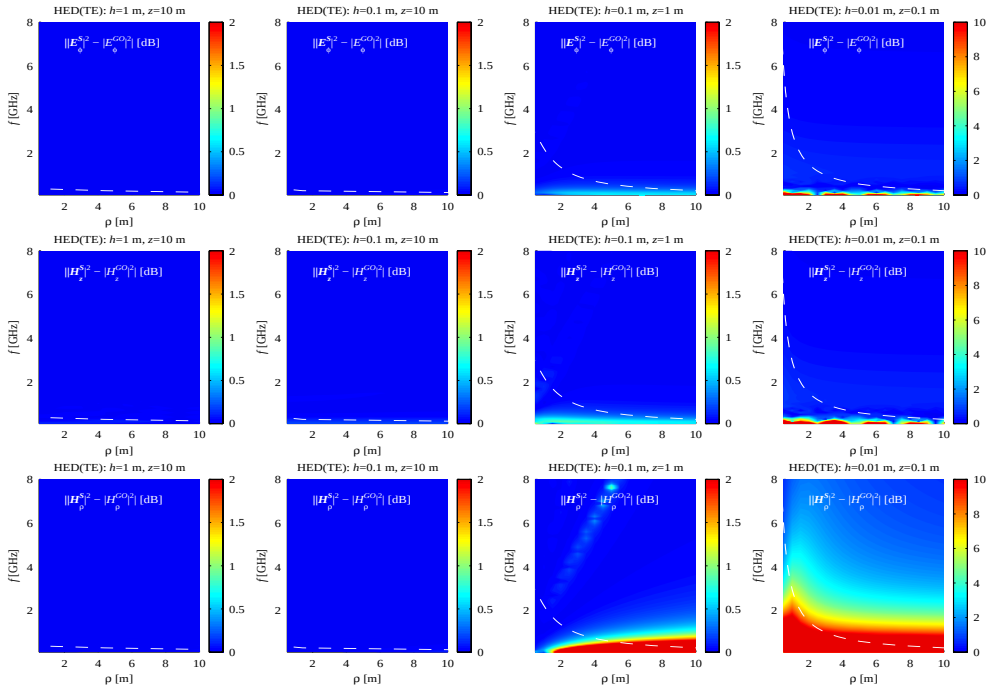

Figure A-8. Field strength residual error of a HED above a concrete half space ($h \neq z$, φ=90°) versus frequency and horizontal separation.

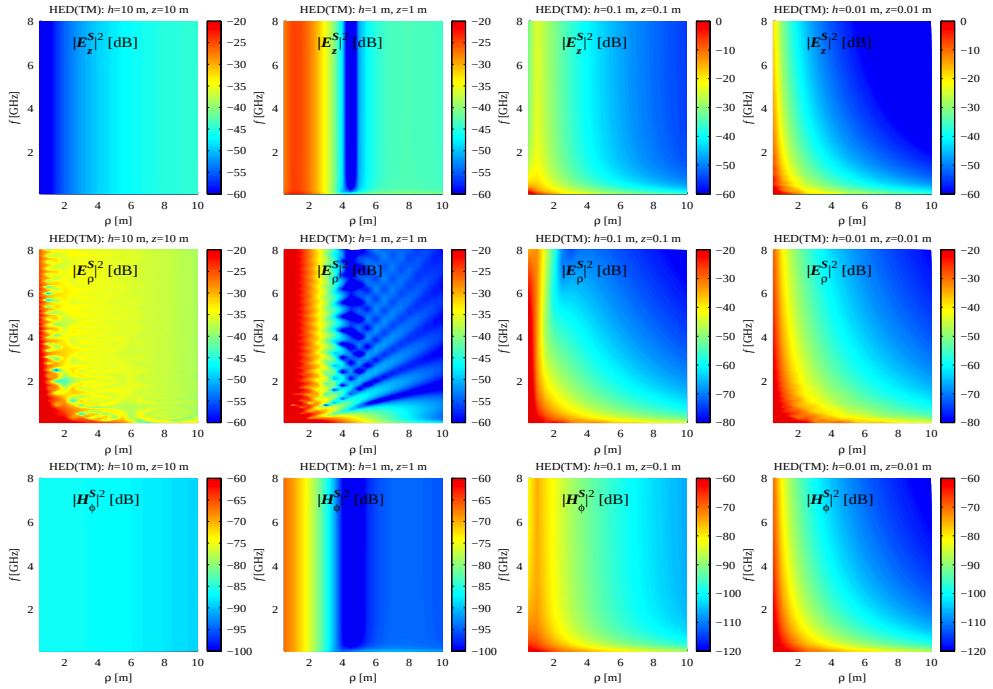

Figure A-9. Sommerfeld field strength of a HED above a concrete half space (h=z, φ=0°) versus frequency and horizontal separation.

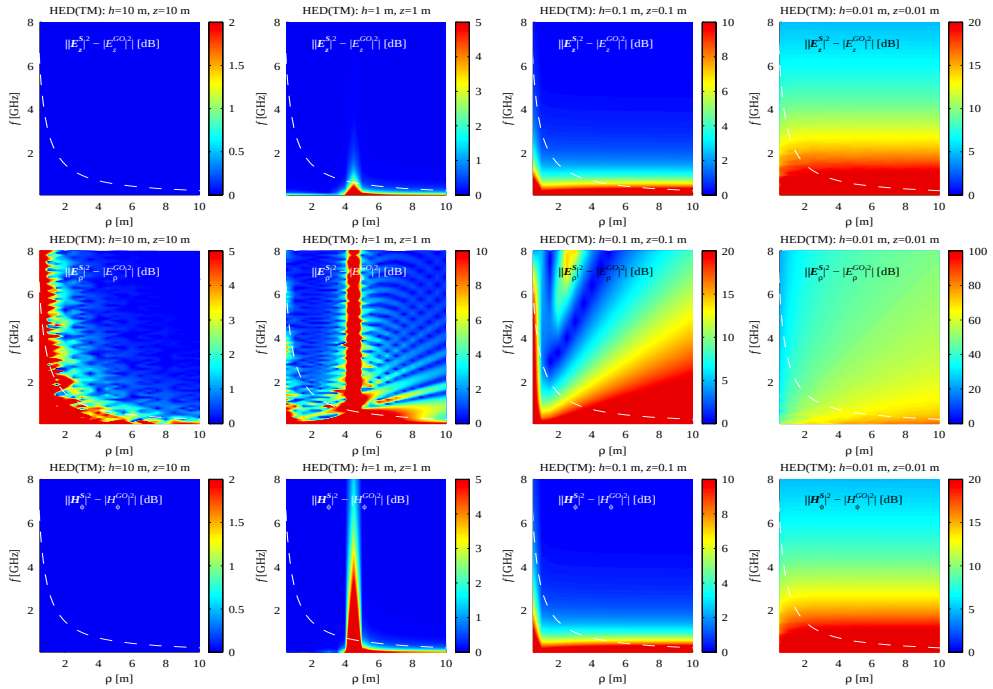

Figure A-10. Field strength residual error of a HED above a concrete half space (h=z, φ=0°) versus frequency and horizontal separation.

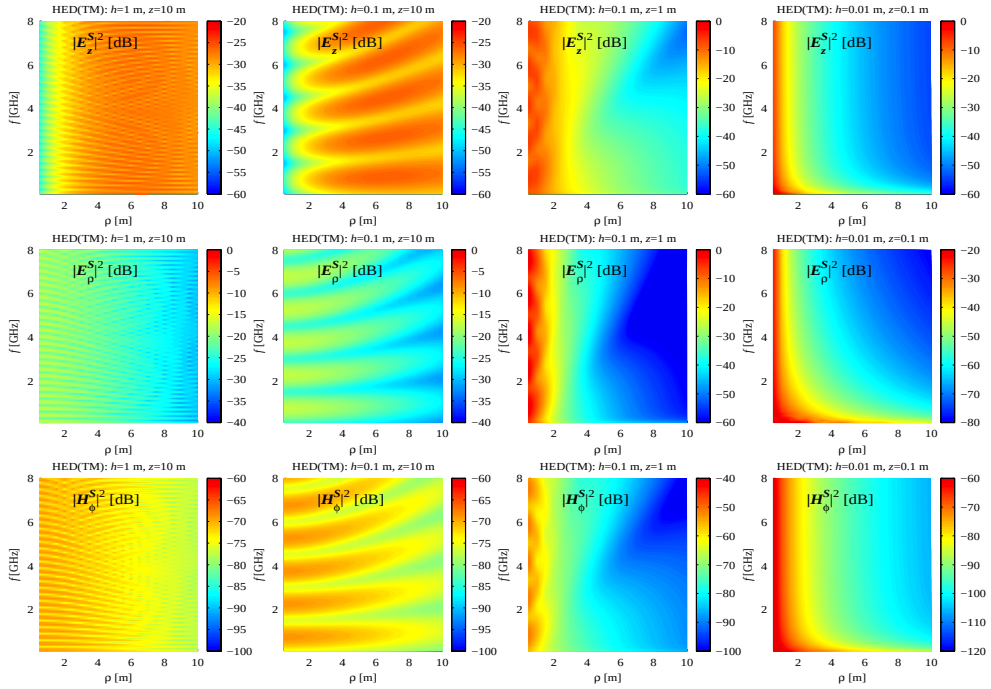

Figure A-11. Sommerfeld field strength of a HED above a concrete half space ($h \neq z$, $\varphi = 0°$) versus frequency and horizontal separation.

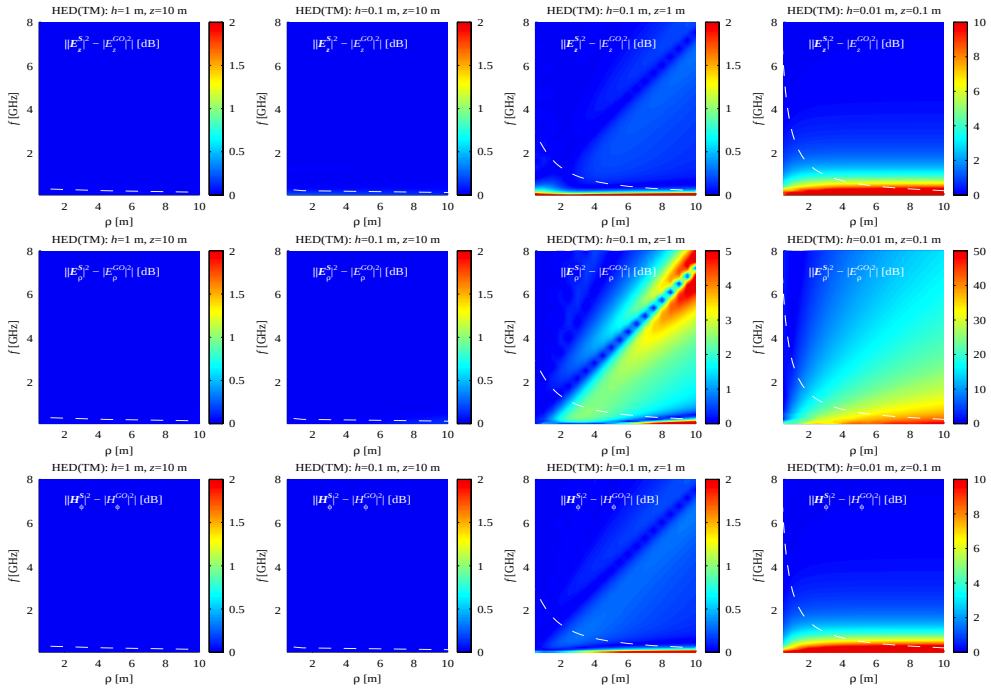

Figure A-12. Field strength residual error of a HED above a concrete half space ($h \neq z$, $\varphi = 0°$) versus frequency and horizontal separation.

APPENDIX B: IMPULSE RESPONSES FOR SIGNALS CENTERED AT 2.4 GHz

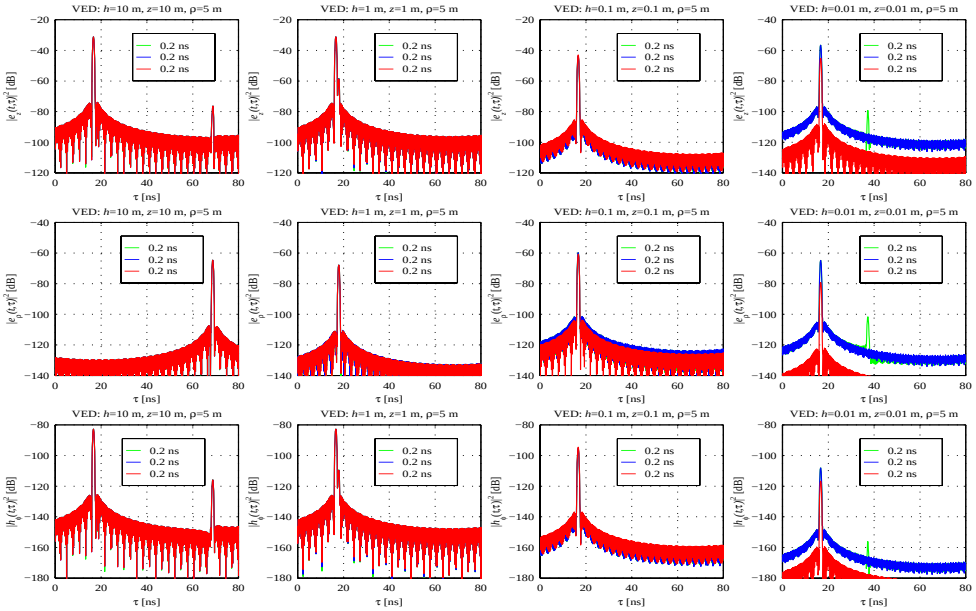

Figure B-1. Near-surface effects on impulse responses of a VED above a concrete half space (f_c=2.4 GHz, BW≈1 GHz, threshold=-30 dB). Legends display Sommerfeld, GO + Norton term, and GO approximations to delay spread.

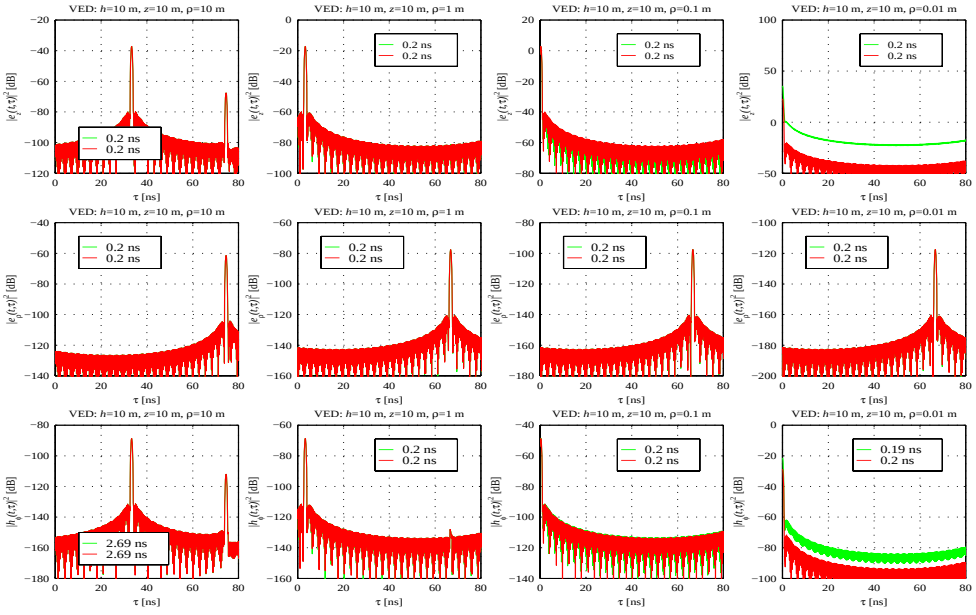

Figure B-2. Near-field effects on impulse responses of a VED above a concrete half space (f_c=2.4 GHz, BW≈1 GHz, threshold=-30 dB). Legends display Sommerfeld and GO approximations to delay spread.

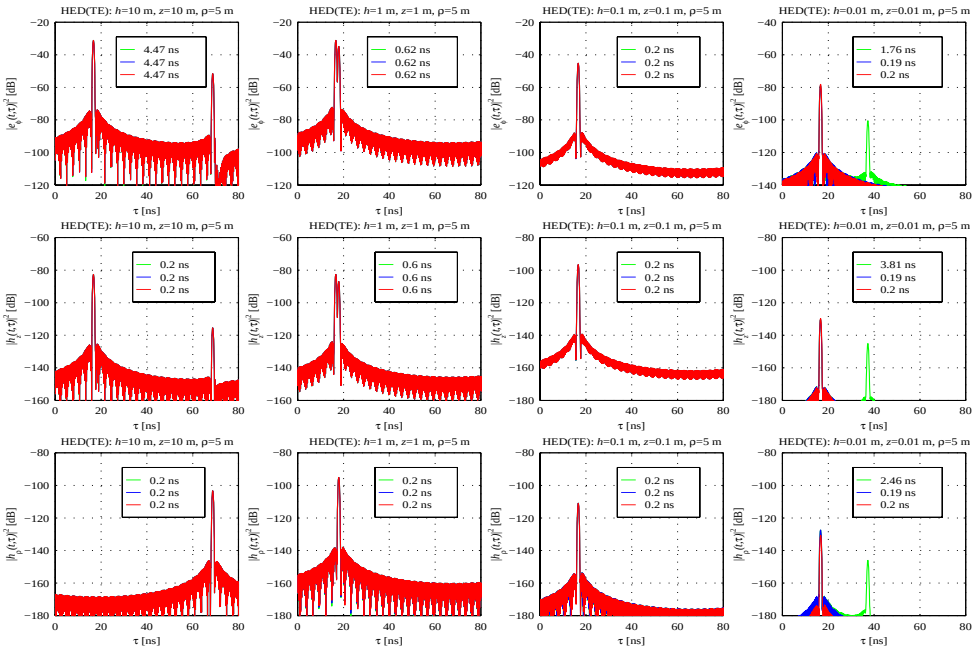

Figure B-3. Near-surface effects on impulse responses of an x-aligned HED above a concrete half space (f_c=2.4 GHz, BW≈1 GHz, threshold=-30 dB, φ=90 °). Legends display Sommerfeld, GO + Norton term, and GO approximations to delay spread.

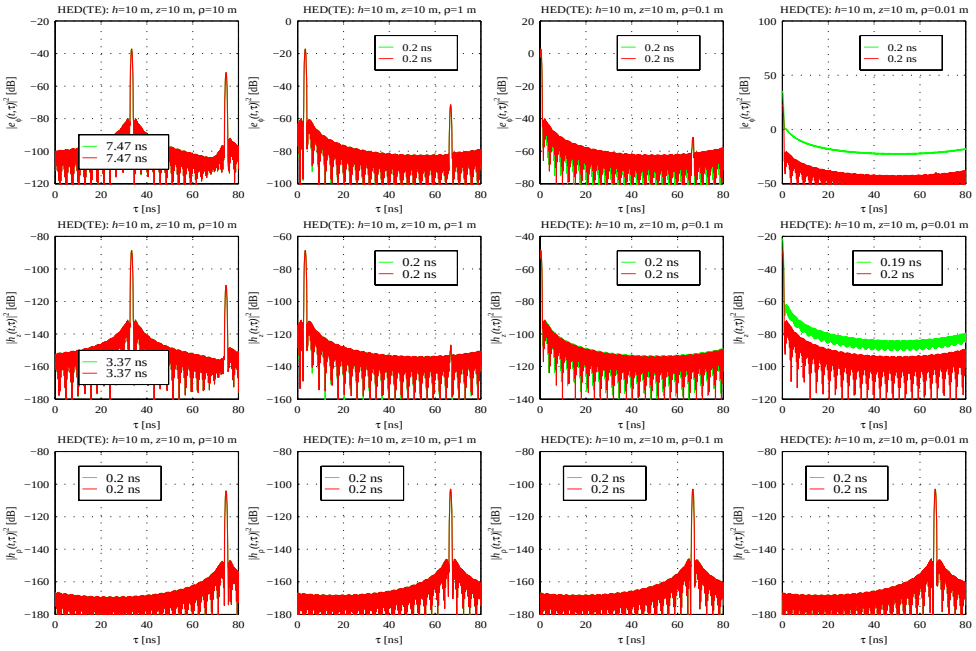

Figure B-4. Near-field effects on impulse responses of an x-directed HED above a concrete half space (f_c=2.4 GHz, BW≈1 GHz, threshold=-30 dB, φ=90 °). Legends display Sommerfeld and GO approximations to delay spread.

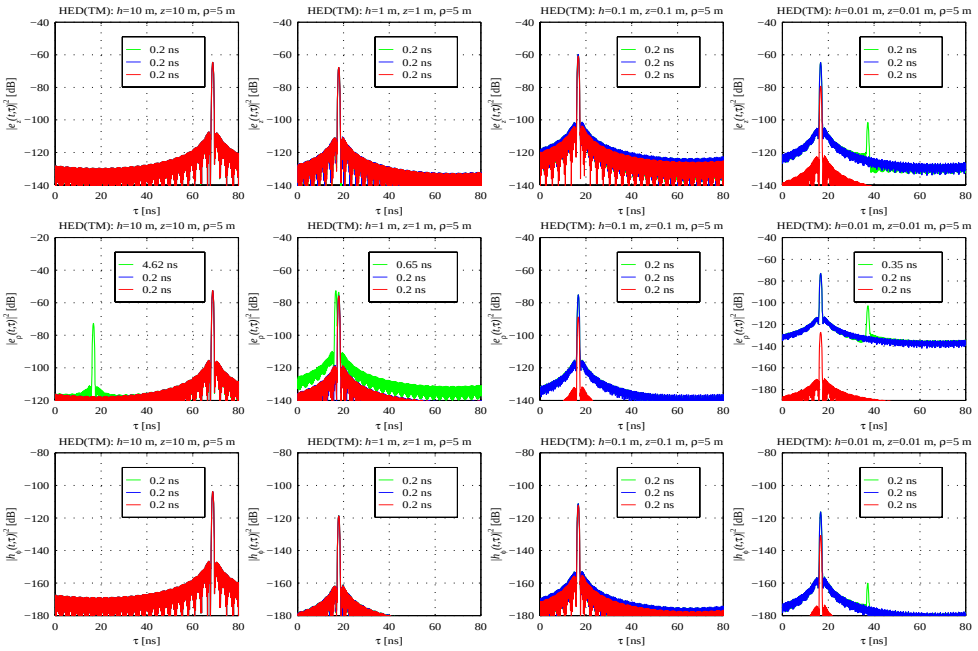

Figure B-5. Near-surface effects on impulse responses of an x-aligned HED above a concrete half space (f_c=2.4 GHz, BW≈1 GHz, threshold=-30 dB, φ=0°). Legends display Sommerfeld, GO + Norton term, and GO approximations to delay spread.

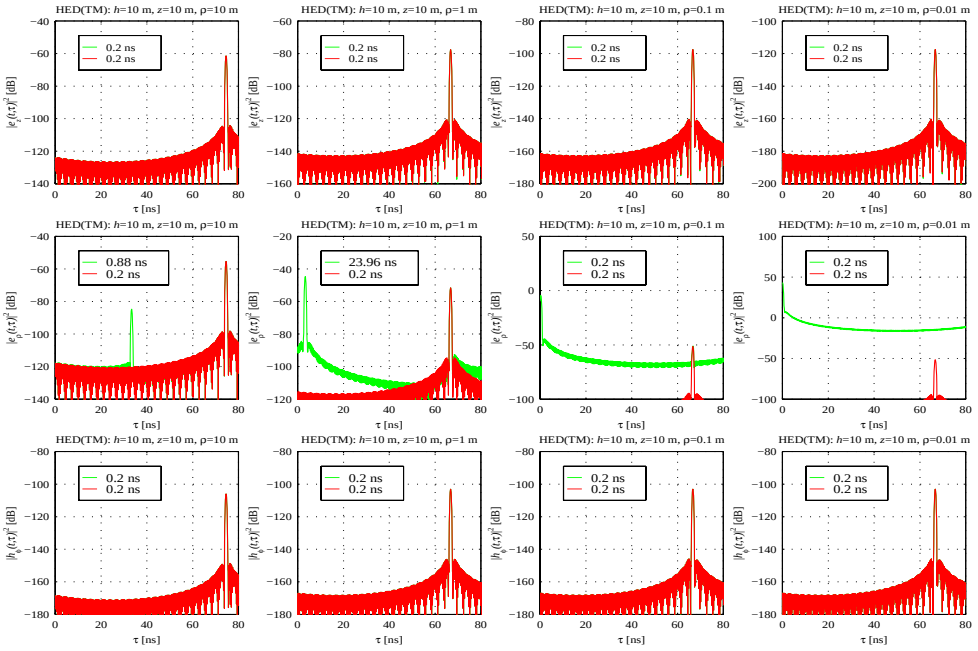

Figure B-6. Near-field effects on impulse responses of an x-aligned HED above a concrete half space (f_c=2.4 GHz, BW≈1 GHz, threshold=-30 dB, φ=0°). Legends display Sommerfeld and GO approximations to delay spread.

This Page Intentionally Left Blank

This Page Intentionally Left Blank

APPENDIX C: IMPULSE RESPONSES FOR SIGNALS CENTERED AT 5.8 GHz

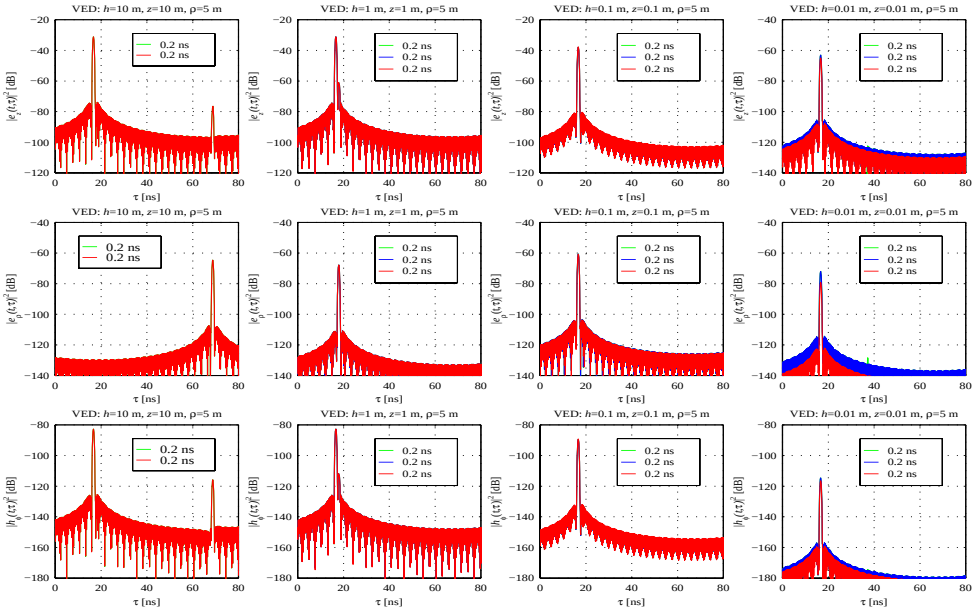

Figure C-1. Near-surface effects on impulse responses of a VED above a concrete half space (f_c=5.8 GHz, BW≈1 GHz, threshold=-30 dB). Legends display Sommerfeld, GO + Norton term, and GO approximations to delay spread.

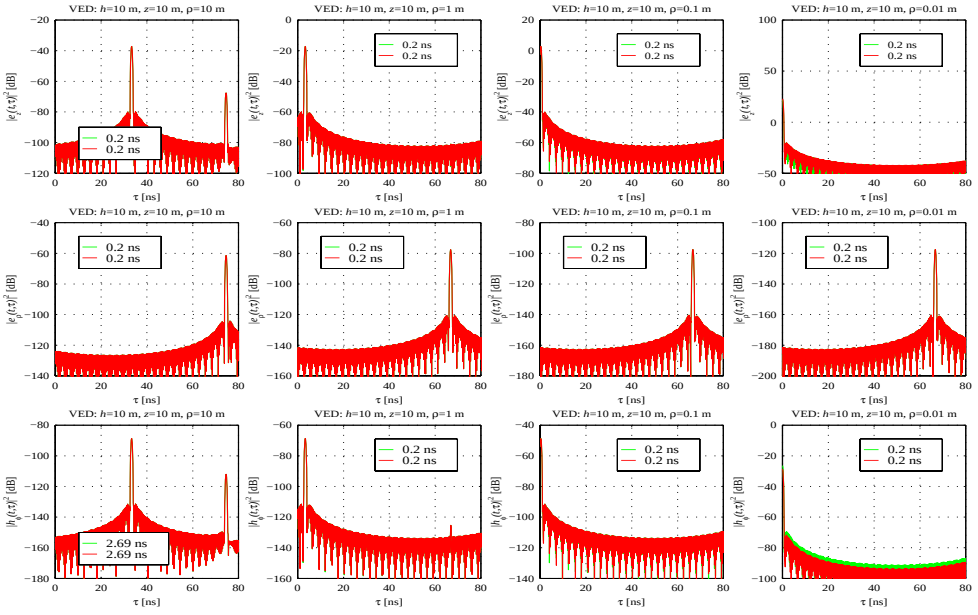

Figure C-2. Near-field effects on impulse responses of a VED above a concrete half space (f_c=5.8 GHz, BW≈1 GHz, threshold=-30 dB). Legends display Sommerfeld and GO approximations to delay spread.

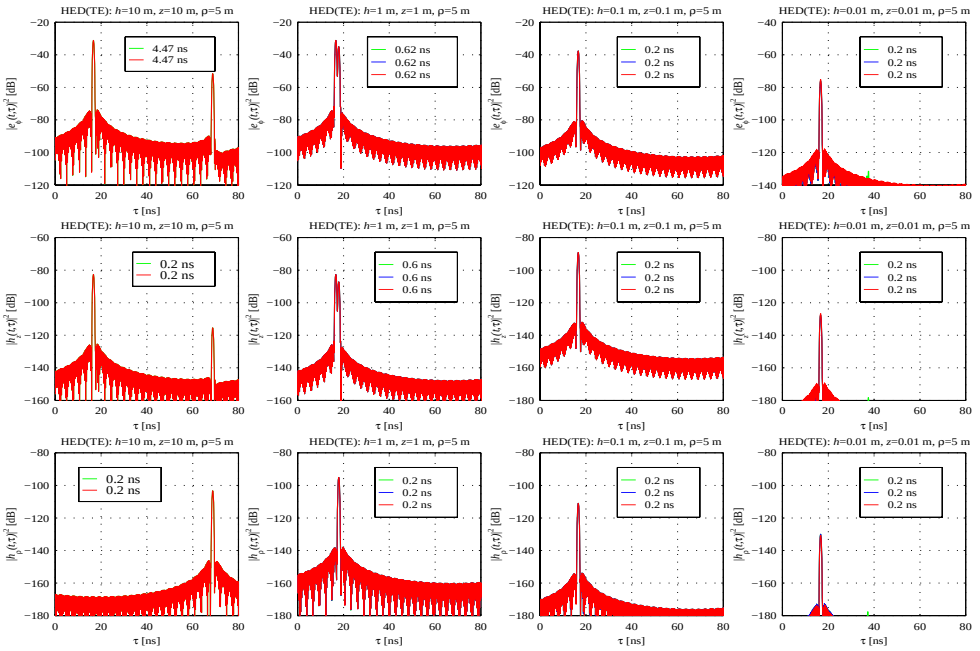

Figure C-3. Near-surface effects on impulse responses of an x-aligned HED above a concrete half space (f_c=5.8 GHz, BW≈1 GHz, threshold=-30 dB, φ=90 °). Legends display Sommerfeld, GO + Norton term, and GO approximations to delay spread.

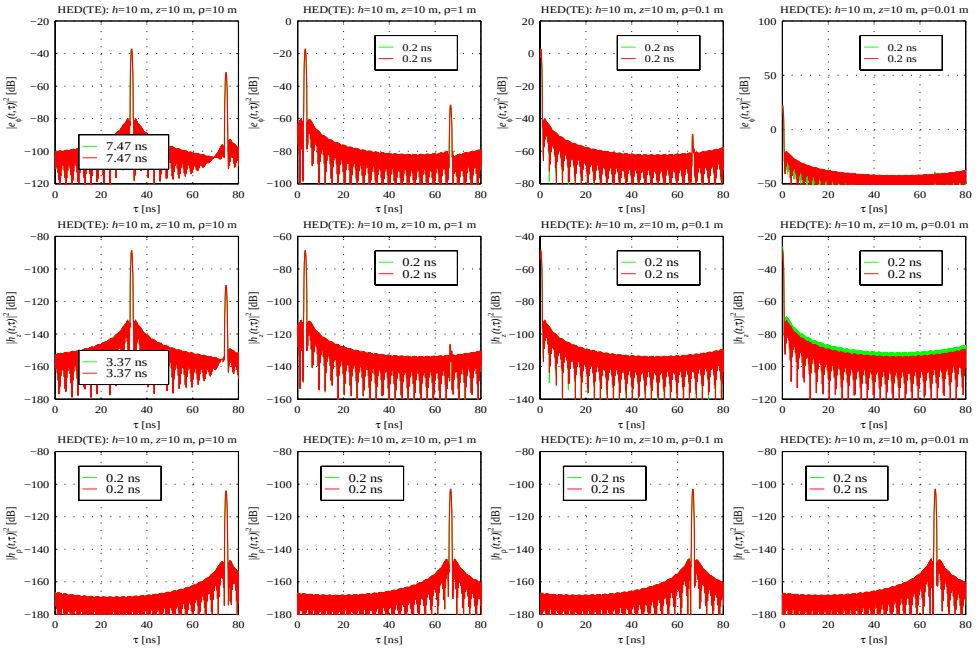

Figure C-4. Near-field effects on impulse responses of an x-directed HED above a concrete half space (f_c=5.8 GHz, BW≈1 GHz, threshold=-30 dB, φ=90 °). Legends display Sommerfeld and GO approximations to delay spread.

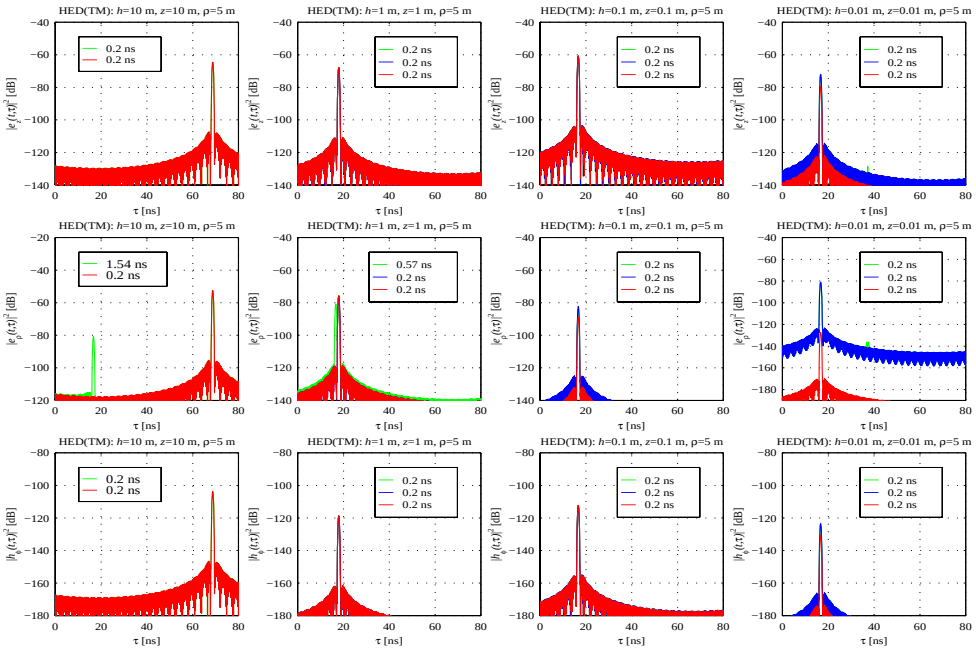

Figure C-5. Near-surface effects on impulse responses of an x-aligned HED above a concrete half space (f_c=5.8 GHz, BW≈1 GHz, threshold=-30 dB, φ=0°). Legends display Sommerfeld, GO + Norton term, and GO approximations to delay spread.

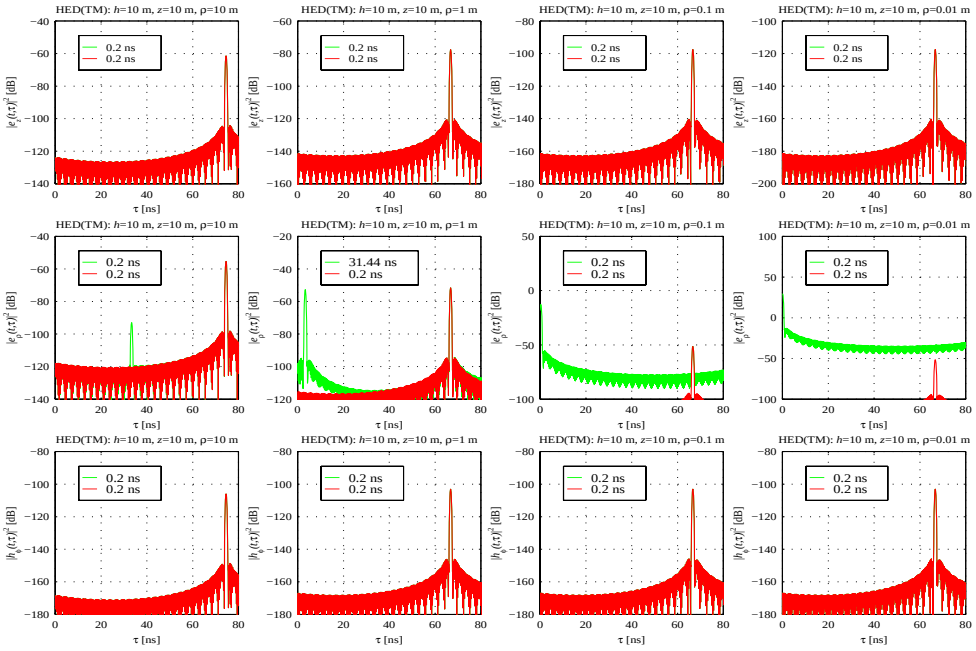

Figure C-6. Near-field effects on impulse responses of an x-aligned HED above a concrete half space (f_c=5.8 GHz, BW≈1 GHz, threshold=-30 dB, φ=0°). Legends display Sommerfeld and GO approximations to delay spread.

This Page Intentionally Left Blank

This Page Intentionally Left Blank

APPENDIX D: DELAY SPREAD VERSUS BANDWIDTH

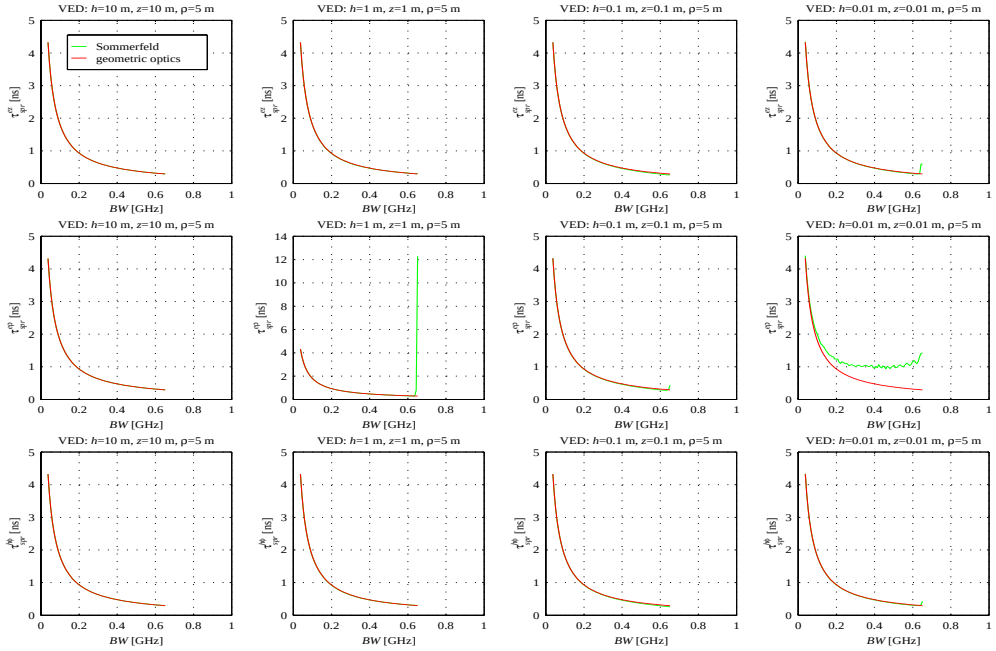

Figure D-1. Near-surface effects on delay spread versus bandwidth for a VED above a concrete half space at f_c=900 MHz (Hamming window, threshold=-30 dB).

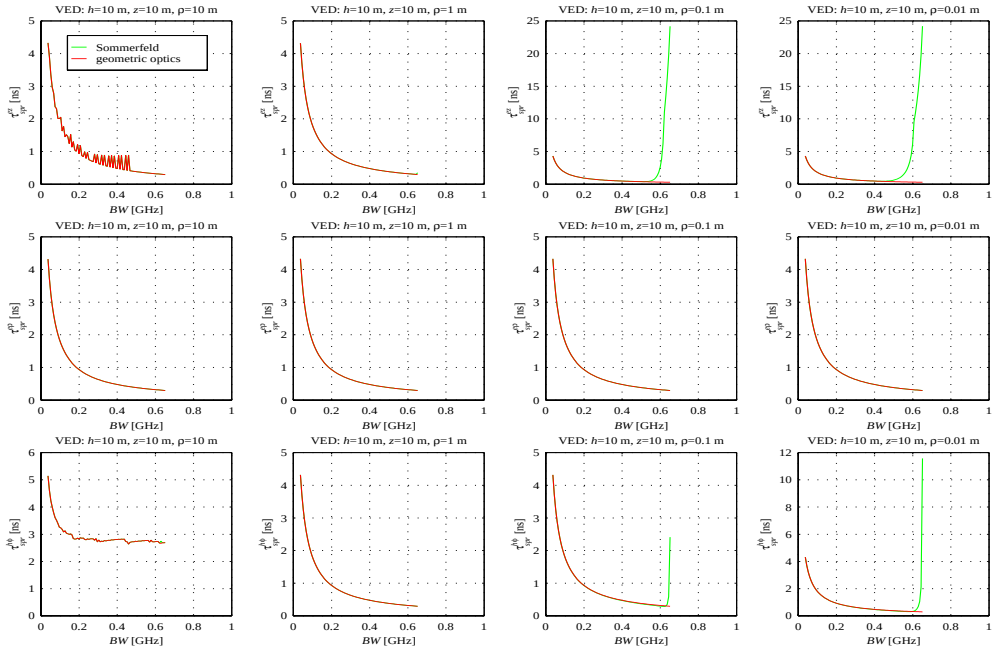

Figure D-2. Near-field effects on delay spread versus bandwidth for a VED above a concrete half space at f_c=900 MHz (Hamming window, threshold=-30 dB).

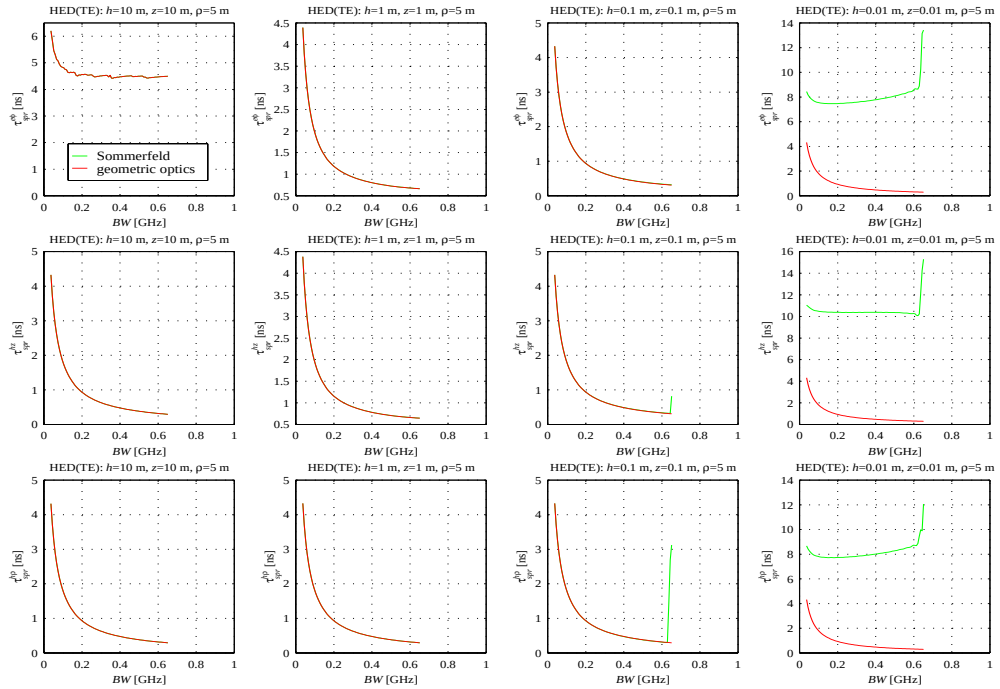

Figure D-3. Near-surface effects on delay spread versus bandwidth for a HED above a concrete half space at f_c=900 MHz (Hamming window, threshold=-30 dB, φ=90°).

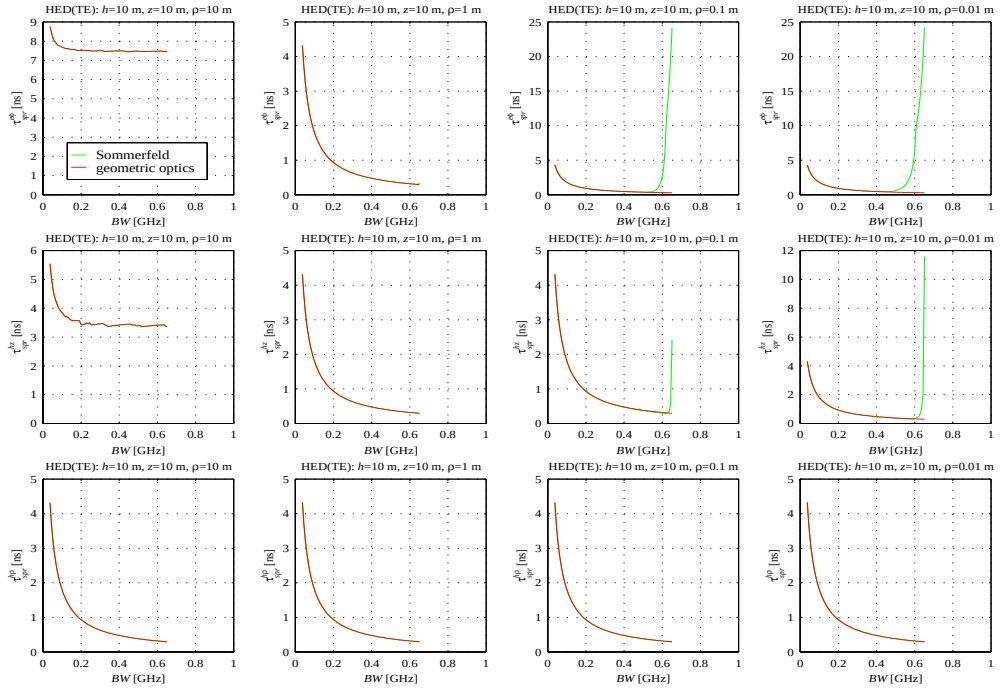

Figure D-4. Near-field effects on delay spread versus bandwidth for a HED above a concrete half space at f_c=900 MHz (Hamming window, threshold=-30 dB, φ=90°).

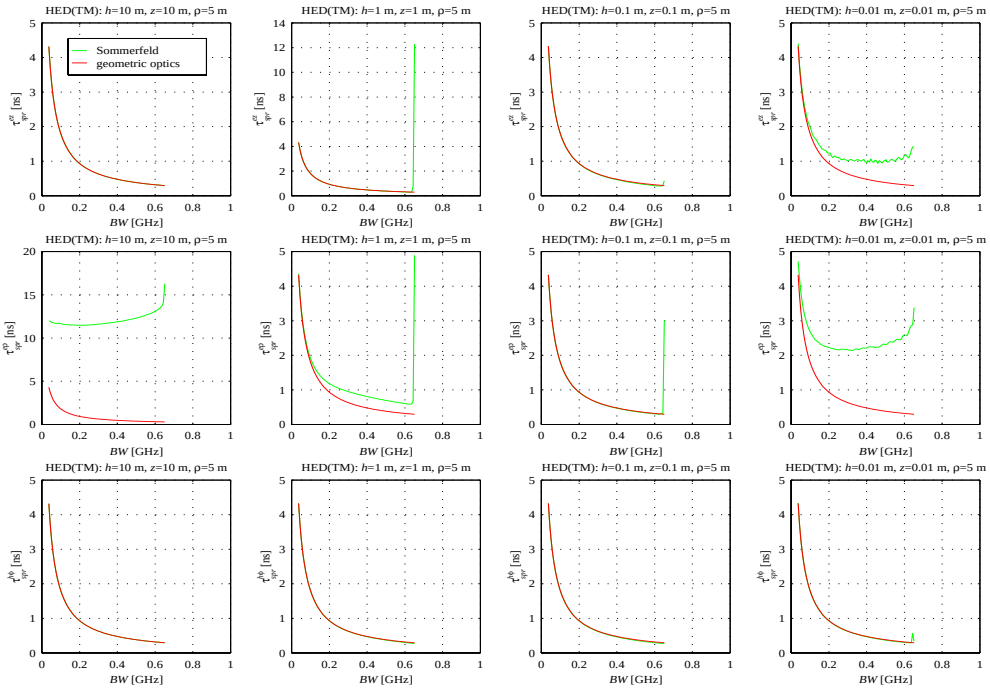

Figure D-5. Near-surface effects on delay spread versus bandwidth for a HED above a concrete half space at f_c=900 MHz (Hamming window, threshold=-30 dB, φ=0°).

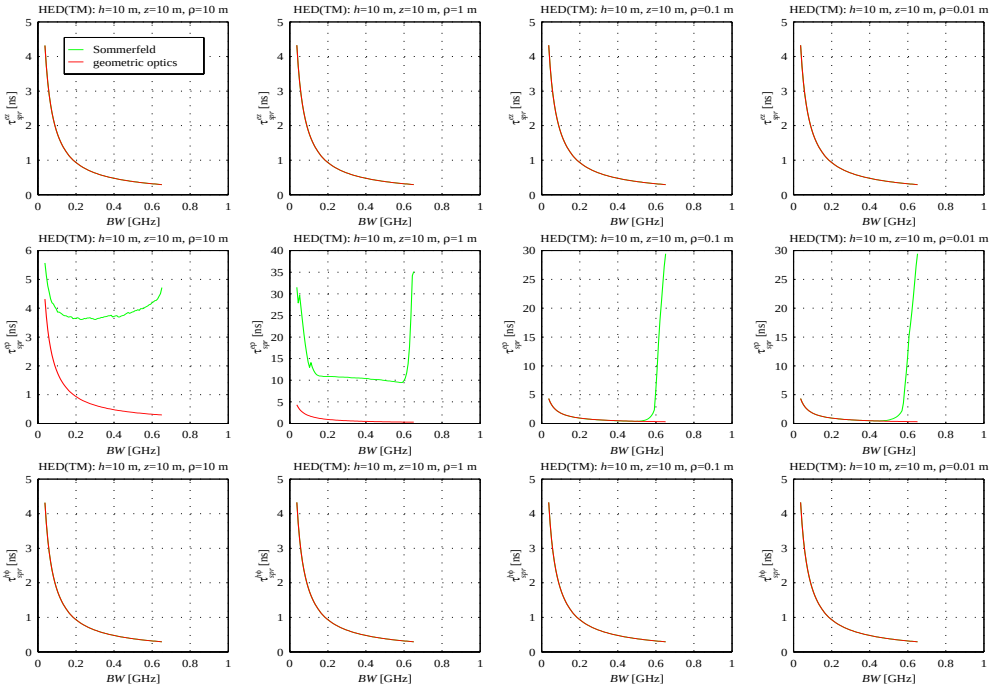

Figure D-6. Near-field effects on delay spread versus bandwidth for a HED above a concrete half space at f_c=900 MHz (Hamming window, threshold=-30 dB, φ=0°).

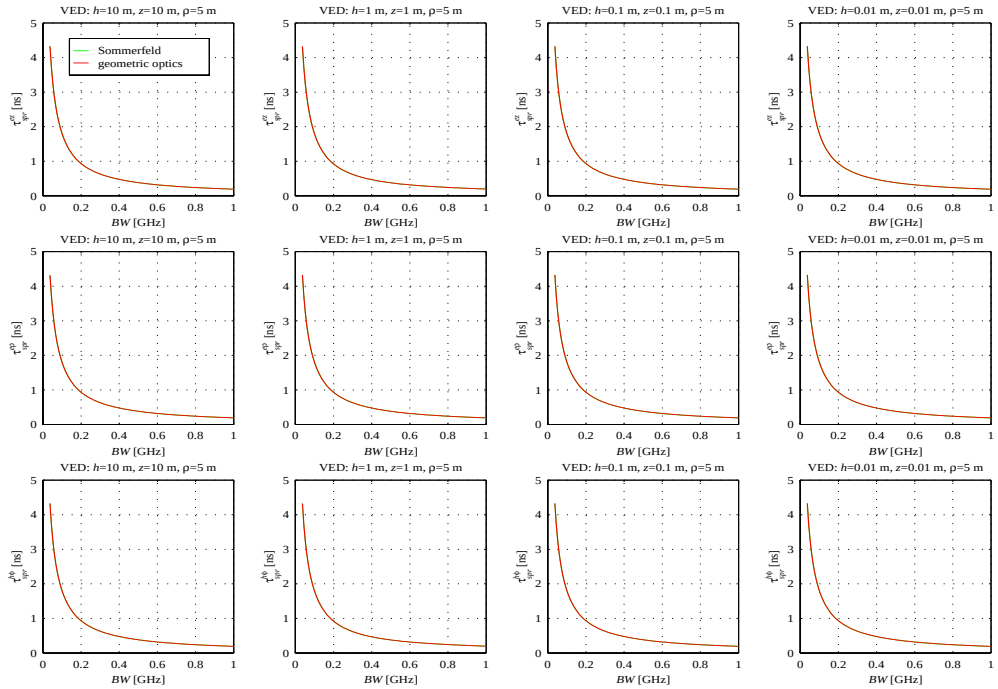

Figure D-7. Near-surface effects on delay spread versus bandwidth for a VED above a concrete half space at f_c=2.4 GHz (Hamming window, threshold=-30 dB).

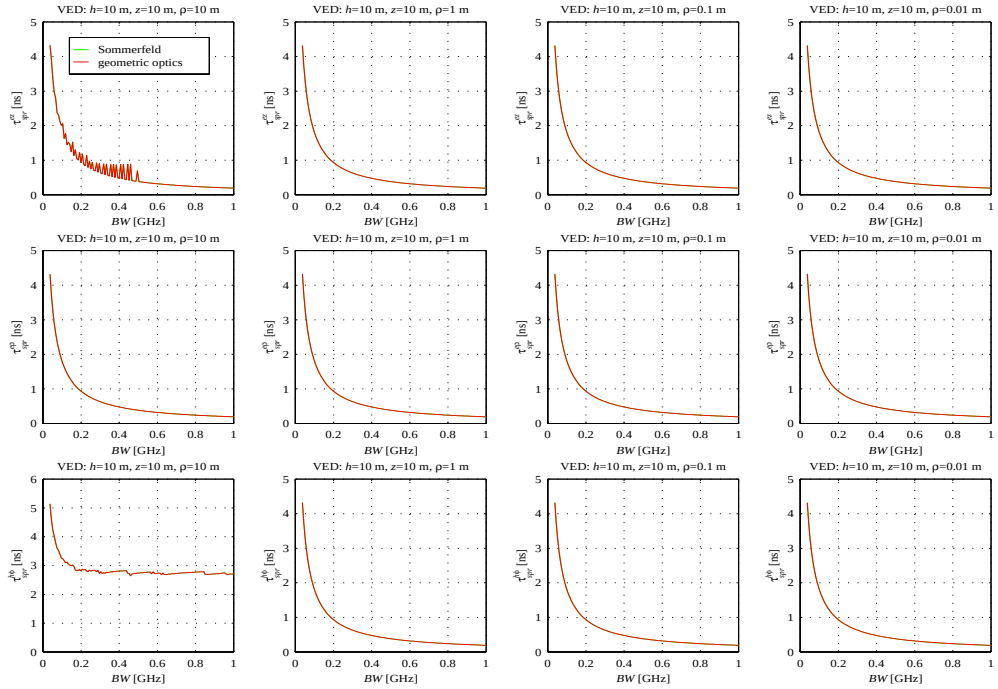

Figure D-8. Near-field effects on delay spread versus bandwidth for a VED above a concrete half space at f_c=2.4 GHz (Hamming window, threshold=-30 dB).

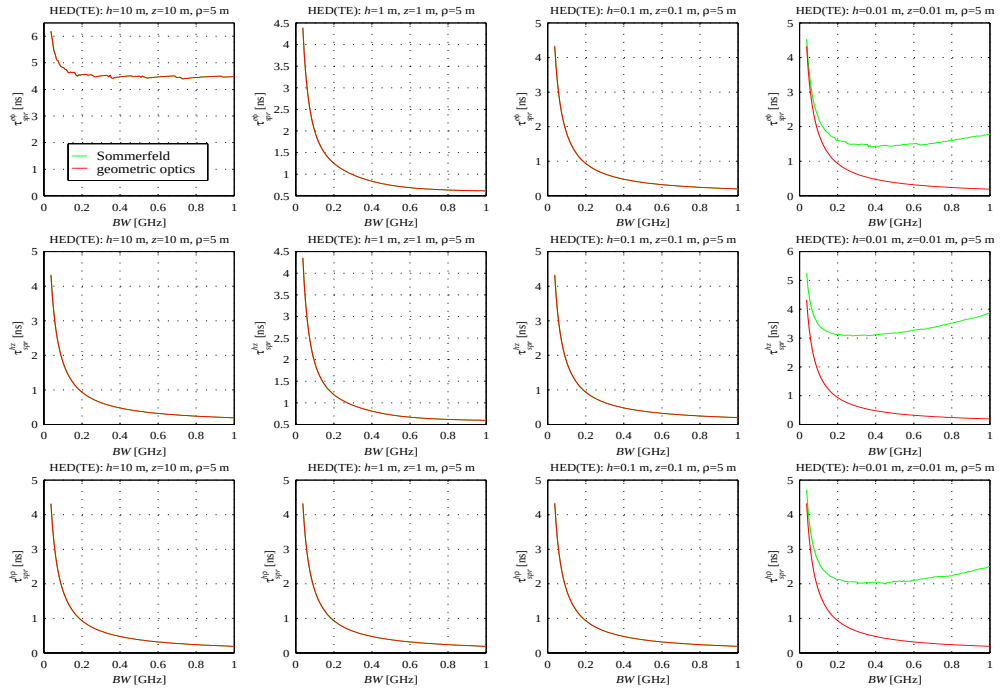

Figure D-9. Near-surface effects on delay spread versus bandwidth for a HED above a concrete half space at f_c=2.4 GHz (Hamming window, threshold=-30 dB, φ=90 °).

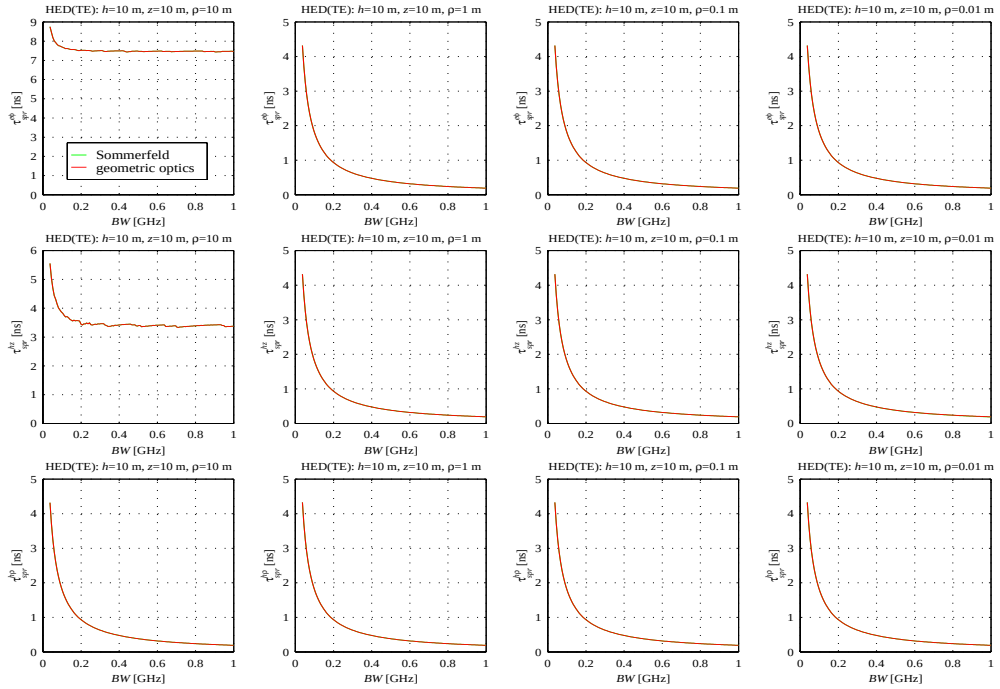

Figure D-10. Near-field effects on delay spread versus bandwidth for a HED above a concrete half space at f_c=2.4 GHz (Hamming window, threshold=-30 dB, φ=90 °).

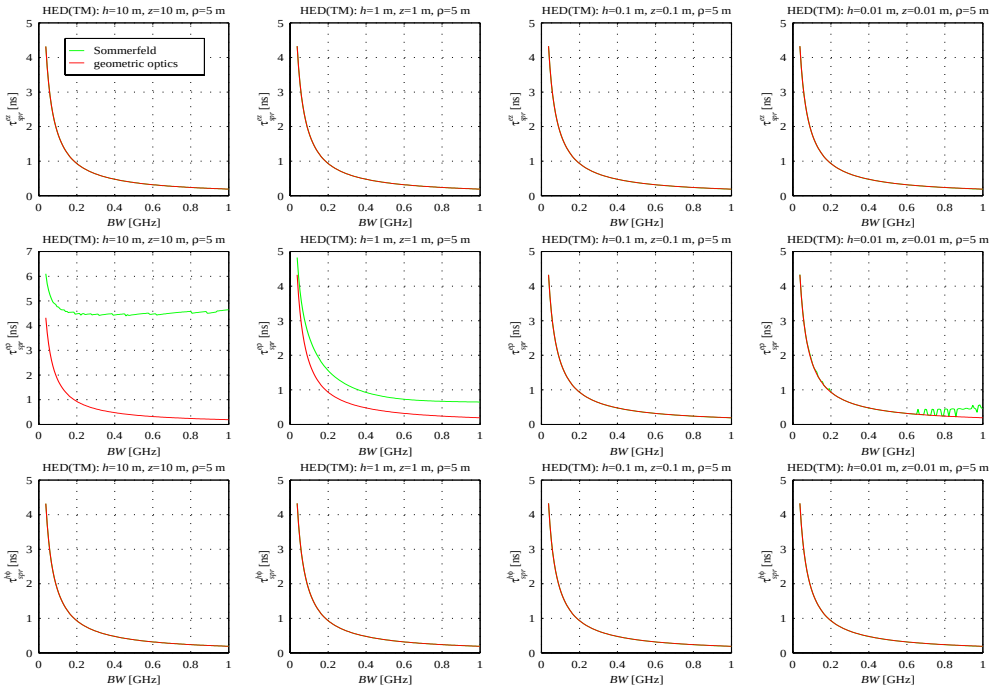

Figure D-11. Near-surface effects on delay spread versus bandwidth for a HED above a concrete half space at f_c=2.4 GHz (Hamming window, threshold=-30 dB, φ=0°).

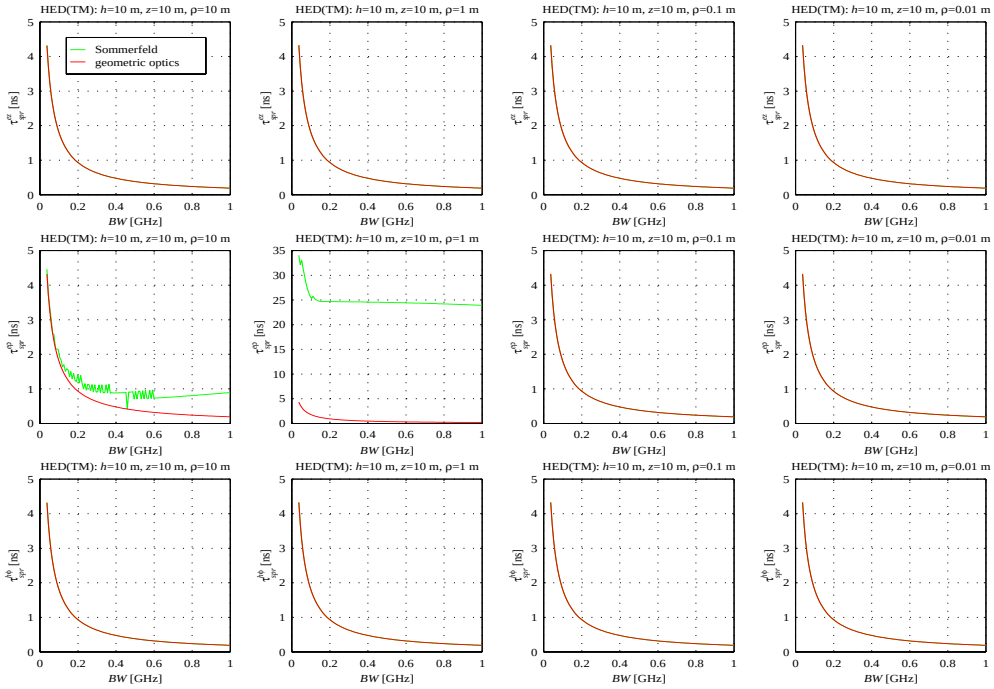

Figure D-12. Near-field effects on delay spread versus bandwidth for a HED above a concrete half space at f_c=2.4 GHz (Hamming window, threshold=-30 dB, φ=0°).

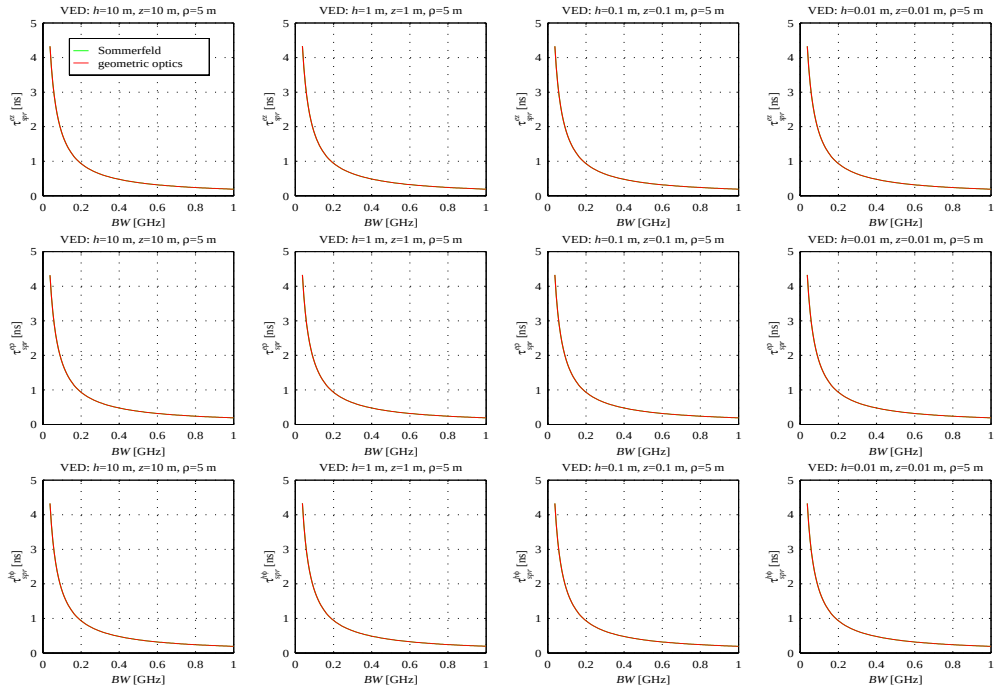

Figure D-13. Near-surface effects on delay spread versus bandwidth for a VED above a concrete half space at f_c=5.8 GHz (Hamming window, threshold=-30 dB).

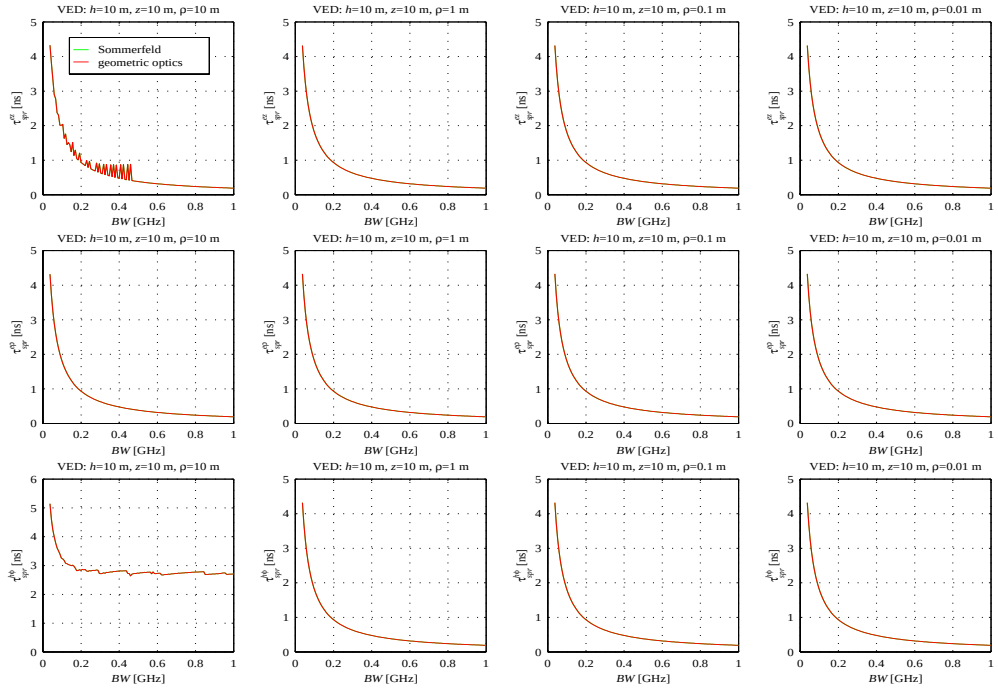

Figure D-14. Near-field effects on delay spread versus bandwidth for a VED above a concrete half space at f_c=5.8 GHz (Hamming window, threshold=-30 dB).

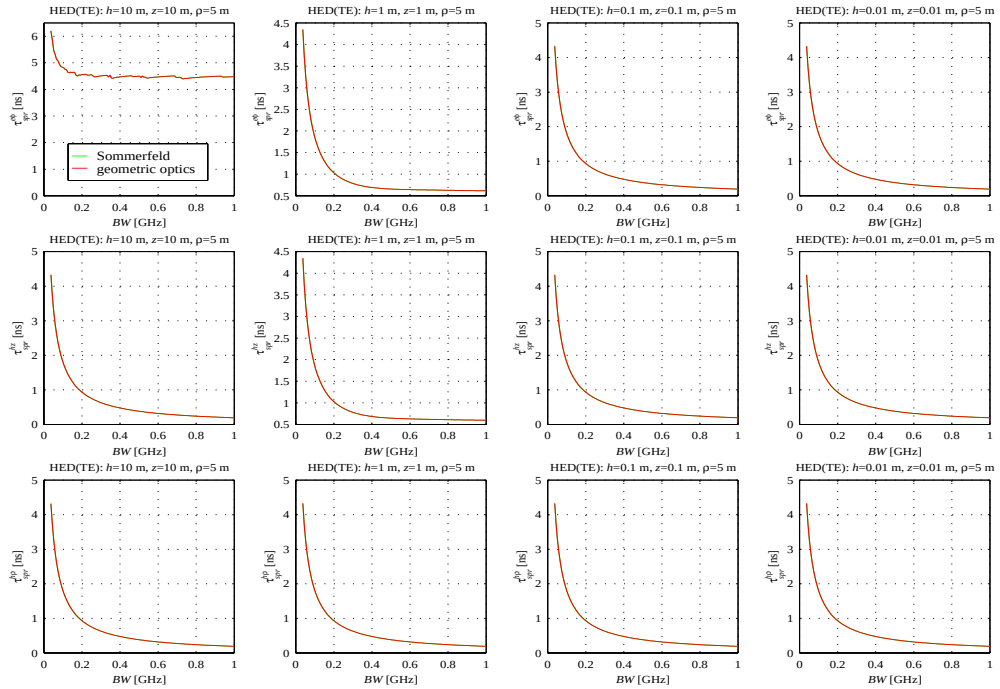

Figure D-15. Near-surface effects on delay spread versus bandwidth for a HED above a concrete half space at f_c=5.8 GHz (Hamming window, threshold=-30 dB, φ=90°).

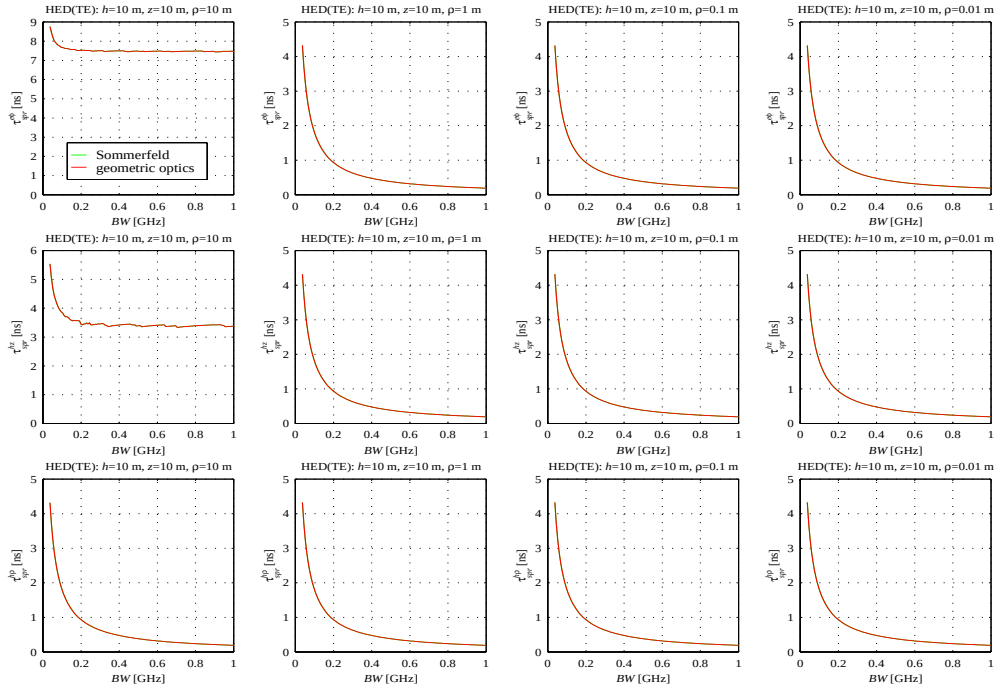

Figure D-16. Near-field effects on delay spread versus bandwidth for a HED above a concrete half space at f_c=5.8 GHz (Hamming window, threshold=-30 dB, φ=90°).

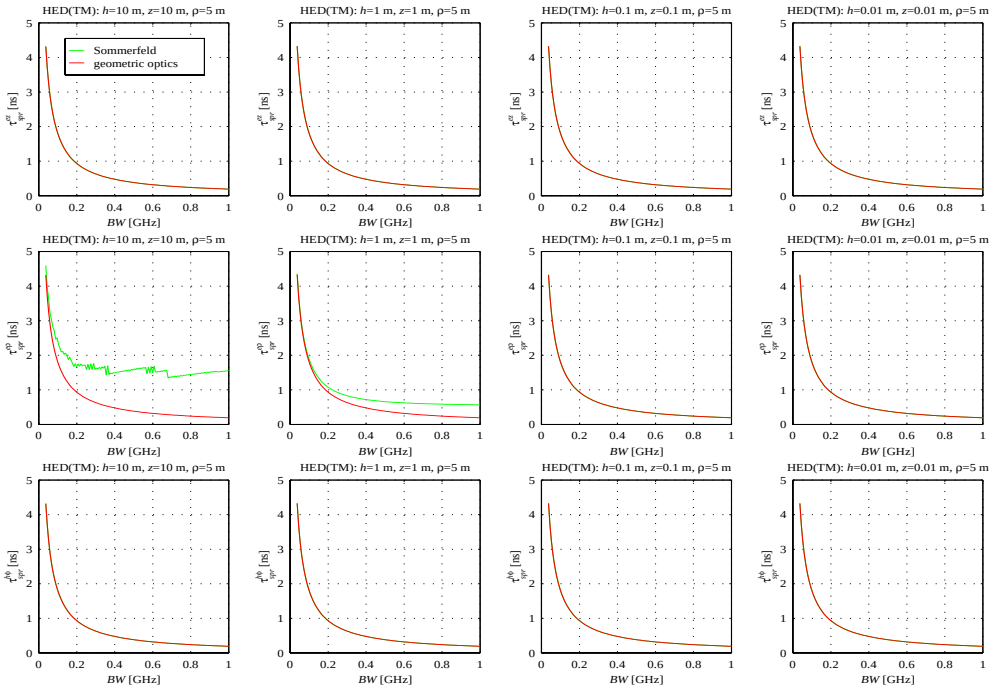

Figure D-17. Near-surface effects on delay spread versus bandwidth for a HED above a concrete half space at f_c=5.8 GHz (Hamming window, threshold=-30 dB, φ=0°).

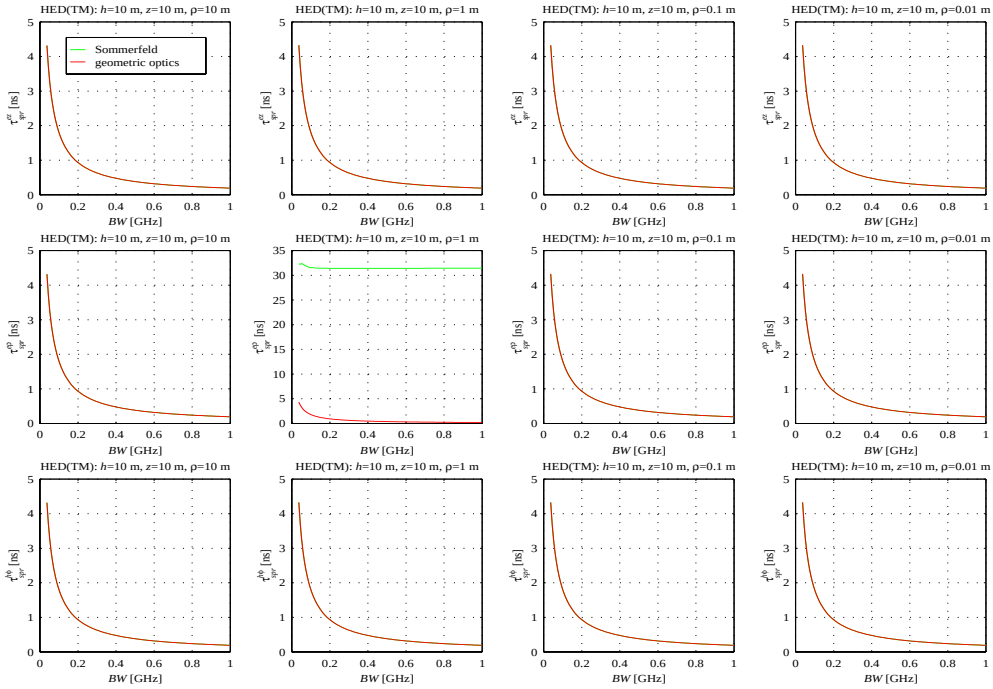

Figure D-18. Near-field effects on delay spread versus bandwidth for a HED above a concrete half space at f_c=5.8 GHz (Hamming window, threshold=-30 dB, φ=0°).